INVESTIGATION OF HIGH TEMPERATURE TENSILE CREEP OF REFRACTORIES

Dissertation at the Chair of Ceramics of the University of Leoben (Montanuniversität) to reach the degree of

"**Doktor der montanistischen Wissenschaften**"

Submitted by

Amina SIDI MAMMAR

Leoben, February 2016

AFFIDAVIT

I declare in lieu of oath, that I wrote this thesis and performed the associated research myself, using only literature cited in this volume.

To my beloved father,

Acknowledgments

Financial support by the Austrian Federal Government (in particular from Bundesministerium für Verkehr, Innovation und Technologie and Bundesministerium für Wissenschaft, Forschung und Wirtschaft) represented by Österreichische Forschungsförderungsgesellschaft mbH and the Styrian and the Tyrolean Provincial Government, represented by Steirische Wirtschafts-förderungsgesellschaft mbH and Standortagentur Tirol, within the framework of the COMET Funding Programme is gratefully acknowledged.

Foremost, I would like to express my sincere gratitude to my supervisor Prof. Harald Harmuth (Chair of Ceramics, Leoben) for his availability and continuous guidance. Thank you for the immense knowledge you brought me, for always believing in me and for your moral support when I needed it the most. I could not have imagined having a better mentor during my doctoral studies.

I would like to thank Prof. Huger (GEMH, Limoges) for his insightful comments, advice and expertise in scientific issues. Thank you for your flexibility and availability.

I am also grateful to Dr. Dietmar Gruber (Chair of Ceramics, Leoben) for his patience, support and assistance. Many thanks for your very interesting advices and help with my academic research during these four years. You have always brought me rigorous answers to my questionings which allowed me to progress more quickly than expected.

My sincere thanks also go to Dr. Jin (Chair of Ceramics, Leoben) for his availability, support and care. Thank you for the numerous discussions on the related topics that helped me expand my knowledge in the area. I also am thankful to you for commenting on my views and helping me understand and enrich my ideas.

I am also indebted to my colleagues from the Chair of ceramics with whom I have interacted during the course of my graduate studies. Particularly, I would like to acknowledge Ms. Christina Atzenhofer, Dr. Magdalena Drózd-Ryś, Dr. Christoph Fasching, Mr. Robert Caks, Dr. Sabine Gschiel, Ms. Marianne Doletschek… and many others for the valuable discussions that allowed me to enjoy my stay in Leoben and helped to improve better my research area and my German skills.

Many friends have helped me stay focused and motivated through these years of research. Their support and care helped me overcome challenging moments and stay determined on my graduate studies. I greatly value their friendship and I deeply appreciate their belief in me.

Most importantly, none of this would have been possible without the patience and love of my family. My family has been a constant source of concern, love, support and strength all these

years. I would like to express my heart-felt gratitude to my father Mokrane, my mother Lila and my brothers Omar, Tarik and Tahar for their infinite love and for supporting me throughout my life.

Abstract

A new tensile creep testing facility for high temperature measurements of heterogeneous refractories was introduced in order to characterize materials applied for the lining of furnaces and vessels of the steel industry. The machine allowed accurate specimen alignment and holding systems. A uniform loading permitted to avoid bending and uneven stress distribution in the specimen. Prior to the measurements, thermo-mechanical simulations were carried out in order to optimize the testing procedure. Feasibility of the experiments was confirmed with the selection of an optimal heating rate. Observation of temperature and stress distributions in the hot zone and the cold ends confirmed the specimen shape and dimensions chosen.

Creep behaviour of magnesia-chromite and magnesia-spinel bricks were measured as a function of tensile stress in the range from 0.2 to 1.9 MPa and as a function of temperature in the range from 1100 °C to 1600 °C. Three creep phases were revealed at these conditions indicating the strain-hardening, the steady state and the strain-softening behaviour of the materials. The procedure developed for the interpretation of the experimental results included the selection of Norton-Bailey creep law, the identification of the creep stages and the calculation of the creep parameters by inverse-estimation using the general reduced gradient (GRG) or Levenberg-Marquardt (L-M) algorithms. A detailed study of creep behaviour of magnesia-chromite material was then carried on with bringing to light the evident correlation existing between the creep strain, the applied stress and the temperature. An approach which consisted on finding the transition points between the creep stages in dependence of stress and temperature can be implemented in a simulation program. The activation energy was evaluated for this material; however it was not evident to conclude about the different mechanisms happening during creep due to their probable simultaneous occurrence in the heterogeneous material.

Norton-Bailey creep parameters describing the strain-hardening behaviour of magnesia-chromite were then implemented in the software Abaqus for a thermomechanical modelling of an RH-snorkel. Three models were investigated and compared; the symmetrical tensile, the symmetrical compressive and the asymmetrical creep models. During process the refractory lining endures high thermal stresses. The temperature and stress distributions were evaluated and compared at different moments of the first heat. The asymmetrical creep model was more representative than the symmetrical ones.

Table of contents

Introduction

Refractory materials are applied in diverse fields, among them the industries of steel, cement, nonferrous metals, glass and several others. They became indispensable for industrial processes at extremely high temperatures beyond 1000 °C. Refractory materials bring a level of high performance to industrial vessels because of their improved resistance against not only high temperature, but also against corrosion, external mechanical loads and thermal shock. However under operating conditions their performance over time may be altered due to continual thermal cycling and important tensile and compressive loadings, leading to their creep. The expected creep deformation affects the lining design and durability.

Despite the influence of the tensile creep on refractories in service, there has been no subsequent advancement on that area. Many researches were capable to relate the creep of refractories under compressive loads, but only few of them showed concern on their tensile creep behaviour. This is due to the difficulties of testing heterogeneous refractory materials under the conditions of tensile creep loading. Many aspects have to be taken into consideration. Long term experiments capable of measuring small strains at temperatures up to 1600 °C should be performed. This induces providing a suitable alignment to avoid bending of the specimen and guarantee uniform uniaxial stresses during loading. Moreover, suitable fixtures at high temperatures for relatively brittle refractories could be difficult to implement. Presently only two standards for testing creep related properties of refractory materials at high temperature exist: Creep In Compression (CIC) and Refractoriness Under Load (RUL). However the applied compressive loads are restricted to 0.2 MPa. During operation the loads influencing the creep additionally occur under tension and exceed 0.2 MPa. Creep data under tensile loading also need to be provided in order to design failure resistant systems.

Experimental and numerical approaches are combined in this study for the characterization of creep under tensile loads at high temperature and for further simulating industrial refractory linings during service conditions.

In the first chapter the state of the art concerning tensile creep of refractory materials is compiled. The detailed bibliographical review relates the various tensile creep testing procedures and mechanisms, the existing creep laws as well as their applications to the asymmetric creep response.

The second chapter highlights the innovative design of the testing setup and the measurement procedure. The modelling conducted prior to measurements points out the chosen specimen and heating rate, and confirms the feasibility of the creep testing at extremely high temperatures.

Chapter 3 sums up the tensile creep measurements for two refractory materials at high temperatures and different applied loads. The creep of a magnesia-chromite and a magnesia-spinel refractory is represented as a material property in a simulation program. The processing of the creep data requests the use of powerful tools and accurate evaluation methods.

After having studied the creep of two refractories and implemented a valuable evaluation method for creep parameters identification, tensile creep data are applied to linings of an industrial vessel. In the last chapter the results of asymmetric creep model are presented for a case study.

Chapter 1: State of the art

1.1 Introduction

Industrial construction parts, viz. refractories, employed in steel production at high temperature are constrained with respect to their thermal expansion. This leads to a growth of tensile and compressive stresses during heating and cooling cycles. Depending on the refractories mechanical properties, their response is different. On the one hand creep may contribute to a stress decrease and avoid e.g. spalling of brittle materials. On the other hand creep close to the hot face after e.g. contact with liquid steel reduces the brick dimension. This may bring about a higher risk of tensile failure after further thermal equilibration. Therefore, quantitative material models for refractory creep are mandatory to assess the material behaviour. Several testing methods, including creep, investigate refractory material properties and describe their behaviour indicating threshold stresses for safety at high temperatures. This first chapter resumes the existing advanced technology for performance of such experiments and more specifically those related to creep; which is mainly performed under compressive loading for ordinary refractories or under tensile loading for advanced ceramics. Creep laws are numerous and should be well known, their use helps for understanding the comportment of refractory materials. Creep law parameters may be suitable to clarify the mechanisms occurring during creep. Creep laws are further integrated into simulations of industrial vessels in order to comprehend their performance in service and optimize their creep resistance under tough conditions. Creep of a ceramic material is above all asymmetrical, meaning that it is more severe in tension than in compression under the same loading level due to the dilatation of the material. Further studies managed to apply asymmetric creep models to ceramics taking into account both compressive and tensile creep influence.

1.2 Definition of creep

Creep is a type of deformation that occurs in dependence of time and under constant load, the amount of deformation is a function of stress, temperature, time and structure of the material [1]. After the elastic behaviour of the material, three stages as a consequence of irreversible deformation may follow. In the primary creep, also called transient creep, the material hardens while a decreasing strain rate is observed ($\partial\varepsilon_{cr}/\partial t \neq$ constant and $\partial^2\varepsilon_{cr}/\partial t^2 < 0$). It is followed by the secondary stage which is characterized by constant creep rate ($\partial\varepsilon_{cr}/\partial t =$ constant) not anymore time dependent. The tertiary regime shows a region of rapid increase of the creep rate ($\partial\varepsilon_{cr}/\partial t > 0$), the material experiences strain softening behaviour in anticipation of ultimate fracture. **Fig. 1** illustrates the typical creep behaviour with respect to time.

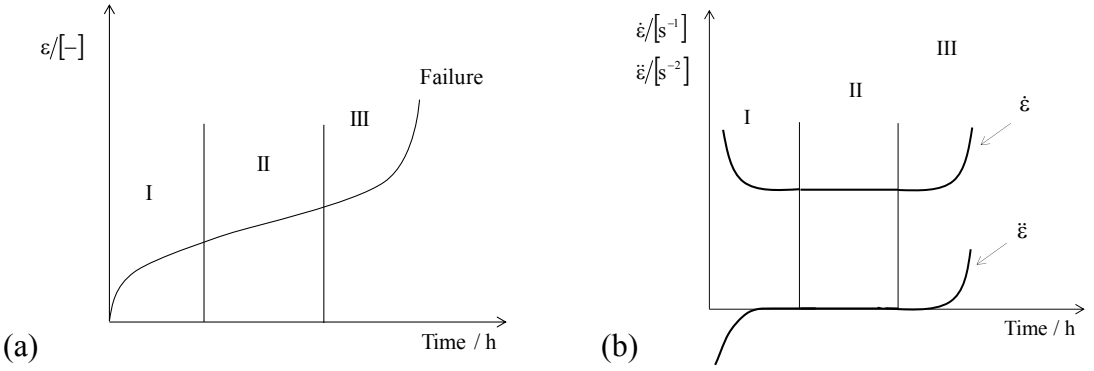

Figure 1: (a) Theoretical creep strain, (b) creep rate and acceleration with respect to time.

1.3 Creep laws

Creep laws describing the strain with respect to time were proposed for all types of materials including refractories. Factors like material composition, magnitude of the applied load or temperature have a direct effect on creep. The overall basic creep equation is written with respect to the applied stress σ, the time *t* and the temperature *T* as follows:

$$\varepsilon_{cr} = f(\sigma, t, T) \tag{1}$$

Several creep laws assume that the impact of the parameters can be separated [2, 3]:

$$\varepsilon_{cr} = f_1(\sigma) f_2(t) f_3(T) \tag{2}$$

In the past decades numerous hypotheses were proposed for the development of creep laws. Stress, time and temperature functions of creep according to literature references are described in a large number of alternative expressions [3, 4 and 5]. Although many stress dependent creep models were proposed [6, 7, 8], the power function of the applied stress ascribed to Norton [9] is nowadays one of the most commonly used law.

$$f_1(\sigma) = b_1 \sigma^n \tag{3}$$

Time dependence of creep was considered by Bailey [10] among many other existing creep functions [7, 11, 12 and 13], see **Eq. 4**. Many of them certainly describe the time function effectively. While the representation of creep performance may be comparable, they disagree in the number of involved constants.

$$f_2(t) = b_2 t^m \tag{4}$$

Here b_1 and b_2 are material constants. The commonly used temperature dependent creep function was defined by Arrhenius [5, 14, 15 and 16] and is given as

$$f_3(T) = A\exp\left(\frac{-Q}{RT}\right) \tag{5}$$

A is the pre-exponential factor, Q is the activation energy, R is the general gas constant and T is the absolute temperature. The above creep function, **Eq. 2**, could be then represented as

$$\varepsilon_{cr} = b_1\sigma^n b_2 t^m A\exp\left(\frac{Q}{RT}\right) \tag{6}$$

If creep occurs under isothermal conditions, for a given temperature the function then may be simplified to:

$$\varepsilon_{cr} = B\sigma^n t^m \tag{7}$$

The latter equation, recognized as Norton-Bailey creep law, was often exploited for creep analysis and was applied under constant uniaxial stress [17, 18]. Creep under variable uniaxial stress - although being not completely satisfactory - was based on the theories derived from creep under constant stress. Two hypotheses were put forward [2]: time hardening; assuming that the creep strain rate is a function of stress, time and temperature (see **Eq. 8**), or strain hardening; where the creep strain rate is rather a function of stress, temperature and accumulated creep strain (see **Eq. 9**).

$$\frac{d\varepsilon_{cr}}{dt} = f(\sigma,t,T) = f_1(\sigma)\frac{df_2(t)}{dt}f_3(T) \tag{8}$$

$$\frac{d\varepsilon_{cr}}{dt} = f(\sigma,\varepsilon_{cr},T) = g_1(\sigma)g_2(\varepsilon_{cr})g_3(T) \tag{9}$$

The derivative of **Eq. 7** with respect to time gives

$$\frac{d\varepsilon_{cr}}{dt} = B\sigma^n m t^{m-1} \tag{10}$$

By substituting the time variable from **Eq. 7**, the creep strain rate can be written as

$$\frac{d\varepsilon_{cr}}{dt} = mB^{\frac{1}{m}}\sigma^{\frac{n}{m}}\varepsilon_{cr}^{\frac{m-1}{m}} \tag{11}$$

Both of the **Eq. 10** and **Eq. 11** are strain rate functions that describe the time hardening and the strain hardening behaviour of the material, respectively [19]. They were used primarily to model the primary creep stage by determining the creep coefficients m, n and B. Several theories and laws emerged from these two hypotheses to describe the creep behaviour of ceramics. The general equation employed in many researches [20, 21 and 22] that expresses secondary creep of single phase ceramics by taking into consideration grain size exponent is written as follows

$$\dot{\varepsilon}_{cr} = C\frac{\sigma^{n}}{d^{p}}\exp\left(-\frac{Q}{RT}\right) \tag{12}$$

C is a constant, d is the grain size, p is the grain size exponent, σ is the applied stress and n is the stress exponent.

Lin *et al* [23] adopted the model of Raj and Ashby [24] that was derived from the general creep equation to analyse the creep deformation of alumina-silicon carbide composites

$$\dot{\varepsilon}_{cr} = C\frac{\sigma^{n}}{d^{p}r^{q}V}\exp\left(-\frac{Q}{RT}\right) \tag{13}$$

V is the whisker content, r is the whisker radius and q is the radius exponent. Creep performance can be improved by varying whisker content and size as well as the matrix grain size. To describe a multiphase refractory system, MgO-$CaMgSiO_4$, Snowden and Pask [25] employed the creep rate equation that considers shear modulus G.

$$\dot{\varepsilon}_{cr} = A\left(\frac{\sigma}{G}\right)^{n}\exp\left(\frac{-Q}{RT}\right) \tag{14}$$

Here n is a dimensionless constant and the factor A having a dimension of [1/time] varies linearly with G and inversely with the temperature. With assuming that two mechanisms operate simultaneously and by introducing a structural parameter S, the steady-state creep rate was then expressed [25].

$$\dot{\varepsilon}_{cr} = \sum_{i=1} A_i f_i(\sigma, T, S)\exp\left(\frac{-Q_i}{RT}\right) \tag{15}$$

Here f_i represents the functional dependence for the i^{th} mechanism on the applied stress, temperature and structure parameter S. Q_i is the apparent activation energy for creep by each mechanism. It was determined at several temperatures using the incremental temperature technique described by Dorn [5].

Luecke and Wiederhorn [26, 27] suggested that creep of Si_3N_4 is mainly controlled by cavity formation and growth during the steady state and proposed a model of the creep strain rate in relation with the volume fraction of the amorphous phase Φ and a constant α.

$$\dot{\varepsilon}_{cr} = A\sigma\exp\left(\frac{-\Delta H}{RT}\right)\frac{\Phi^{3}}{(1-\Phi)^{2}}\exp(\alpha\sigma) \tag{16}$$

Multi-axial creep was considered [28, 29] in order to establish constitutive creep models [30, 31]. Experiments showed for isotropic and homogeneous materials that creep can be dominated by shear stresses with the material volume maintained constant during creep; the rate of volume creep is then nil [32, 33 and 34]:

$$\dot{\varepsilon}_1 + \dot{\varepsilon}_2 + \dot{\varepsilon}_3 = 0 \tag{17}$$

Here $\dot{\varepsilon}_1, \dot{\varepsilon}_2$ and $\dot{\varepsilon}_3$ are principal strain rates.

$$\frac{\dot{\gamma}_1}{\tau_1} = \frac{\dot{\gamma}_2}{\tau_2} = \frac{\dot{\gamma}_3}{\tau_3} = 2\psi \tag{18}$$

Here ψ is a constant; $\dot{\gamma}_1, \dot{\gamma}_2$ and $\dot{\gamma}_3$ are principal shear strain rates; τ_1, τ_2 and τ_3 are principal shear stresses. The principal shear strain rates are related to the principal shear stresses.

$$\tau_1 = \frac{\sigma_2 - \sigma_3}{2},\ \tau_2 = \frac{\sigma_3 - \sigma_1}{2} \text{ and } \tau_3 = \frac{\sigma_1 - \sigma_2}{2}$$

$$\dot{\gamma}_1 = \dot{\varepsilon}_2 - \dot{\varepsilon}_3,\ \dot{\gamma}_2 = \dot{\varepsilon}_3 - \dot{\varepsilon}_1 \text{ and } \dot{\gamma}_3 = \dot{\varepsilon}_1 - \dot{\varepsilon}_2$$

The assumption made is that the effective strain rate, $\dot{\varepsilon}_e$, is associated to the effective stress similarly to the uniaxial case:

$$\dot{\varepsilon}_e = f_1(\bar{\sigma}) f_2(t) \tag{19}$$

$$\bar{\sigma} = \frac{\sqrt{2}}{2}\sqrt{(\sigma_1 - \sigma_2)^2 + (\sigma_2 - \sigma_3)^2 + (\sigma_1 - \sigma_3)^2} \tag{20}$$

Here $\bar{\sigma}$ is Von Mises equivalent stress.

1.4 Creep mechanisms in ceramics and some representative creep functions

The mechanisms of creep are identified by the calculation of the stress, strain and grain size exponents in addition to the apparent activation energy, all derived from the steady-state creep regime. Theoretical creep mechanisms at high temperature describing intergranular or intragranular deformation progressions are described by the strain rate, $\dot{\varepsilon}$, which is in dependence on several parameters [35].

$$\dot{\varepsilon} = \frac{ADGb}{kT}\left(\frac{b}{d}\right)^p \left(\frac{\sigma}{G}\right)^n \tag{21}$$

A is a dimensionless constant, *D* is the diffusion coefficient of the governing diffusion process, *G* is the shear modulus, *b* is the Burger's vector, *k* is Boltzmann's constant, *T* is the absolute temperature, *d* is the grain size, *p* is the exponent of the inverse grain size and *n* is the stress exponent. The diffusion coefficient is dependent on the activation energy, *Q*, necessary for the

diffusion process, the frequency factor D_0, the gas constant R (8.31 J mol^{-1} K^{-1}) and the temperature T.

$$D = D_0 \exp\left(\frac{-Q}{RT}\right) \tag{22}$$

Creep data are not easily interpretable especially for refractory ceramics, as they are in the most cases polycomponent materials with a porous grain/matrix structure and may develop liquid phases at service conditions.

The dominant creep mechanism, viz. the rate controlling one, may be intragranular, meaning that there is no dependency on the incidence of grain boundaries. The exponent of the inverse grain size p is nil and the deformation processes are then lattice mechanisms [36]. Numbers of lattice mechanisms were developed according to the predicted values of the strain exponent n and the activation energy Q; for example different types of dislocations glide and climb [37]. When the rate controlling creep is intergranular, here grain boundaries are involved in the deformation process [37], the exponent p is then defined as greater than or equal to 1. The grains displaced are influencing each other with a move happening either at the grain boundary plane or not far from it. This arrangement may take place together with tensile elongation of the grains [38]. More than a few boundary mechanisms were established, for instance sliding limited by diffusion creep (Nabarro-Herring or Coble), sliding controlled by intragranular flow across the grains, or sliding with or without continuous glassy phase at the boundary. In the absence of the glassy phase sliding is accommodated by formation of grain boundary cavities or formation of triple-points folds [35].

In the case of bonding phase displacement, creep rate is dependent on the tensile or the compressive deformation. A creep model assuming bonding of the grains via a Newtonian fluid (viscous grain boundary phase) was described by Dryden *et al* [39, 40]. Chadwick *et al* [41, 42] applied afterwards the theory of non-Newtonian viscous fluids based on the viscous flow models.

$$\dot{\varepsilon}_{cr} = \alpha_3 \sigma \frac{\left(\frac{\omega}{d}\right)^3}{\eta} = \alpha_3 \sigma \frac{(1-\Phi)^3}{\eta} \tag{23}$$

Here d is the grain size, ω is the bonding phase thickness, η is the effective viscosity of the bonding phase and Φ is its volume fraction. The matrix flow model exhibits a creep rate proportional to the volume fraction of the matrix cubed.

For solution-precipitation mechanism [43, 44 and 45] are involved parameters like grain size, diffusivity of ions from refractory grains through intergranular phase, $\dot{\varepsilon}_0$, apparent activation enthalpy of precipitation from liquid, $\Delta H_{sol\text{-}ppt}$, and other empirical constants σ_0, G_0 and [46].

$$\dot{\varepsilon}_{sol-ppt} = \dot{\varepsilon}_0 \left(\frac{G_0}{G} \right)^3 \left(\frac{\sigma}{\sigma_0} \right) \exp\left(\frac{-\Delta H_{sol-ppt}}{RT} \right) \tag{24}$$

Cavitation is also likely to happen. Cavity formation usually accompanies creep in tension and can be the controlling factor for creep of some materials. It is a typical grain boundary mechanism which occurs often in polycrystalline materials, but it is not as active in compression as it is in tension; unless high magnitudes of stresses are involved in compression creep [47]. The creep law stating cavitation mechanism [46] can also be expressed in the following way

$$\dot{\varepsilon}_{cav} = \frac{k}{\eta} \frac{V_f^3}{\left(1 - V_f\right)^2} \sigma \exp\left(\alpha\sigma\right) \tag{25}$$

$$\eta = \eta_0 \exp\left(\frac{\Delta H_{vis}}{RT} \right) \tag{26}$$

$$\dot{\varepsilon}_{cav} = \frac{k}{\eta_0} \frac{V_f^3}{\left(1 - V_f\right)^2} \sigma \exp\left(\alpha\sigma\right) \exp\left(\frac{-\Delta H_{vis}}{RT} \right) \tag{27}$$

The rate of flow from the cavities, the total number of pockets and the fraction of the cavitated ones need to be defined [46]. k and α are empirical constants, η is the apparent viscosity, ΔH_{vis} is the apparent activation enthalpy for the viscosity of the bonding phase material in the pockets and multigrain junctions, and V_f is the volume fraction of the bonding phase.

1.5 Creep of ceramics

The undertaken experiments for the determination of creep behaviour of ceramics are numerous; however those dedicated to refractory materials turn out to be less frequent. Large interest was shown for advanced technical ceramic materials dedicated to many applications, for example as part of gas turbines, turbochargers and heat exchangers intended for aerospace, also for nuclear, automotive, electronics and biotechnology industries. The main technical advanced ceramic materials are Ceramic Matrix composites (CMCs) [48, 49], alumina/SiC micro-nanocomposites [20], silicon nitride [27], whiskers reinforced ceramics (SiC-whisker-reinforced Al_2O_3), glass-bonded ceramics (sintered Si_3N_4) and powder compacts (Siliconized SiC) [50], sol-gel derived mullite ceramics [21], ZrB_2-SiC composites [51], mullite or zircon-mullite-zirconia (ZMZ) [52] and ceramics for glass industry belonging to the AZS system [53]. All those materials are bi-phasic or multi-phasic systems having grains/matrix with sizes in the range from nanometres to few micrometres. The grain size can be even larger in case of AZS refractories.

Creep under tensile deformation differs from creep under the compressive deformation. Creep deformation of ceramics is activated by several displacement mechanisms. The early stage of deformation is characterized by the material transfer from compressive grain boundaries to

tensile grain boundaries [54]. In the case of a bonding phase the deformation may stop after the grains eventually come into contact. In some special cases creep can be controlled mainly by cavity formation and growth under tension, while in compression it is more controlled by solution-precipitation.

1.5.1 Creep of silicon nitride and silicon carbide ceramics

Wiederhorn [46] discussed the creep behaviour of particulate ceramic composites (silicon nitride and silicon carbide) in tension and compression at temperatures up to 1400 °C. The important properties controlling creep resistance are the refractoriness of the phases located at the grain-boundaries and their volume fraction. The more refractory the second phases, the more the material is resistant to creep. In addition, a lower volume fraction of the bonding phase leads to a higher creep resistance. *Q. Wei et al* [55] studied the microstructure evolution of a self-reinforced silicon nitride associated with high temperature tensile creep process. The loads were applied from 60 MPa to 140 MPa at temperatures between 1100 °C and 1275 °C. They observed with extensive transmission electron microscopy (TEM) strain whorls, different types of dislocations, grain boundary sliding and cavities in certain samples. The major creep mechanism was concluded to be dislocations starting mostly from the grain boundaries. They assumed that grain boundary sliding and cavity formation contributed to the accelerated creep failure at high temperature, whereas at lower temperature creep was more controlled by diffusion.

The tensile creep of silicon nitride ceramic, sintered with additions of Yb_2O_3 and SiO_2, was studied by *Cao et al* [56]. The investigated temperatures were 1300 °C and 1400 °C under applied stresses from 125 MPa to 200 MPa. The specimens tested led to failure without observation of the tertiary stage. Transmission electron microscopy (TEM) observations revealed that the dominant creep mechanism was not cavitation in that case. Tensile creep behaviour of reaction-sintered ceramics was determined by Ienny *and* Boussouge [57]. Silicon nitride (RBSN) and silicon carbide (RBSC) were tested at temperatures up to 1200 °C and 1300 °C, respectively. Different stresses ranging from 10 MPa to 100 MPa were applied with or without unloading. Phenomenological and rheological models were used to describe transient creep. Viscoelastic deformation dominated the creep of RBSN, whereas RBSC exhibited viscoplastic creep behaviour. Creep of RBSN was assumed to be controlled by the bulk oxidation through the open porosity. Further measurements of this material were performed with pre-oxidation in air at 1050 °C in order to reveal this effect. As a consequence, creep resistance decreased with higher oxidation time.

The effect of heat-treatment by annealing (furnace or microwave) on creep behaviour of self-reinforced silicon nitride ceramics Si_3N_4 were considered by Q. Wei *et al* [27]. Several tensile stress levels were applied and three creep stages were detected at 1200 °C and 100 MPa. Both furnace and microwave annealing enhanced the creep resistance of the material with microwave annealing presenting the most significant effect. High amount of multiple-junction cavitation and

a significant devitrification of the amorphous phases in the microwave annealed specimen were perceived.

1.5.2 Creep of ceramic matrix composites (CMCs)

A large participation for the investigations of several CMCs with respect to creep mechanisms and damage are available in the literature. *Lamoureux et al* [58] studied the effect of damage on creep behaviour of alumina fibre reinforced silicon carbide composite with the microcomposite model approach on the basis of several results. He pointed out a progressive fibre-matrix debonding induced by their creep rate mismatch, causing tertiary creep and a decrease of the longitudinal elastic modulus. Another research from *Lamoureux et al* [59] demonstrated the creep behaviour of alumina fibre/silicon carbide CMC characterized by a short primary stage followed by one or two tertiary stages. The secondary stage was limited to a single point. The mechanisms were controlled by viscoplastic creep of the alumina fibre or damage accumulation within the composite. Creep tests were carried out at a temperature of 1100 °C and stresses of 100 MPa and 170 MPa, with unloading-reloading cycle of 2 MPa/s. The two tertiary stages presented different damage mechanisms; the first one was related to fibre-matrix debonding only, whereas the second one successive fibre failure was dominated at low creep stresses only. *J.L. Chermant et al* [60] resumed more than 10 years of research on creep of CMCs reinforced by long ceramic fibres in ceramic or glass-ceramic matrix. Primary and secondary stages were mostly detected. The stresses and the temperatures causing creep were low. In air or argon conditions, stresses were lower than 400 MPa and temperatures were below 1400 °C and 1100 °C for CMCs with the ceramic matrix and the glass-ceramic matrix, respectively. Creep of CMCs reinforced by continuous ceramic fibres with a ceramic matrix is controlled by damage creep mechanism, while creep for those with a glass ceramic matrix is controlled by the creep of the fibres above 1000 °C. They observed brittle damage creep mechanisms operating for these CMCs in two steps: matrix microcrack development until its saturation followed by an opening of some of these microcracks. Under certain conditions the latter enables creep of SiC fibres which bridge the microcracks.

The effect of oxidation on the creep behaviour fibre-reinforced CMCs was modelled by Casas *and* Martinez-Esnaola [61]. The model took into account the interface and matrix oxidation and was compared to experimental results at 1000 °C and 1100 °C with stresses between 115 MPa and 300 MPa. The fraction of broken fibres increased and accelerated with time due to load transfer and fibre degradation. Unstable failure of the composite was concluded to be caused by a fraction of about 15% of broken fibres.

Long-time tensile creep and also rupture of a 2D-woven SiC fibre-reinforced SiC matrix composite was investigated under air at 1315 °C and several stresses [62]. Three different SiC fibres and three different SiC-based matrixes were compared. Primary, secondary and sometimes tertiary stages were detected. The dominant factor, controlling creep and rupture properties of the composites, was the creep of the fibres. The formation and growth of most matrix microcracks

originated from the specimen surface. Through the whole specimen thickness matrix-cracking was not observed for creep over a period of 100 h. As the fibres were more creep resistant than the matrix, stresses were relaxed with time at the crack tip. Matrix crack growth was stopped until oxidized fibres breakage occurred in a matrix crack wake. It was also noted that a true steady-state strain rate condition was never achieved due to the fibres themselves that showed strong primary creep and also to stress transfer from matrix to fibres during creep of the composites. Creep resistance of a ceramic material is enhanced considerably by adding second phases. The addition could be a dilute arrangement of fine particles or multidimensional tows of continuous fibres infiltrated in matrix phase.

A review of available models of creep behaviour and mechanisms in multiphase ceramic materials was given by David S Wilkinson [50], where particular attention was paid to whiskers reinforced ceramics, infiltrated powder compacts and glass-bonded ceramics. Models based on viscoplastic creep of the matrix phase showed that creep can be controlled by a combination of matrix flow, dissolution-precipitation creep and cavitation.

Cyclic creep and recovery behaviour of an oxide-oxide continuous fibre ceramic composite, CMC, was studied in steam environments at 1200 °C for maximum stress levels of 100 MPa and 125 MPa [48]. Primary creep stage was mainly detected. For an applied stress, creep rate and accumulated creep strain were lower in cyclic creep-recovery than in sustained creep experiment. Strain recovery led to improvement in creep lifetime. Presence of steam affected the cyclic creep recovery behaviour of some CMCs; strain recovery was lower compared to the one in air. Regions of fibrous fracture were noticed for creep-recovery tests under air. Steam environment had a dramatic effect on the fracture surface.

Long-duration creep performance of SiOC containing composites material reinforced with fibres was considered at temperatures up to 1200 °C [49]. All measurements showed a period of primary regime and constant strain rate without tertiary creep. Creep of CMCs samples with fibre orientation of ± 45° was matrix dominated with pronounced primary stage. The steady state creep was attributed to viscous flow behaviour of the SiOC in the matrix. In the CMCs samples of 0°/90° fibre orientation creep was independent of oxidation. It was rather dependent on the granular structure of the fibre. The change of the microstructure of the fibres to coarser and non-uniform shape led to a reduction of the secondary stage and modification of the diffusional creep.

Tensile creep of a novel mullite fibre at temperatures equal to 1100 °C and 1300 °C was performed by Almeida *et al* [63]. Only primary and secondary creep stages were observed, followed sometimes by failure with the absence of the tertiary stage, and creep deformation was not detected at lower temperature. Most of the tested fibres had what the authors called an elastic-pseudo-plastic behaviour associated with grain boundary sliding mechanism at 1400 °C. Two main determinant aspects for the mechanical behaviour of the mullite fibre came out of these results: microstructure heterogeneity for the total deformation and density of defects for the strength.

High temperature tensile creep, fatigue and fracture of single or multiphase ceramics, i.e. mullite and ZMZ, with additional glass/liquid phase were discussed by Davies *et al* [52]. The specimens

ended with fracture after only a continuously decelerating primary stage in case of mullite and mostly after a tertiary stage for ZMZ. Experiments were performed at temperatures between 1200 °C and 1400 °C and several applied loads. All experiments ended with growth of a single crack. The cyclic fatigue periods were the longest because of the viscous crack bridging and crack healing while unloading. The authors concluded on an initial flow of the viscous glassy phase that was substituted by solution/precipitation when the grains lock up. Tertiary creep was denoted as a result of cavitation damage in the liquid phase.

All previously discussed creep investigations of advanced ceramics were carried out at high applied stresses (approximately hundreds of MPa) and at moderately high temperatures (from 1000 °C to 1400 °C), which are significant service conditions for this category of materials. In comparison to ordinary ceramic refractories the operating conditions do not attain such high stresses but can reach high temperatures like e.g. 1600°C.

1.5.3 Creep mechanisms of advanced ceramics under compression

More than three decades ago compressive creep was already investigated by Tsai *and* Raj [64] for MgO-fluxed hot pressed Si_3N_4 assuming solution-precipitation mechanism. Kinetic data for the dissolution rate of β-Si_3N_4 in Mg-Si-O-N glass were utilized. Creep happened by solution-precipitation process as the fine-grained hot pressed Si_3N_4 contained amorphous phase in grain interfaces. Creep under uniaxial compression was applied at a temperature of 1400 °C and for a stress range from 100 MPa to 500 MPa. Solution-precipitation creep could be controlled either by the transport of atoms across the fluid/crystal interface or by diffusional transfer of atoms through the fluid medium [65]. The two steps acted in series and the slower one was assumed to be rate controlling. Tsai *and* Raj relying on previous studies opted for the interface reaction for creep in hot-pressed Si_3N_4 without taking into account the influence of the grain size. With monitoring the density they ensured that the measured strain did reflect deformation only and not cavitation. Theoretical estimations of creep rates were in good agreement with the experimental results. Further studies revealed the importance of secondary glassy phases and β-Si_3N_4 particular grain morphology for the influence on creep resistance of the material. Creep deformation mechanisms in compression for silicon-nitride materials could be viscous flow, grain boundary sliding, solution-precipitation, etc. and several models were developed to explain their particular properties. Melendez-Martinez *et al* [66] studied two sintered silicon nitride based ceramics at temperatures from 1450 °C to 1700 °C with argon atmosphere and applied stresses from 5 MPa up to 90 MPa. Creep curves showed no significant transient state and steady states were reached almost immediately after each stress change. The crept specimens presented no evidence of macroscopic failure. The use of scanning electron microscopy (SEM) after creep measurements revealed an absence of dynamic grain growth and some cavities around the grain boundaries. No intra-granular cavities formation was detected.

Another interesting study of long durations compressive creep behaviour in air of precursor-derived Si-C-N ceramics was completed by Thurn *et al* [67]. The temperature range was between 1200 °C and 1550 °C under compressive stresses from 30 MPa to 250 MPa. Stationary creep was not reached even after long time testing. Temperature dependency of creep behaviour for such materials turned out to be extremely low. For temperatures up to 1500 °C a dense inactive oxide layer was detected on the surface of crept specimens. However, at 1500 °C no oxidation layer was found, but an area of high porosity near to the surface representing specimens' decomposition. The behaviour of the tested materials in terms of oxidation was controlled by the formation of silica layers at the surface. As there are no grain boundaries and intergranular oxide-type phases, there is no internal diffusion of oxygen along grain boundary phases.
Microstructure and high temperature compressive creep properties of alumina/zirconia ceramics, manufactured by powder processing or sol-gel precursors processing, were investigated [22]. Creep tests were carried out at temperatures from 1300 °C to 1450 °C under stresses from 10 MPa to 150 MPa. Depending on the applied stresses and temperatures, brittle fracture, plastic behaviour or even some softening behaviour without failure were observed in the crept specimens. The results showed that the addition of 5.5 vol% zirconia particles to alumina matrix did not improve the creep resistance. Models correlating the microstructural evolution and the creep parameters were established to detect the predominant creep mechanism. Creep started by grain boundary sliding and was complemented by cavities formation. For powder processed materials showing large monoclinic zirconia grains at grain boundaries, linkage to cavitation was facilitated, whereas for sol-gel processed ceramics with tighter grain size distribution of small tetragonal zirconia grains cavities were present but showed lower microcracking activity.

1.5.4 Creep mechanisms of advanced ceramics under bending

Tensile creep of ceramics was also determined by means of 3-point or 4-point bending experiments. Ivankovic *et al* [21] reached temperatures in the range of 1320-1400 °C under stresses between 40 MPa and 160 MPa intended for 4-points bending creep of sol-gel derived mullite ceramics with mono-modal and bimodal distribution of grain sizes. The mono-modal exhibited the highest creep rate with low grain size (0.6 μm). After creep measurements the change in microstructure was obvious. Intergranular fracture was predominant near the tension surface and transgranular more planar fracture was predominant near the compression surface zone.
Reveron *et al* [20] also investigated 4-point bending creep behaviour of pressureless sintered alumina/SiC micro-nanocomposites obtained by slip-casting. A temperature of 1200 °C in air and a stress of 100 MPa were applied and the results compared to pure alumina materials. A high purity Al_2O_3 powder and a SiC fine powder were used. Two suspensions containing 1% vol and 5% vol SiC were obtained. The composite with 1 vol% SiC had lower amount of SiC particles located on the grain boundary than the composite with 5 vol% SiC. The volume of added SiC particles located on the grain boundary was much lower for 1 vol% SiC than the one for 5 vol%

SiC. The large SiC particles (having a high mean size) were mainly located at the alumina grain-boundaries and almost all SiC particles with low mean size were bounded into alumina grains. Higher toughness and hardness of the composite were noticed with SiC addition. For 1 vol% SiC creep resistance was governed by the grain size in the matrix, whereas for 5 vol% SiC better creep resistance was achieved with the assumption that the SiC particles situated between adjacent grains may have contributed to reduce grain-boundary sliding. Primary creep was detected and creep resistance was considerably improved in materials containing 5 vol% of SiC. Lin *et al* [23] studied the grain-size effect on flexural creep deformation of alumina-silicon carbide composites. The material studied was alumina reinforced with 10 vol% SiC whiskers. The measurements were conducted at 1200 °C and 1300 °C and under stresses from 50 MPa to 230 MPa in air. Grain boundary sliding mechanism was discerned at 1200 °C with grain offset and grain rotation. Creep resistance at this temperature rose with rising matrix grain size. Nevertheless at higher temperature creep rate was noticed to be insensitive to grain size increase due to the development of cracklike cavities. SEM observations showed that the predominant sites for cavity nucleation and growth were the grain boundary facets (two-grain junctions) oriented perpendicular to the stress axis in the case of coarse-grained materials. Fine-grained materials showed on the contrary that prevalent sites for cavity formation were triple-grain junctions. It was also noticed that the amount of the amorphous phase present at whisker-alumina interfaces did not depend on alumina grain size; it was not a determining factor in the creep results.

1.5.5 Creep mechanisms of refractories under compression

Research about tensile creep mechanisms of ordinary refractories is at the present time non-existent. On the other hand it is not unlikely to find few outcomes of these materials tested for compressive creep. Creep mechanisms in corundum ceramic over a wide range of test conditions were studied by Bakunov *et al* [68]. Experiments at temperatures from 1300 °C to 1900 °C and stresses between 0.5 MPa and 50 MPa were carried out. The materials mainly worked in the region of the action of mechanisms like surface diffusion, creep along the grain boundaries, or by a combination of these mechanisms. In the region of loads up to 10 MPa (relatively small), surface diffusion effect was the most likely to happen. Concentration of impurities, porosity, shape of the crystals, etc. would influence the settled regions. Snowden *and* Pask [25] developed a study on the high temperature creep behaviour of MgO-$CaMgSiO_4$ (monticellite, CMS) refractory system. Compressive creep tests were conducted in air from 1200 °C to 1450 °C, where the steady state region was determined. Three distinct stages of typical creep curves were not always revealed. A complex deformation process involving simultaneous mechanisms with increasing temperature was observed. At low temperature and high applied loads creep was controlled by dislocation processes in the MgO crystals; the silicate boundary phase being highly viscous was unable to deform independently. For higher temperatures and low applied loads

viscous flow deformation of the boundary regions was the dominating mechanism, which resulted in a gradual break of the MgO framework.

Compressive creep of calcia-silicate (CaO/SiO_2) containing MgO refractories was detected by Wereszczak *and* Kirkland [69]. Commercially-available brands were tested over a temperature range of 1400-1550 °C and stresses of 0.1-0.3 MPa. MgO content was greater than 96 wt%. All brands showed a minimum C/S ratio equal to 1.9 wt% and a firing temperature exceeding 1535 °C. Specimens were soaked and loaded sequentially at three different stresses from 0.1 MPa to 0.3 MPa for 225 hours. Contraction was observed during the initial 15 h to 20 h soak. It is believed to be due to some microstructural rearrangement and/or sintering happening in the material. All brands had similar general appearance of creep curves with different creep resistance which was affected by the relative amount of impurities, type of phases present, porosity and grain size distribution. High MgO content and C/S wt% ratio were not efficient indicators for a better creep resistance. However, larger average grain size and wider size distribution, low iron content and absence of $CaO-MgO-SiO_2$ ternary compounds would improve the resistance to creep. Transient creep was characterized by a long duration of slowly decreasing creep rate. Steady-state creep was rarely achieved and tertiary creep never observed. Some brands showed a stress exponent indicative of the diffusion mechanism dominance, while the activation energies suggested that creep was accommodated by grain boundary sliding through viscous deformation of the calcium-silicate boundary phase. Other brands were believed to have endured high contraction, time hardening effects, or more than a single active deformation mechanism.

Investigations of creep mechanisms of refractories under compression could be found in the literature, but not in great numbers. Many of them, despite of determining the creep parameters with a power law expression of the creep rate, do not venture describing the occurring mechanisms, which makes sense from a perspective of heterogeneous refractory materials. Among these studies can be sited the creep of CaO/MgO refractories [70], compressive behaviour of ACS torpedo bricks [43] or compressive strength and creep behaviour of magnesium chromite refractory [44].

1.6 Creep testing methods

Refractory ceramics performance can be affected by high compressive loads and tensile constraints at elevated temperatures. For refractory selection and development, lining design and avoidance of failure it is important to perform creep experiments both under tension and compression. The available standards concerning refractory materials are Creep In Compression (CIC) [71] and Refractoriness Under Load (RUL) [72]. For both testing methods the specimens are of cylindrical shape and the applied load is not high enough to represent the conditions in service [77]. Furthermore, because deformation takes place while heating up of the specimen, creep possibly occurs before the final temperature is achieved. The RUL gives the temperature at which the specimen shows a defined deformation. The temperature increases with a rate of 5 K/min and the applied compressive load is constant and equal to 0.2 MPa at maximum. CIC

measures the variation of the specimen length under constant compressive load and temperature. The method of measuring CIC is differently standardized in the applied load, heating rate and specimen dimensions according to national standards [73]. Creep assessment of ordinary ceramics is standardized only for compressive testing. Presently there are no existing standards that define high temperature tensile creep testing of heavy ceramics, which are heterogeneous with respect to microstructure and grain size. On the other hand developed tensile creep testing equipment and standards for advanced technical ceramics are numerous.

1.6.1 Compressive creep testing of refractories

High temperature creep under compression of ordinary refractory ceramics was largely investigated in the preceding years [74, 75 and 76], often more frequently comparing to tensile testing since fewer restrictions are involved for the former, like specimen shape, gripping and alignment during testing.

Refractoriness under load and hot creep measurements of refractory ceramics were reviewed by Matsumura *et al* and the standards available from different countries were compared [71]. The difference of creep testing experiments remain mostly in the size of the tested specimen, the material of loading rod, the applied load and the heating rate. The aim of refractoriness under load (RUL) is to assess softening behaviour of the material in dependence of temperature, while creep in compression (CIC) intends observing the material deformation at selected service temperatures. This paragraph will mainly discuss essential compressive creep studies related to ordinary ceramic refractories including specimen geometry, testing conditions and apparatus when available.

Compressive creep behaviour of ACS torpedo bricks was studied by Andreev *et al* [43]. Experiments were carried out on samples immersed in coke particles with a constraint of 100 N during the heating up period (heating rate 4 K/min). The temperature ranged from 800 °C to 1400 °C and the applied loads from 10 MPa to 40 MPa. Several specimen designs were employed, among them the cylindrical one with 30 mm dimeter and 50 mm height. Primary and secondary creep regimes were attained for all curves. Tertiary creep, defined by increasing strain rate, was also observed in some of them.

Compressive strength and creep behaviour of magnesium chromite (20 wt% MgO and 80 wt% Cr_2O_3) refractory in nitrogen atmosphere was investigated by Krause [44]. Creep measures were carried out at a temperature range from 1300 °C to 1600 °C and applied loads ranging from 1.4 MPa to 5.6 MPa. A linear voltage displacement transducer with a sensitivity of ±1 µm was monitoring the crosshead displacement while the specimen deforms. Creep experiments lasted from 3 to 170 hours when no steady-state regime was attained. Specimens with dimensions of $8\times9\times18$ mm^3 were diamond-sawed and diamond-grounded to have bearing faces as flat, parallel and perpendicular to adjacent sides as possible. A preload of 50 N was applied to take into consideration the alignment and thermal expansion of the material during heating up; the crosshead movement was monitored automatically by the machine (10 % variation).

Molybdenum disilicide resistive heating elements were used to be able to reach temperatures up to 1600 °C. The furnace was heated in 20 minutes until 1200 °C, afterwards at a heating rate of 20 K/min up to the target temperature. One hour dwell time was added to get a homogenous temperature equilibration. Jin *et al* [77] investigated the compressive creep testing at elevated loads and temperatures of shaped and unshaped refractory ceramics. They applied service related creep loads between 0.5 MPa and 9 MPa and temperatures ranging from 1100 °C to 1550 °C. The materials studied were burnt magnesia-chromite bricks and an ultra-low cement high alumina castable. A spindle-driven universal testing machine supplemented with an electrical furnace was employed to reach loads up to about 20 MPa. The specimens, prepared by diamond-grinding, were of cylindrical geometry with dimensions of 35×70 mm². A height/diameter ratio of 2 was necessary to avoid that friction of the end faces affects the measurements. The recording of the displacement was ensured by a rear and a front extensometer with an initial gauge length of 50 mm. The change of the end face of the upper piston into a spherical surface helped to avoid uneven loading during creep testing. The preheating was performed with a rate of 10 K/min and a low preload.
A report from Ferber *et al* [78] sums up a research about compressive creep and thermo-physical performance of refractories regarding creep testing, specimen preparation, data interpretation and microstructural characterization. They carried out experiments at a temperature range from 1300 °C to 1650 °C and several applied stresses depending on the material tested. For the measurements, the compressive creep frame of the testing device was equipped with an electrically heated furnace. Either a digitally controlled pneumatic or hydraulic drive controlled by an analogue controller was employed. Several refractory materials were tested; silica, mullite, fusion-cast alumina and fused spinel refractories. Specimen preparation was depending on the tested material. For instance in the case of the silica and mullite refractories, cylindrical specimens having dimensions of 25.4×76.2 mm² were core-drilled. The deformation of refractories was measured using at least two linear variable differential transducers (LVDTs), which is until now an efficient and accurate measurement method, as long as the recorded deformation coincides with the specimen heights measured before and after testing.

1.6.2 Tensile creep testing of advanced ceramics

The investigated studies about tensile creep process of ceramics at high temperature remain mostly dedicated to fine technical ceramics quoted previously. Adequate and efficient standards including tensile creep have been developed for these categories of fine structural ceramics (ISO, ASTM, CEN and JISC) defining specimen design, testing assembly and detailed measurement approaches. A listing of the existing standards related to tensile creep of ceramics is available in Refs [79, 80]. It is of high interest to consider some relevant tensile creep tests designed for this type of materials in addition to those for refractories.

Ferber *et al* [81] studied the high temperature stress sensitivity of the creep rate for commercially available alumina (94% Al_2O_3) and silicon nitride ceramics, which are used as structural components in advanced automotive gas turbine engines. Button-head specimens were gripped outside the compact heating furnace that is capable of heating at temperatures up to 1600 °C. The cold grips were connected to the load frame by hydraulic couplers to reduce bending. A direct-contact capacitance extensometer was recording the deformation during testing with a resolution lower than 1µm. The materials were machined with a numerically controlled four-axis grinder into button-head specimens. The gauge section of the specimen was equal to 6 mm in diameter and 25.4 mm in length. Three creep stages could be achieved until failure for silicon nitride at 1200 °C and loads between 20 MPa and 32 MPa. Regarding alumina material, transient or steady state regimes mostly followed by failure, were revealed at a temperature of 1000 °C and loads ranging from 21 MPa to 39 MPa.

The tensile creep investigation from Ienny *and* Boussuge [57] for the determination of tensile creep behaviour of RSSC and RBSN was made with specimens having an overall length of 100 mm and a gauge length of 20 mm. Thermal gradient in the gauge length was not higher than ± 10 K. Cylindrical test pieces of mullite and ZMZ investigated by Davies *et al* [52] for high temperature tensile creep were manufactured with 150 mm length and 9 mm diameter with a reduced gauge length of 20 mm and a gauge diameter of 5 mm. Both ends of the specimens were gripped to water cooled chucks. Cao *et al* [56] performed tensile creep measurements with flat dog-bone specimens having a total length of 70 mm and a rectangular cross-section of 4×2.5 mm² in the gauge area. The gauge length measured 20 mm. Creep tests were performed under air using a dead-weight loading apparatus. The furnace was equipped with six $MoSi_2$ heating elements ensuring a maximal temperature error of 5 °C. Specimen ends were fixed in hot grips via four SiC pins connected to SiC loading fixtures. Optical image analyser was employed to measure the displacement of the inner positions of the hot grips. Bending strain expressed as percent bending could be reduced to a value lower than 5 % for an applied stress of 60 MPa at room temperature. Details of the percent bending calculation are present in [56]. Specimens where heated with a heating rate of 15 K/min and 15 min dwell time under a preload of 98 N.

For the study of Nextel 610 reinforced polymer derived CMCs at 1000 °C [49] a Kappa 050 creep testing machine (Zwick) was utilized according to DIN EN 1893:2005 [82]. A constant heating rate of 30 K/min and a dwell time of 10 min were applied. The recording of the strain was done with a laser system at both ambient and high temperatures. Dog bone shaped specimens were manufactured with the gauge section dimensions equal to 180 mm length and 15 mm width. The gauge length for displacements measurements was equal to 25 mm.

The previously announced tensile and creep testing of a novel mullite fibre at high temperatures [63] was performed under the following conditions: single filament tensile experiments were accomplished according to DIN EN 1007-4 and 1007-6 [83]. Two SiC heating elements were employed in a furnace that achieved a temperature of 1400 °C. The gauge length utilized for displacement measurements was equal to 25 mm. In order to achieve a better control of the applied load a dead load system was utilized.

These testing methods for tensile creep of advanced ceramics were interesting to consider in terms of the reached temperatures and employed furnace, specimen geometry, displacement measurements or holding systems. The chosen machine characteristics are indeed suitable for these categories of fine ceramics; nevertheless they would not be totally efficient when applied to ordinary ceramic refractories due to their high heterogeneity.

1.6.3 Tensile testing of refractories

Moreover, not numerous but sufficient amount of investigations for high temperature uniaxial tensile testing of refractories, without measuring creep, could be found in the literature. An ancient study [84] that was established 80 years ago depicted some refractory properties under tensile loads, for e.g. tensile strength and Young's modulus. Several brands of fireclay bricks representing a large range in silica content and obtained from different manufacturing methods were investigated. The specimens were of cylindrical shape with shoulders and flanges. Their dimensions were adopted after trying 3 different methods of obtaining specimens from the individual brick. The length of the tested specimens was decided to be either 114.3 mm or 161.93 mm, corresponding to 50.8 mm and 76.2 mm gauge lengths, respectively. The cross sectional area of all specimens was equal to 38.1 mm² in the gauge segment. Sections were cut crosswise and lengthwise to the bricks. The testing machine was of counterbalanced simple beam type (lever type) with aligning bearings and was assembled with Tuckerman optical strain gauges [85]. The tested specimens were held with porcelain grips which were supported by porcelain clamping rings. The reason was that the machine was intended for studying the tensile properties of refractories at elevated temperatures. The results showed that the properties of the lengthwise specimens were better than those of the crosswise ones. However, their strengths were approximately equal and Young's modulus of the lengthwise specimens was lower than the crosswise ones.

Tensile and compressive behaviour of magnesia carbon refractories was determined by Schmitt *et al* [86]. They examined the Young's modulus and tensile strength of two materials, one bonded with phenolic resin and the other one with pitch. The study included, inter alia, a uniaxial compression crushing test and a special uniaxial tensile testing forced by an elastic restraint to deform homogeneously. Non-symmetrical compression-tensile material behaviour and presence of nonlinear domain were revealed. To overcome the early strain localisation that occurs during tensile loading and to delay the initiation of microcracking a special setup, developed formerly [87, 88], was employed. The principle is based on first having aluminium bars fixed on the lateral faces of the specimens (specimen dimensions 160×80×40 mm^3). The load is then transmitted through these bars secured with the grips of the testing machine. Strain gauges were in contact with the bars and the specimen to guarantee the uniformity of the displacement. The central zone could therefore undergo uniaxial loading. A strain rate of 1.5 10^{-5} s^{-1} was applied during loading. The specimens showed a linear elastic behaviour followed by hardening-softening regimes owing to emergence of microcracks around the aggregates. Nazaret *et al* [89] also performed uniaxial

tensile testing with two refractory materials: andalusite and cordierite reinforced with short steel fibres based refractory castables. The testing machine was a servo hydraulic universal type. Extremities of the sample were glued on metallic plates, which were water-cooled. The central part of the specimen was covered by the furnace capable to provide a maximum temperature of 1400 °C. The specimen showed a reduced cross section of 30×25 mm². The strain was measured with two high temperature extensometers with gauge length of 12.5 mm. This assembly allowed measurements in the range of 20-900 °C. Monotonic or cyclic loading/unloading tests were carried out. Kakroudi *et al* [90, 91] studied the pure tensile properties of refractory castables at different temperatures, from 20 °C to 1200 °C. An electro-mechanical universal tensile testing machine was utilized. The specimen had a shape of a cylindrical rod of 18 mm diameter that was glued with two metallic parts. Additional machining of the system was made in order to improve the symmetry. Strain variations were measured by silicon carbide rods of two extensometers placed in parallel. The gauge length was equal to 25 mm. The material reached displacement values at rupture between 3 μm and 5 μm. Tensile behaviour of magnesia-spinel refractories was investigated by Grasset-Bourdel *et al* [92] using the same uniaxial tensile equipment, however the final central diameter obtained after machining was equal to 16 mm. The specimens utilized were prepared from a cylindrical road of 20 mm diameter and the gauge length remained as quoted above.

1.6.4 Tensile creep testing of refractories

It is nevertheless not impossible to find investigations about tensile creep of ordinary ceramics at elevated temperature. One of the first researches that brought about tensile creep of refractory bricks was made almost 70 years ago by Mong [76]. He exposed different brands of firebricks to creep measurements. The measurements were performed at temperatures from 25 °C to 950 °C during long time periods (approximately 240 days). Specimens were attached to porcelain load links. Cylindrical specimens with a length of 228.6 mm and a minimal diameter of 25.4 mm have been used. The temperature variation of the furnace was controlled to be from less than 3 °C to about 9 °C after the heating units deteriorated. The temperature was increased with a rate of approximately 40 K/h and kept constant for 3 hours. Kandil *and* Dyson [93] developed a tensile creep testing facility intended for glass ceramics and refractories up to a temperature of 1500 °C. The furnace was of cylindrical shape with a height of 165 mm; maximum temperature variation was believed to be less than ±2 K. The sample was glued to metallic caps by an adhesive. It was machined from a solid cylindrical rod to 9.4 mm diameter and 270 mm length. The gauge section was of 22 mm in length and of 4 mm in diameter. Bending stresses were reduced to values within ±2 %. Details of bending measurement are available in [93]. The test piece was heated with a rate of 10 K/min and a low applied preload. Tensile creep experiments of reaction-bonded silicon nitride (RBSN) were carried out at 1450 °C to assess the capability and accuracy of the system. Tensile tests of this material were also performed at room temperature. Bisson *and* Regent [94] proposed a high temperature tensile testing apparatus for industrial ceramics showing

heterogeneous and coarse microstructure. Specimens with rotational symmetry were 230-320 mm long. The central diameter was 20-30 mm. The ends of the specimens were also attached by cold grips. A short furnace allowed experiments up to a temperature of 1500 °C.
A tensile creep facility intended for creep measurements of refractory ceramics up to 1600 °C was established by Rendtel *and* Hübner [95]. Displacements were measured by flag-based scanning laser extensometers on hot-pressed silicon nitride samples at 1500 °C. A screw-driven universal testing machine with a load train comprising a sintered α-SiC upper and lower pull-road connected to grips via pins. Flat dog bone specimens geometry with a cross section of 2×4.6 mm² in the gauge segment and a gauge length of 38 mm were utilized. Specimen ends were fixed to upper and lower grips by in all four α-SiC pins. The specimens, the grips and the end of the pull rods are housed by a chamber furnace with a volume of 150×150×150 mm^3.
It is obvious that there is a lack of knowledge in investigating tensile creep of ordinary ceramic refractories because of the several criteria that have to be met in order to accomplishing reliable and accurate measurements. Specifications like recording small displacements (in μm level) at high temperatures, ensuring accurate alignment in order to reduce bending considerably, uniform and uniaxial stresses distribution during loading, and a suitable and robust gripping system for relatively brittle materials are indispensable.

1.7 Asymmetric creep models

Creep modelling of ceramics turned out to be a valuable tool for their lifetime prediction. As the mechanical structures undergo not only compressive creep but also tensile creep during operation, it is of high significance to take both processes into consideration, especially since they do not act in the same manner [96]. Indeed, early investigations on refractory materials indicated non-symmetrical creep behaviour under tension in comparison with compression [76, 97, 98, 99 and 100]. For instance, Mong [76] concluded on an asymmetrical behaviour between creep under compression and creep under tension for several brands of firebrick. Moreover, asymmetric creep behaviour could be more pronounced when a glassy phase surrounds the grains [101]. In tension, a separation of grains in the direction of loading may occur and creep may be influenced by a viscous phase. Whereas in compression, grains can come into contact and exert pressure onto one another thereby modifying the microstructure. Damage can also be an influencing process, as it is more sensitive under tension than under compression due to the onset of cavitation in the former one [97, 50]. Ferber *et al* [81] attributed these creep dissimilarities to the generation of creep-induced damage zone under tension (creep cavitation effects) that augments the creep rate. Based on tensile-compressive asymmetric creep model, Chuang *et al* [102] suggested power-law creep functions using the parameters of effective stress/strain. Finite element method was applied to study the long-term compressive creep deformation of a siliconized silicon carbide ceramic Si-SiC C-ring at 1300 °C. They utilized an asymmetric creep function by generalizing a symmetric creep equation with different creep constants in tension and compression. The sign of the largest principal stress in magnitude determined the asymmetric

creep response. Lim *et al* [103] indicated that if there is a small difference in magnitudes between tensile and compressive principal stresses this model is then questionable. Accordingly, the authors generated a finite element model for high temperature asymmetric creep behaviour of alumina and siliconized SiC ceramics. They analysed creep response of ceramic structures with general loading conditions via finite element calculations in Abaqus. Details of the proposed model are available in ref. [103]. The simulations were compared to experimental results from the literature for siliconized SiC (C-rings) under compression and for alumina and siliconized SiC under bending. Multiaxial creep equations were proposed and implemented into a user subroutine (UMAT) of Abaqus with considering elastic and creep behaviour only; damage was not considered. Finite element calculations for the variation of creep strain with time were in good agreement with experimental bending data for alumina specimens at 1000 °C. However, this agreement was achieved only for principal stresses smaller than the threshold stress of creep damage. The difference between experimental and simulated results at higher applied stress was attributed to damage in the tensile region of the specimen under flexion, for the reason that no damage model was considered. For siliconized SiC, finite element calculations assuming non-constant principal stresses were in accordance with compressive creep experiments (Si-SiC C-ring) at 1300 °C and with four-point bending creep experiments (Si-SiC) for the conditions of the cavitation zone. A region bearing tensile stresses exceeding 100 MPa represented the cavitation zone, with fast growing cavities in Si-SiC specimens.

Asymmetric creep deformation of hot-isostatically-pressed Y_2O_3-doped-Si_3N_4 under tension and compression was examined at different temperatures by Wereszczak *et al* [104]. Different compressive and tensile stresses were applied at temperatures between 1316 °C and 1399 °C. Primary and secondary creep stages were observed in both cases. The proposed empirical creep model represented the minimum creep rate in dependence of temperature and was designed for both tensile and compressive stresses. The creep strain rate depended on a product of exponential and linear functions of stress in addition to the creep rate function according to Norton's law with a stress exponent equal to 1. Creep was depicted as being asymmetrical with creep rates more severe in tension than in compression at equivalent stress magnitudes. Microstructural analyses were carried out after creep testing using transmission electron microscopy (TEM). Creep strain asymmetry in tension and compression was essentially due to the variation between tensile- and compressive-stress-induced cavitation amounts. All tensile samples exhibited multigrain junction cavities, while a few of compressive samples showed it at a far less concentrations. Cavity types, size and location also differed for specimens crept in tension comparing to the ones crept in compression. E. Blond *et al* [101] proposed a high temperature asymmetric tensile-compressive creep model to characterize the behaviour of ceramics. The material investigated was a refractory bauxite-based brick utilized in working linings of steel ladles. The model developed is an extension of the Bingham-Norton's rheological model [105, 106], which reflects the different viscoplastic creep behaviour of the material in tension (3 point-bending) and compression. It was simplified with ignoring the viscoplastic dilatancy during creep caused by void or microcrack nucleation and/or growth. Furthermore, the mass conservation of the elementary volume was

assumed in the case the material contained a high content of soft glassy phase. Two mechanisms, assumed being responsible for the deformation, were introduced in the constitutive model: matrix creep that was activated by tensile loads and grains creep, which was rather initiated by compressive loads. Consequently, a decomposition of the stress tensor into positive and negative parts was added in order to illustrate the unilateral behaviour of damage, which was due to opening-closure of microcracks [107, 108 and 109].

Chapter 2: Testing machine design and application

2.1 Introduction

In this research a testing setup was especially designed and adapted for performing tensile creep measurements of refractory ceramics. In the literature mainly facilities for creep-testing of refractories under compressive loading are described. To date, no significant studies relating tensile creep of coarse grained refractories are available. This is due to the various obstacles that could appear in this case, like specimen fastening and alignment, insuring an adequate heating rate that avoids irreversible strain before creep testing, or appearance of bending while applying the mechanical load. Therefore, a feasibility study was accomplished prior to testing, comprising a finite element modelling built with Abaqus software which permitted to determine, inter alia, optimal specimen geometry and heating up schedule. A detailed design and the main features of the tensile creep setup are afterwards described in this chapter as well as the creep testing procedure.

2.2 Innovative setup design and procedures

2.2.1 Choice of the specimen shape

A major questioning for an adapted testing procedure design was the choice of a specimen type and shape compatible with the investigated materials, i.e. coarse-ceramic refractories. Many specimen shapes were considered in the past [110, 111 and 112], the rectangular or the flat dog bone specimens were often utilized in researches that are mainly dedicated to advanced technical ceramics [56, 59, 60 and 62]. The dimensions, mostly rather small, differ according to the materials tested and their applications. Those shapes are complex and their manufacturing could be inappropriate and limited to coarse-ceramic refractories due to the large range of grain sizes from few micrometres up to approximately 5 mm. Advanced technical ceramics differ completely from refractory ceramics in terms of composition, intrinsic flaws and defects, porosity and microstructure. For an adequate and representative tensile creep measurement of ceramic refractories, specimens of sufficiently large volume were needed. Specimens having small proportions would not be suitable due to the size of the biggest grains in refractory ceramics. Consequently the selected geometry was a simple cylindrical one with dimensions of 230 mm length and 30 mm diameter. Drilling a cylindrical geometry permitted to improve even loading and to avoid undesired further stresses. Other advantages of manufacturing cylindrical shapes were a gain in time and prevention from unintentional pre-cracking.

2.2.2 FE simulation prior to measurements and choice of the heating up schedule

For an optimal design of the high temperature tensile creep setup it was decided that both specimen ends would be attached outside the furnace. They were glued to steel adapters which were secured by water-cooled grips. To verify the feasibility of the proposed design with respect to the specimen geometry and dimensions a FE simulation was carried out in advance using the software Abaqus. This preliminary investigation allowed for the prediction of the temperature and stress distributions in the specimen during preheating and creep experiment. It permitted also to estimate these distributions in the hot central zone and at the cold ends. The heated section of the specimen was 100 mm long.

A two-dimensional axisymmetric FE model was established as the specimen shape showed radial symmetry. A simple symmetrical boundary condition at the lower end of the model was applied. Coupled temperature-displacement type was chosen with a mesh comprising 1740 quadrilateral elements. The specimen underwent an increase of temperature from ambient (20 °C) temperature up to 1600 °C followed by a dwell time of 1 h without any preloading. In order to consider an optimal heating up schedule without engendering significant thermal stresses within the sample three different preheating rates were simulated; 2.5 K/min, 5 K/min and 10 K/min. The applied heat transfer coefficient for the heating of the specimen in the furnace was equal to 10000 W/(m².K). This value was taken as an upper limit to represent a worst-case design condition with respect to heterogeneity of the temperature distribution. The heat transfer coefficient should be lower, but the cold end temperature needed also to be taken into account. The water cooling of the specimen ends was therefore modelled with a temperature of 20 °C and a heat transfer coefficient of 500 W/(m².K) (**Fig. 2b)**). Creep was then simulated by applying a tensile mechanical load of 0.25 MPa for 2 h. Norton-Bailey constitutive equation was used for the prediction of the specimen behaviour. Only the creep strain hardening approach was considered in this model [113]. Specimen geometry and FE model are presented in **Fig. 2**.

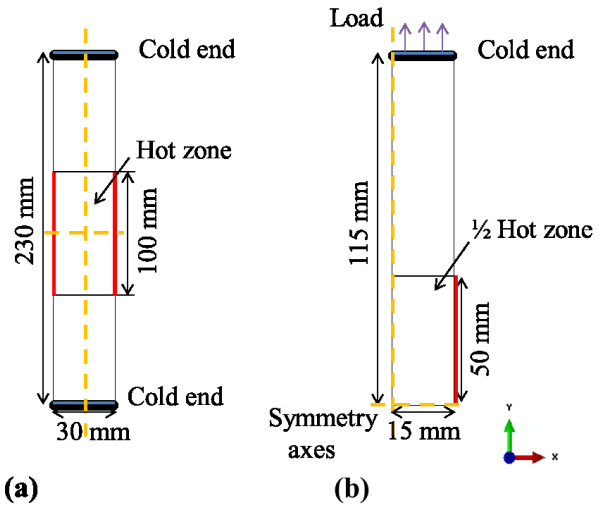

Figure 2: (a) Specimen dimensions and (b) axisymmetric finite element model.

The model showed an increase of temperature up to 1600 °C in the specimen heated zone, which remained constant until the end of the creep experiment. The difference of the temperature between the centre and the surface of the specimen caused emergence of thermal stresses. **Fig. 3** illustrates the axial stresses at the centre and on the surface of the specimen in the beginning of the preheating for the three different heating rates. The selected nodes, where the stresses were observed, are shown in **Fig. 4**.

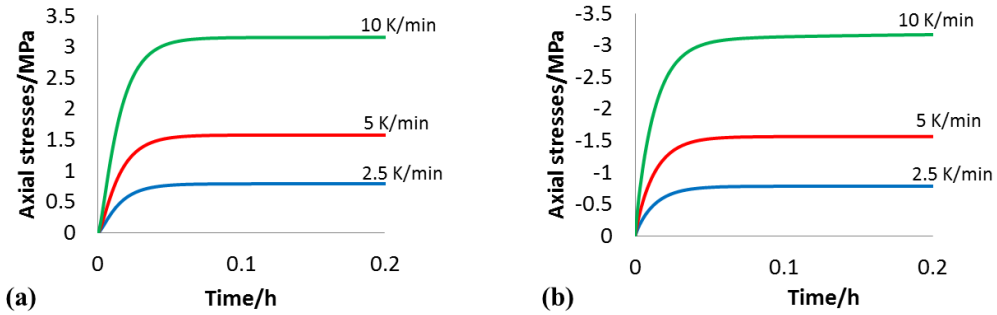

Figure 3: (a) Axial tensile stresses in the centre and (b) compressive stresses on the surface of the specimen for different heating rates.

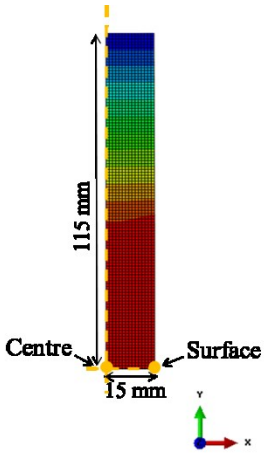

Figure 4: Nodes chosen for stresses observation.

During heating up the maximal temperature is found at the specimen surface, this leads to emergence of compressive stresses at the outer surfaces and tensile stresses at the centre of the heated specimen. After some time the stresses stabilize and keep relatively constant until the temperature within the specimen reaches 1600 °C. It is seen if **Fig. 3** that increasing the heating rate leads to the rise of the stress gradients. The maximum thermal stresses increased from 0.78 MPa at 2.5 K/min to 1.57 MPa at 5 K/min. By increasing the heating rate further from 5 K/min to 10 K/min resulted in the doubling of the thermal stresses, to 3.15 MPa. This means that the

heating rate can seriously affect the mechanical integrity of the specimen. A high rate of 10 K/min is expected to generate important stresses that immediately trigger micro-crack formation. By applying lower heating rates at, for example, 2.5 K/min and 5 K/min, considerably lower compressive and tensile residual stresses are obtained at the surface and at the centre. Radial stresses also present a smaller scatter for 5 K/min preheating at the selected nodes. The tensile radial stresses reach a value of approximately 0.8 MPa in the centre and the compressive ones a value of approximately -1.55 MPa at the surface.

In order to apply an efficient heating up schedule, the tensile creep experiments were decided to be carried out with a heating rate of 5 K/min; which is the same rate as the one applied for the RUL and CIC standard methods. A dwell time of one hour was added in order to ensure a homogeneous temperature and stress distribution. The temperature distribution of the specimen before applying the mechanical load is presented in **Fig. 5a)**. The colour scale from red and blue indicates higher and lower temperatures, respectively. As expected the maximum temperature of 1600 °C was found at the heated zone and the minimum temperature, equal to 139.3 °C was situated at the cold ends. The cold end temperature is considered as being appropriate and low enough to secure the specimens to the stainless steel adapters with the use of thermally resistant organic glue. Along the gauge length of the specimen a homogeneous temperature distribution is observed. The maxima of the principal stresses occur outside the heated zone**,** as shown in **Fig. 5b)**. The highest stresses were located at a vertical distance of 65.5 mm from the centre, which was a result of the presence of a thermal gradient at already a low value and far from the extensometers position. Moreover, low and homogeneously distributed stresses were observed at the area where the deformation is measured. It can also be noticed within the simulation that a high length/radius ratio of the specimen has benefits with regards to the stresses and the temperature difference.

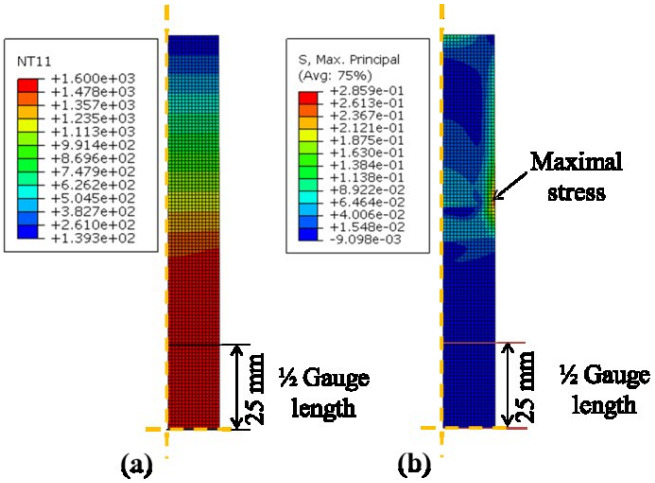

Figure 5: (a) Temperature and (b) stress distribution before application of tensile load (320 min preheating and 60 min dwell time).

The probable influence of thermal stresses during heating up was verified by carrying out FE simulations with two different models. The first model considered the creep when the temperature attained a value of 1600 °C. The second model took into account the creep during the heating-up period at temperatures above 1300 °C. The results of the two models, with and without considering creep during heat-up, were analysed and compared. Initially, and for setting up the testing machine design, the creep data were estimated for the simulation. After the measurements documented in **Table 2** were acquired, the preliminary calculations were repeated for verification. The following results illustrate the behaviour of the material using the creep data from **Table 2**.

The specimen was heated up to 1600 °C during approximately 5h20min and then kept at a constant temperature for one additional hour. **Fig. 6** illustrates the axial stresses on the surface of the specimen with and without allowing of the creep during preheating (**Fig. 6a)**) and the difference between the two simulated creep strains, $\Delta\varepsilon$ (**Fig. 6b)**). For the model that considers creep during preheating, tensile stresses in the centre and compressive stresses at the surface gradually decreased after 4h20min which corresponds to a temperature of 1300 °C. The model that does not allow for creep during preheating shows a harsh decrease of axial surface stresses at 1600 °C. Following one hour dwell time, the temperature gradient in the heated region is completely equalized and tensile and compressive stresses diminished to nearly zero. The creep strains, with and without considering the creep during preheating, indicated nearly no divergences.

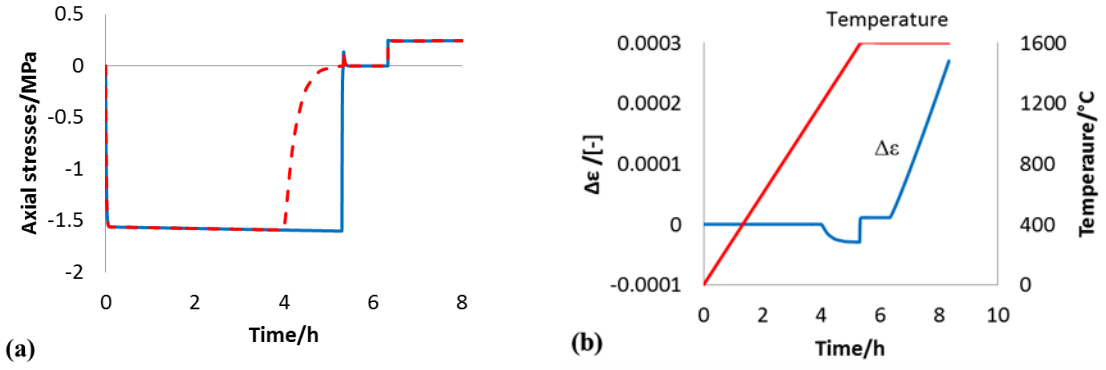

Figure 6: (a) Axial stresses on the surface with (dashed line) and without (solid line) considering the creep during preheating. (b) Temperature evolution and difference between the simulated creep strains at 5 K/min.

Fig. 6a) shows a minor jump in the axial stresses at 5h20min, as the thermal homogenization in the specimen when reaching the target temperature (1600 °C) was attained. At 4h20min, in **Fig. 6b)** a drop of Δε happens due to the creep deformation already at 1300 °C while considering the creep during preheating, leading to a slight increase of the irreversible strain. This deviation between the two simulated creep strains, Δε, augmented to a value of 0.0003 until the end of the simulation. However this value remained minor even after two hours of creep testing. Moreover, for an experiment performed at 1600 °C with an applied stress of 0.25 MPa (**Fig. 13b)**) the total creep strain at the end of the primary creep differed by only 0.01 % of the simulated value while considering the creep during preheating. From these outcomes, it can be noticed that the testing technique is not significantly influenced by low thermal strains during the heating up period. It is then concluded that the chosen heating up procedure does not influence the material creep.

2.2.3 Details of design and main features of the tensile creep machine

The tensile creep testing facility was developed and established in close collaboration with the company Messphysik [114]. The tensile creep testing machine is based on a single rotating spindle connected to a load cell that measures the applied force and sustained by a rigid frame. A maximum loading capacity of 20 kN which corresponds to approximately 28 MPa for the specimens cross sectional area is assured by the setup. The measurement can be performed either load or displacement controlled; the first option was chosen here. The loading device and the testing furnace are illustrated in a schematic diagram in **Fig. 7**. The compact high-temperature furnace, with heating elements made of molybdenum disilicide ($MoSi_2$), permits temperatures of up to 1700 °C. It is made of two symmetrical parts fixed in the vertical orientation and it covers the isothermal region of the specimen. During heating, the two sections are sealed together by means of clamps, which are easy to operate.

The electric furnace has openings at the rear and at the front for the extensometers and openings at the top and at the bottom for the specimen. It is perfectly centred and does not come into contact with the specimen or the extensometers. Displacements are recorded at high resolution (<0.1 μm) by two extensometers with a class-0.5 accuracy of measurement according to ISO 9513. They are diametrically arranged at the rear and at the front of the machine. Two corundum rods for each extensometer are in direct contact with the specimen surface. Relative movement between the two rods is restricted to a single degree of freedom (in a vertical direction). High initial gauge length of 50 mm was favoured to cover a large area of the specimen and thus take into consideration the heterogeneous material microstructure comprising the large grains. To verify the thermal homogeneity of the specimen within the gauge length, 3 thermocouples were placed at its surface during testing; one thermocouple placed in the centre and the two remaining ones were placed at the upper and the lower limits of the gauge length, respectively.

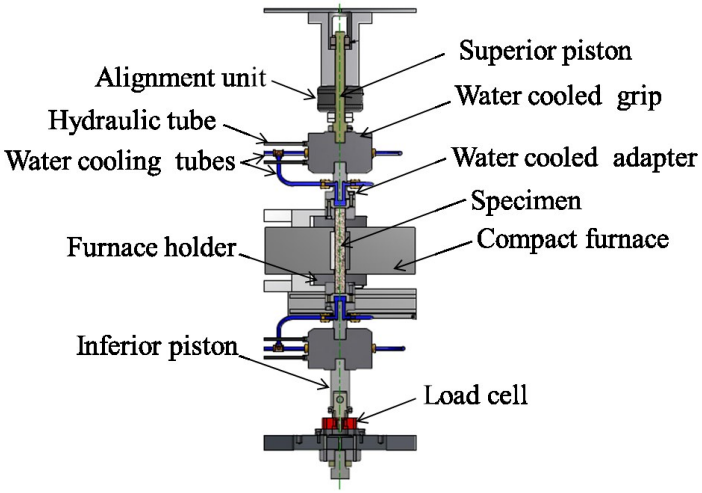

Figure 7: Schematic representation of the loading device and the testing furnace (courtesy of Messphysik [114]).

The specimen ends were decided to be glued to steel adapters outside the furnace because of the absence of feasible solutions to fix the specimens at high temperatures. The furnace is of cylindrical shape with a height of 102 mm and a diameter of 140 mm. The specimen, having dimensions of 230 mm height by 30 mm diameter, is large enough to allow for a homogeneous distribution of the loads, induced at the fixtures, in the volume defined by the gauge length. The distance between the specimen centre and the cold ends is appropriate for ensuring homogeneous temperature distributions and low thermal stresses in the specimen along the gauge length. The creep experiments were performed at ambient air and atmospheric pressure. Two Platinel II thermocouples of type B according to [115] placed inside the furnace and located in the centre in a close distance to the specimen's gauge length, constantly monitor the temperature.

The lower and upper adapters are glued to the specimen and are both safely connected to water cooling tubes in order to reduce their temperature during testing. They are also gripped by a hydraulic system providing a pressure of 100 bars, which is also water cooled. **Fig. 7** exhibits a detailed schematic of the electrical furnace and the device with all its features. An alignment unit is integrated in the upper part of the machine to avoid uneven loading and to ensure the alignment adjustment of the superior piston with the inferior one along the vertical axis. The unit comprises a connecting flange with centring and connecting bolts for the adjustment of eccentric and angular misalignments of the loading axis. The uniformity of the stress field in the specimen was assured by room-temperature measurements using the strain gauges method. The alignment procedure of the machine was certified according to ASTM E 1012 [116].

Figure 8: Tensile creep testing equipment; specimen, opened furnace and front extensometer.

2.2.4 Specimen preparation and testing

The investigated materials were fired magnesia chromite and magnesia spinel bricks particularly suitable for high temperature applications in the steel industry. The first one was designed with a high resistance to thermal shock and erosion. Its composition consisted of 56.5 wt% MgO, 25.5 wt% Cr_2O_3, 6.0 wt% Al_2O_3, 10 wt% Fe_2O_3, 1.3 wt% SiO_2 and 0.6 wt% CaO. The second one was designed to sustain high thermomechanical, thermal and chemical loads, especially for the application in cement rotary kilns. It had the following composition: 86.53 wt% MgO, 11.22 wt% Al_2O_3, 0.34 wt% Fe_2O_3, 0.58 wt% SiO_2 and 1.09 wt% CaO. Their microstructure is shown in **Fig. 9**.

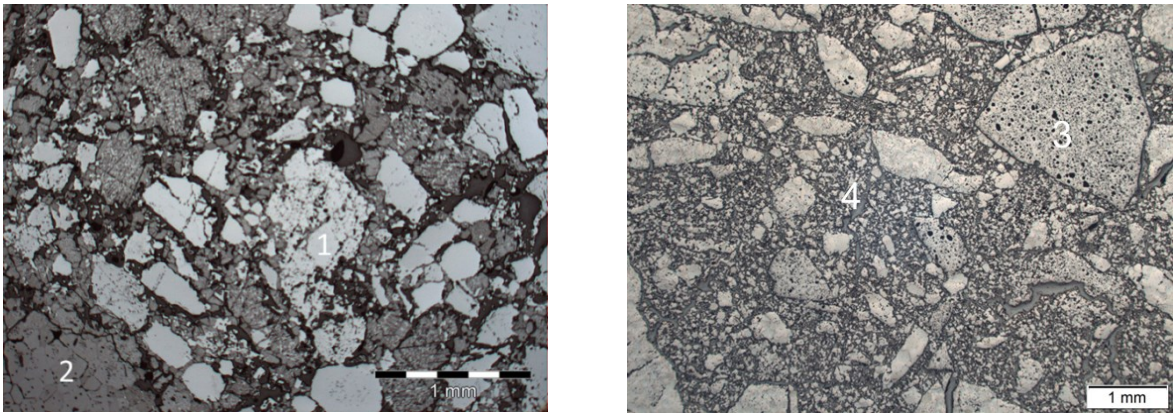

Figure 9: Reflected light microscopic image of the investigated materials. a) magnesia-chromite: 1. chromite, 2. magnesia-chromite coclinker; and b) magnesia spinel: 3. spinel, 4. magnesia.

The cylindrical specimens, having dimensions of 230 mm length and 30 mm diameter, were core drilled and cut from commercially available bricks. The specimens were aligned and glued to the adapters using a fixing device. **Fig. 10** shows the alignment and gluing of a magnesia-chromite specimen with the steel adapters on the fixing device. This device comprises a controlled level platform located between two symmetrical adapter holders. Water-cooled adapters were fixed parallel to each other on both sides of the device. The sample was then positioned on the platform that kept it perfectly straight and its ends were inserted into the adapters. Through adjustment of the platform level it was possible to ensure an accurate alignment of the sample and the adapters. The specimen ends were then glued to the steel adapters. The high temperature resistant adhesive contains two components, a resin and a hardener in a ratio of 2:1. A 50 ml cartridge manual applicator with a mixing nozzle was used to inject the adhesive through the orifices of the water-cooled adapters. The two components of the epoxy were mixed inside the mixing nozzle. The cartridge was used multiple times and the mixing nozzles were of single use. The hardening of the adhesive lasted approximately eight hours at room temperature.

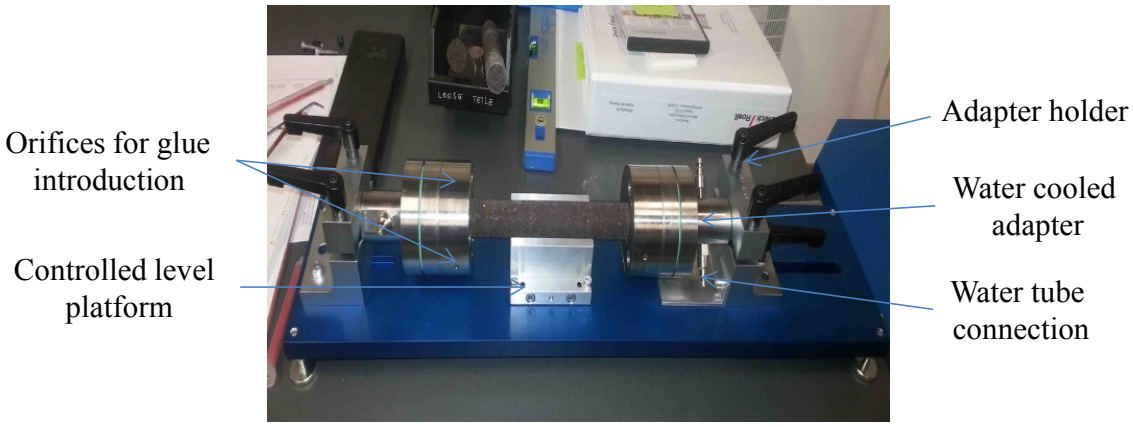

Figure 10: Fixing device.

Once the adhesive hardened, the specimen and the adapters were introduced into the testing machine in a vertical position. The lower adapter was first gripped, then the lower piston was moved upwards until the upper adapter coincided with the superior grip. At this state of the procedure, the force of the loading cell needs to be set to zero in order to take into account the weight of the specimen. The upper adapter was then gripped. If the upper adapter deviates from the vertical axis when it coincides with the superior grip, the force will rise quickly before activation of the hydraulic grip due to contact. This provides an indication and confirmation of the specimen alignment. Both parts of the furnace could be then joined together and fastened. The rear and front extensometers are lastly introduced into the machine just before starting the experiment.

At the end of each creep measurement, the broken specimens together with the adapters were released and removed from the tensile creep machine. As the specimen ends are still glued to the adapters it is necessary to burn out the adhesive and clean the adapters for a multiple use. Therefore, to burn the adhesive, the adapters were placed in an electrically heated furnace set at 400 °C during 2 hours. They were then cooled to ambient temperature for a period of 2 to 3 hours and cleaned by scraping off the glue deposits.

2.3 Conclusion

High temperature measurements of heterogeneous refractories were performed using an innovative tensile creep testing setup. The machine had a new design that improved the specimen alignment and fixture. An even distribution of stresses permitted to avoid bending during testing. Thermo-mechanical simulations were carried out preliminary to the measurements with the purpose of optimizing the tensile creep procedure. The choice of specimen geometry and heating rate were adequate for optimized experimental conditions. Observations of temperature and stress distribution in the hot zone and at the cold ends confirmed the viability of the experiments. The design and dimensions of the testing device and the specimen provided reliable results. The testing procedure was not significantly influenced by low thermal strains during the heating up period.

Chapter 3: Testing results and evaluation procedures

3.1 Introduction

After having implemented the tensile creep machine, measurements were performed with two refractory ceramics containing spinel, magnesia chromite and magnesia alumina spinel materials. Magnesia chromite material is consistently employed in applications necessitating high hot-strength and resistance against attack by slags and liquid metals [117, 118]. Magnesia alumina spinel materials have largely replaced the application of magnesia chromite refractories in cement rotary kilns as they offer a chrome free eco-friendly alternative. They combine favourable properties with respect to their thermomechanical behaviour and their thermal and chemical resistivity.
After creep testing an evaluation of the experimental results was needed. In this chapter, the creep behaviour for these two refractory materials is described together with an efficient approach developed to analyse the creep data. A constitutive creep equation is applied to fit the measurements and its parameters are inversely estimated using two different approaches. An investigation is continued for magnesia-chromite material, which consists of finding the relation between the creep strain, the applied stress and the temperature. These correlations give evidence about the beginning of the creep stages. An implementation in a thermomechanical simulation program will permit to apply the corresponding creep parameters and therefore predict the behaviour of industrial vessels.

3.2 Experimental results and discussion

For the period of the preheating, a tensile preload of 0.01 MPa and a heating rate of 5 K/min were applied. The low preload value was chosen in order to stabilize the specimen during preheating without causing undesirable irreversible strain. The target temperature was maintained constant for one hour to ensure steady-state thermal conditions inside the sample. The extensometers were attached before the application of the testing load. The rear and front extensometers showed good agreement for all tests approving the accurate specimen alignment at high temperature. **Fig.11** illustrates the extensometers recording of one experiment with magnesia-chromite specimen at 1400 °C and 0.5 MPa having a standard deviation equal to 0.012.

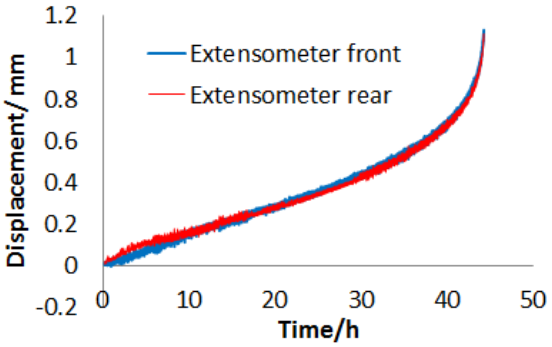

Figure 11: Displacement according to both extensometer readings dependent on time at 1400 °C and 0.5 MPa for the magnesia-chromite specimen.

3.2.1 Magnesia-chromite material

Tensile creep experiments of magnesia-chromite specimens were performed for several loads at 1300 °C, 1400 °C, 1500 °C and 1600 °C. The results of the experimental total strains are plotted in **Figs. 12** and **13**.

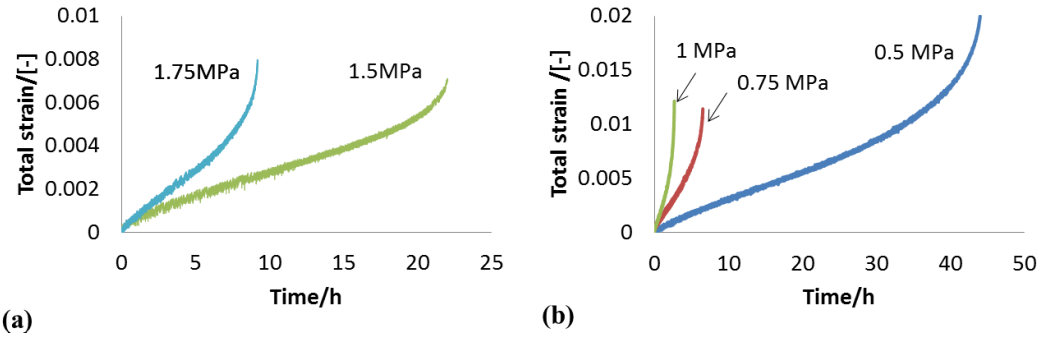

Figure 12: Measured total strains over time at (a) 1300 °C and (b) 1400 °C for the magnesia-chromite material.

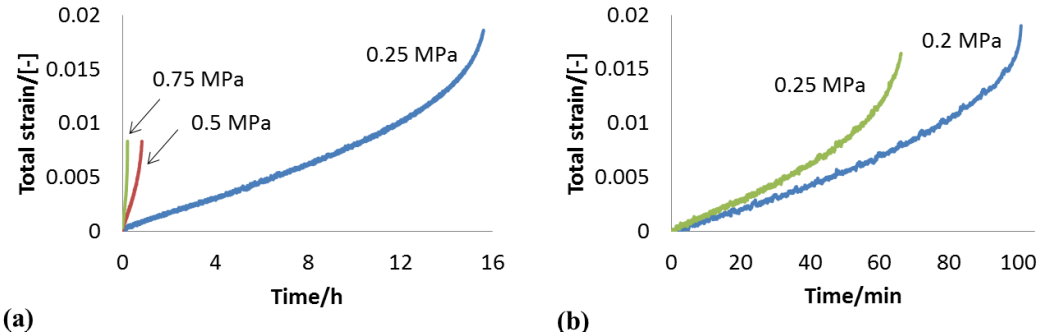

Figure 13: Measured total strains over time at (a) 1500 °C and (b) 1600 °C for the magnesia-chromite material.

Three creep stages (strain-hardening, steady-state, and strain-softening) were revealed for all measurements at temperatures from 1300 °C to 1600 °C for loads between 0.2 MPa and 1.75 MPa. All measurements ended with rupture of the specimens between the extensometer rods.
The ultimate strains of all tests varied between 0.008 and 0.02. **Fig. 12a)** represents the experimental total strain at 1300 °C under loads of 1.5 MPa and 1.75 MPa. The experiment lasted for more than 20 hours for a 1.5 MPa load and about 10 hours for a 1.75 MPa load. The elapsed time until failure at this temperature was approximately halved while increasing the stress by only 0.25 MPa. The tertiary creep stage required the longest duration for each test. The maximal total strains reached were approximately 0.08 before failure. As seen in **Fig. 12b)**, at 1400 °C and 0.5 MPa the test lasted 44 hours with 13 hours of tertiary creep. By increasing the loads the creep test was shortened to 6 hours at 0.75 MPa and to less than 3 hours at 1 MPa. At 1500 °C and 0.25 MPa (**Fig. 13a)**) the creep lasted for 15 hours with the tertiary creep representing the longest phase (10 hours). At higher loads the creep time dropped significantly to 50 min for a 0.5 MPa load and less than 15 min for a 0.75 MPa load. The load of 0.5 MPa was applied for two temperatures (1400 °C and 1500 °C). The creep time was significantly reduced from 40 hours at 1400 °C to only 50 min at 1500 °C. Creep was more apparent at 1600 °C for the low applied stresses of 0.2 and 0.25 MPa (see **Fig. 13b)**). At these conditions creep proceeded rapidly for both tests, lasting almost two hours at 0.2 MPa and more than one hour at 0.25 MPa. For the same load (0.25 MPa) and at an increased temperature of 1600 °C, the creep time was also significantly reduced from 15 h to only 1 h 40 min.

3.2.2 Magnesia-spinel material

Tensile creep experiments of magnesia-spinel specimens were also performed for several loads at temperatures of 1150 °C, 1200 °C, 1250 °C, 1300 °C and 1400 °C. The results of the experimental total strains are plotted in **Figs. 14** and **15**.

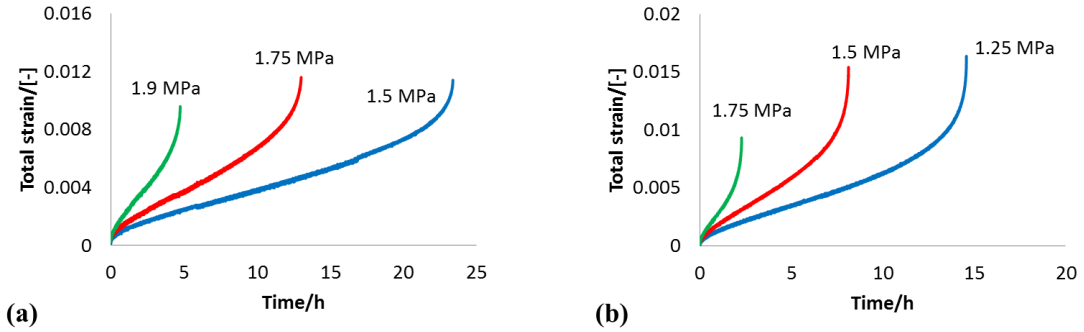

Figure 14: Measured total strains over time at (a) 1150 °C and (b) 1200 °C for the magnesia-spinel material.

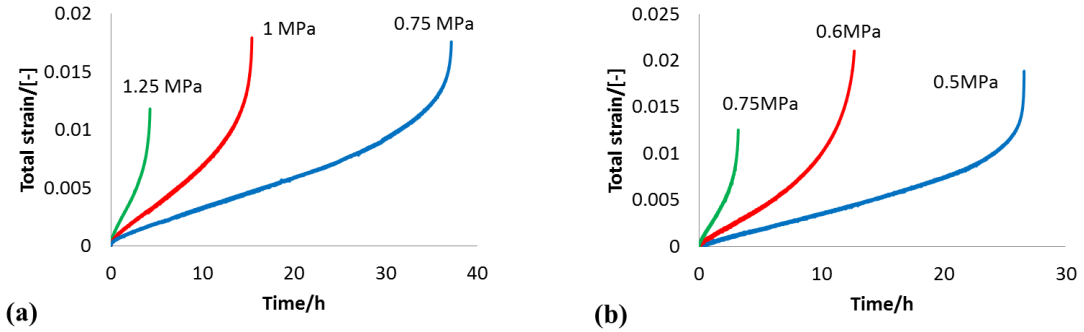

Figure 15: Measured total strains over time at (a) 1250 °C and (b) 1300 °C for the magnesia-spinel material.

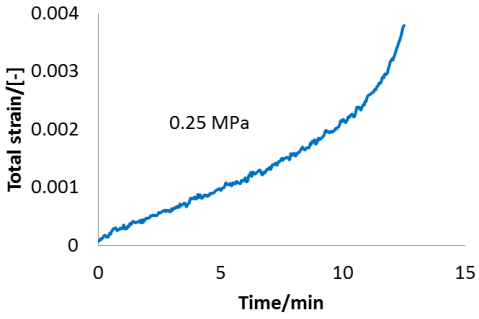

Figure 16: Measured total strains over time at 1400 °C for the magnesia-spinel material.

As for magnesia-chromite the strain-hardening, steady-state and strain-softening behaviours were detected for all measurements at temperatures from 1150 °C to 1400 °C with applied stresses between 0.25 MPa and 1.9 MPa. Also for magnesia-spinel specimens measurements ended with their rupture between the extensometer rods.

Ultimate strains of all measurements differed from 0.004 to 0.021. **Fig. 14a)** illustrates the experimental total strains at 1150 °C under loads between 1.5 MPa and 1.9 MPa. Compared to higher temperatures, failure occurred at lower total strain for a high applied mechanical load. At this temperature the experiments lasted for more than 23 hours under a 1.5 MPa load, about 13 hours under a 1.75 MPa load and almost 5 hours under a 1.9 MPa load. Here also the creep time until failure at 1150 °C approximately doubled with decreasing the applied stress by only 0.25 MPa. The maximal total strains did not vary much from an experiment to another at this temperature; their values attained around 0.01 before failure. At 1200 °C and 1.25 MPa (**Fig. 14b)** the creep lasted almost 15 hours with the tertiary creep representing one third of the overall creep time. At higher loads the duration of the creep test dropped to a bit more than 8 hours for a 1.5 MPa load and more than 20 min for a 1.75 MPa load. The total ultimate strain of the highest applied load (1.75 MPa) at this temperature considerably decreased from about 0.015 at 1.5 MPa to 0.0093. The loads of 1.5 MPa and 1.75 MPa were applied for two temperatures (1150 °C and 1200 °C). The creep time harshly reduced from 23 hours at 1150 °C to only 8 hours at 1200 °C with an applied stress of 1.5 MPa, and from 13 hours at 1150 °C to 2 hours at 1200 °C with an applied stress of 1.75 MPa. As seen in **Fig. 15a)**, at 1250 °C and 0.75 MPa the test lasted 37 hours with about 15 hours of tertiary creep. By increasing the loads the creep test was reduced to 15 hours at 1 MPa and to more than 4 hours at 1.25 MPa.

Creep was more significant at higher temperatures (1300 °C and 1400 °C) under lower applied stresses between 0.25 MPa and 0.75 MPa (see **Figs. 15b)** and **16**). Indeed, creep proceeded extremely rapidly for the highest temperature, lasting less than 15 minutes at 0.25 MPa. At 1300 °C the same observations were made as for 1250 °C and 1200 °C; the ultimate strain at 0.75 MPa is much lower than those at 0.6 MPa and 0.5 MPa. Failure occurred earlier at higher applied load. Equivalent loads (0.75 MPa) were applied at 1250 °C and 1300 °C. Increasing the temperature by only 50 °C led to a decline of the elapsed creep time by almost 34 hours, which is extreme.

3.3 Norton-Bailey creep law

Numerous investigations defined the tensile creep behaviour of a material by means of Norton-Bailey creep law [44, 77, 70 and 119], mostly to describe the compressive creep when it comes to refractory ceramics. The parameters of Norton-Bailey power law were assessed from the experimental tensile creep results. The total strain, which is equal to the summation of the creep strain and the elastic strain (**Eq. 29**), was acquired from the extensometers displacement with an initial gauge length of 50 mm.

$$\varepsilon_{total} = f(t) \tag{28}$$

$$\varepsilon_{total} = \varepsilon_{cr} + \varepsilon_{elastic} \tag{29}$$

The resulting total strain, ε_{total} responding to an applied stress is represented as a summation of the elastic and non-elastic strain. The creep strain, ε_{cr}, is then obtained by the subtraction of the elastic strain σ/E from the total elongation ε_{total} (**Eq. 30**).

$$\varepsilon_{cr} = \varepsilon_{total} - \frac{\sigma}{E} \tag{30}$$

Where σ is the applied stress and E is Young's modulus of the material determined by impulse excitation technique (IET) [120].

As mentioned previously, principally two formulations are possible for the determination of creep; the time hardening formula where the creep rate is function of time and the strain hardening formula where it is rather function of strain. Experimental results on metal based materials have shown a better agreement with the strain hardening law [121]. For a constant applied stress, both laws showed the same results. However, for relatively long creep time, if the stress varies significantly, a smaller creep rate is resulted with the time hardening formula. In contrary, strain hardening formula ignores the time. Time hardening law can be utilized only when small stress variations are to be expected [121]. Norton-Bailey strain rate constitutive equation utilized for the analysis of the creep data is a function of creep strain, stress and temperature:

$$\frac{\partial \varepsilon_{cr}}{\partial t} = K(T)\sigma^{n}\varepsilon_{cr}^{a} \tag{31}$$

K(T) is temperature dependent function [$MPa^{-n}s^{-1}$], *n* and *a* are the stress and the strain exponents. Those tensile creep parameters were to be determined by regression analysis at each of the three creep stages.

3.4 Creep evaluation procedure

After having obtained the experimental creep curves comprising three stages, an accurate and rapid evaluation method to define the creep parameters was required. The first step was the determination of the transition points, i.e. the time and the corresponding experimental total strain between the stages. Creep parameters were then evaluated for the primary, secondary and tertiary stage in dependence on the transition points.

The creep deformation can be measured during the increase of the load and at constant stress. For the investigations presented here, only material creep under constant load was evaluated, *viz.* the ascending part of the load-time curve was neglected. **Eqs. 30** and **31** can then be easily solved

with a rearrangement of the variables ε_{cr} and t followed by integration with respect to creep strain and time, respectively, to yield the following equation for the creep strain:

$$\varepsilon_{total}(t_i) = \frac{\sigma}{E} + \left[\left\{ \varepsilon_{total}(t_{j,i}) - \frac{\sigma}{E} \right\}^{(1-a_j)} + (1-a_j) K_j(T) \sigma^{n_j} (t_i - t_{j,i}) \right]^{\frac{1}{1-a_j}} \quad (32)$$

Here t_i denotes the ith time step used for evaluation, j denotes the creep stages, j=1, 2, 3. t is the elapsed time and $t_{s,j}$ the staring time of that stage j to which t_i belongs:

$$t_{s,j} = \max_{k=1,2,3} (t_{s,k}) \Big| t_{s,k} \le t_i$$

All parameters (K_j, a_j, n_j and $t_{s,j}$) were determined through several measurements using an inverse evaluation procedure. The value of $t_{s,1}$ was determined from the moment when the constant stress was achieved. The starting values for $t_{s,2}$ and $t_{s,3}$ were determined by using a polynomial curve fit of the experimental total strain data. The derivative was then calculated and the starting values determined from its roots. With these starting values for each measurement, and with suitable estimations for n_j, a_j and K_j, all creep parameters were then determined from an inverse estimation procedure using two different approaches. The first one applied the non-linear Generalized Reduced Gradient (GRG) algorithm [122], whereas the second one utilized the Levenberg-Marquardt (L-M) algorithm [123]. These two procedures iteratively minimize the sum of squared differences between the measured and the calculated total strain values for each experiment performed. The L-M optimization technique, exploited in the software Matlab, can be more efficient with respect to accuracy and gain of time. The implemented approach for detecting Norton-Bailey creep parameters by inverse estimation is schematized below:

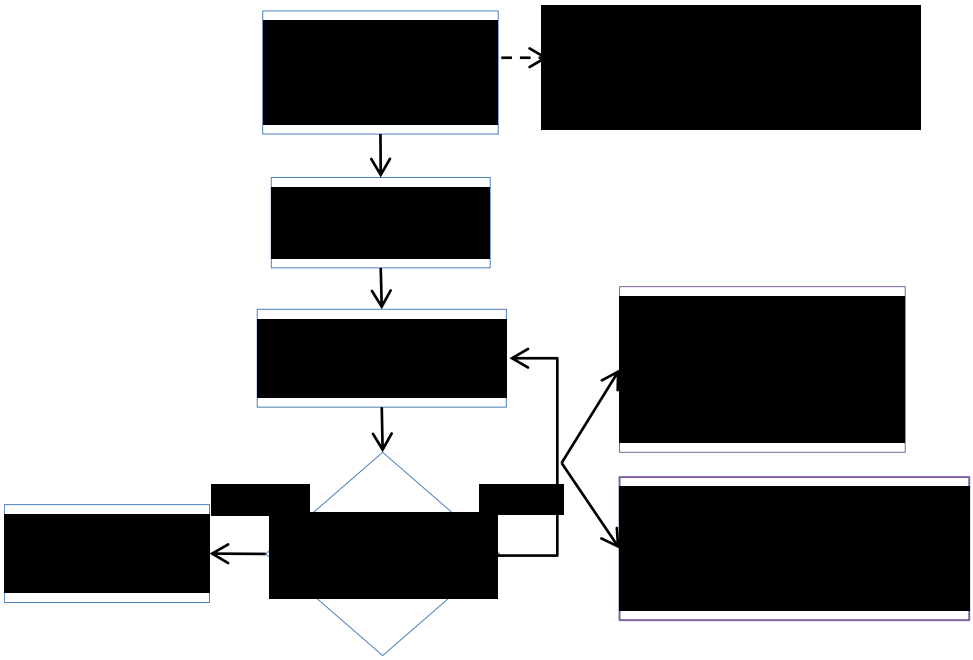

Figure 17: Approach to define the Norton-Bailey creep parameters.

The inverse estimation principle is the minimization of an objective function while refining the parameter vector. The objective function $h(x)$ can be defined by:

$$h(x) = \frac{1}{2} Y(x)^{\mathrm{T}} Y(x) \tag{33}$$

$$h(x) = \frac{1}{2} \sum_{i=1}^{p} y_i(x)^2 \tag{34}$$

$$Y(x) = \left(y_1(x), \ldots, y_p(x)\right)^T \tag{35}$$

$$x = \left(x_1, \ldots, x_n\right) \tag{36}$$

Here x is the parameter vector, n the number of parameters, $Y(x)$ the residual vector and p the number of time steps.

3.4.1 Evaluation approach using the GRG algorithm

The Generalized Reduced Gradient Method (GRG) is a generalization of the reduced gradient method. It is an approximation by allowing also nonlinear constraints and arbitrary auxiliary conditions for the variables. The algorithm minimizes the objective function that is subjected to

the constraints. The reduced gradient (RG) algorithm is defined as an iterative first-order optimization algorithm for constrained convex optimization. The algorithm considers a linear approximation of the objective function for the iteration, and moves slightly towards a minimizer of this linear function, which is taken over the same domain. The fundamental idea of GRG method is comparable to how the Simplex method of linear programming operates [124].
The approach that uses the GRG algorithm was developed as follows: a fifth order polynomial curve to fit the experimental total strain was plotted. The first derivative of this polynomial function, which represents the total strain rate, was then calculated and plotted with respect to time. The selection of the transition points corresponded to the two minima of the strain rate curve. See the following figure **(Fig.18)**.

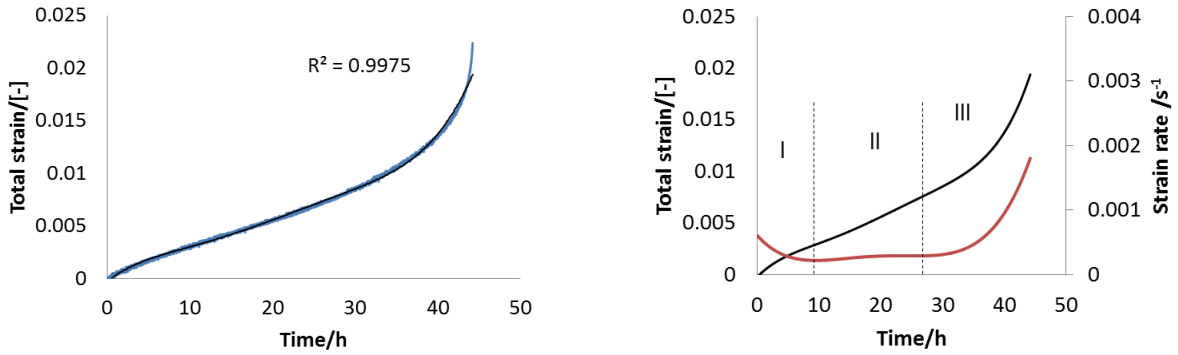

Figure 18: Total strain (blue), polynomial regression model (black) and its first derivative (red) with respect to time – creep of burnt magnesia-chromite material at 1400 °C and 0.5 MPa.

At each temperature at least three creep experiments with three different applied mechanical loads were necessary to determine the Norton-Bailey parameters. These creep parameters n_j, a_j *and* K_j at each of the three stages and the transition times $ts,_2$ and $ts,_3$ were progressively inversely estimated. The figure below (**Fig. 19**) illustrates the procedure for one experiment.

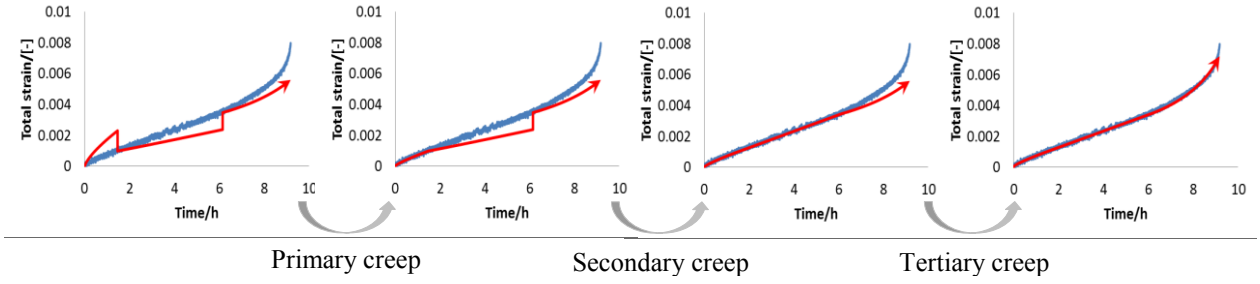

Figure 19: Inverse estimation of the creep parameters using the GRG algorithm – creep of magnesia-chromite material at 1300 °C and 1.75 MPa.

A reference function was integrated in order to instantaneously find and incorporate in the Norton-Bailey creep strain law the transition total strains $\varepsilon_{total}(t_{s,2})$ and $\varepsilon_{total}(t_{s,3})$ corresponding to the transition times, $ts_{,2}$ and $ts_{,3}$.

3.4.2 Evaluation approach using the L-M algorithm

The L-M algorithm provides a numerical solution to the minimization problem of a function, often non-linear and dependent on several variables. The algorithm interpolates the Gauss-Newton algorithm and the gradient algorithm. More stable than Gauss-Newton, L-M algorithm finds a solution even if it starts far from a minimum. However, for some very regular functions, it may converge somewhat less rapidly. The algorithm was established by Kenneth Levenberg [125] and published by Donald Marquardt [123].

The L-M algorithm was employed in the software Matlab, where a code was developed and improved in order to gain in efficiency and time for the inverse identification of Norton-Bailey creep parameters. It consisted of first determining the fifth order polynomial curve to fit the experimental total strain graphs. The third derivative of this polynomial function, representing a second order polynomial (convex curve), was calculated and their roots were determined. The selection of the transition times $ts_{,2}$ and $ts_{,3}$ corresponded in this case to the minimum and the maximum values of the roots, respectively. See **Fig. 20**.

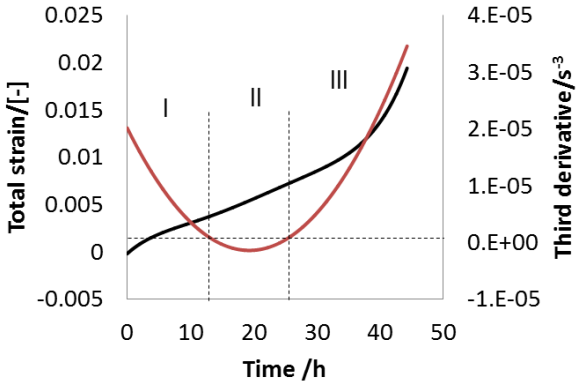

Figure 20: Polynomial regression model (black) and its third derivative (red) – creep of burnt magnesia-chromite material at 1400 °C and 0.5 MPa.

Different transition points were selected by this method. This alternative allowed of a rapid separation between the three creep stages and a simultaneous application of the L-M algorithm to inversely identify the creep parameters at each of the three stages.

Nevertheless, a third alternative can be proposed and applied in the software Matlab; which was the determination of the second derivative of the fifth order polynomial function equivalent to the creep acceleration. Also here the minimum and the maximum values of its roots could represent the transition times $ts,_2$ and $ts,_3$, respectively. The three alternatives are sketched in **Fig. 21**.

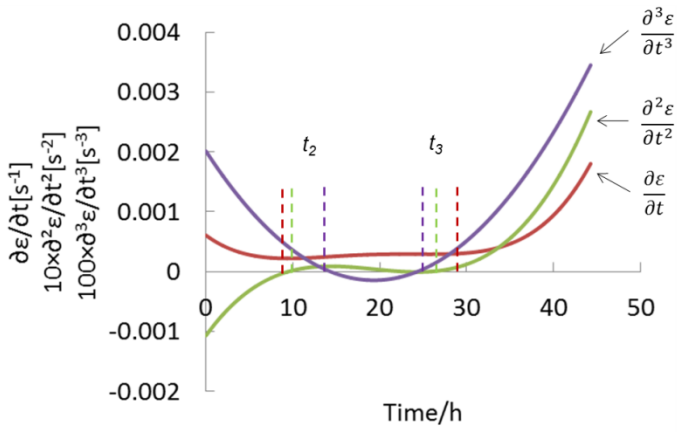

Figure 21: First, second and third derivatives of the polynomial function illustrating the transition points $ts,_2$ and $ts,_3$ from the first (red), second (purple) and third (green) alternatives – creep of magnesia-chromite material at 1400 °C and 0.5 MPa.

The code written in Matlab program enables not only the application of L-M inverse estimation method, it also provides a clever and rapid way to obtain satisfactory results (See Appendix A). With the creation of a function that extracts the measurement files the user is able to apply the procedure to one, two, three or n experiments. The measurement files should be written in the following manner:

measure_temperature_applied load (units)_applied load (tenths).data.

This means for an experiment performed at 1400 °C under a load equal to 0.5 MPa the test file should be written:

measure_1400_0_5.data

The data of the test file should provide the creep time in seconds, the applied mechanical load in Newton and the average displacement in millimetres. This is how the data are actually extracted after the tensile creep measurements.

The program applies an approximation function, derives the function and defines its roots for every measurement file that is added. The minimum and the maximum of the roots are then considered as the beginning points of the secondary and the tertiary stages, respectively.

The data are afterwards separated and rearranged according to each stage in order to perform the inverse evaluation. Norton-Bailey creep law is then applied with the consideration of the transition points.

All testing curves were resized to the same number of data points. The longest tests would have had a higher influence on the optimization.

The evaluation program considers also the elastic behaviour (Young's modulus) of the material with respect to temperature. It is possible to allocate the elastic modulus value to each measurement file and therefore obtain common results for different temperatures.

3.4.3 Norton-Bailey creep parameters

a. Magnesia-chromite material

Creep parameters of the Norton-Bailey constitutive equation (n_i, a_i and K_i) are summarized in **Table 1**. The parameters at 1300 °C and 1600 °C were determined with GRG algorithm by fitting two curves and those at 1400 °C and 1500 °C by fitting three.

Table 1: Creep parameters n_i, a_i and K_i [$MPa^{-n}s^{-1}$] for magnesia-chromite bricks at 1300-1600 °C (GRG algorithm).

Stage	I			II		III		
T(°C)	K_1	a_1	n_1	K_2	n_2	K_3	a_3	n_3
1300	3.05E-09	-0.34	2.45	9.13E-09	5.31	2.36E-06	1.14	7.48
1400	1.87E-07	-0.18	2.81	7.17E-07	3.18	3.08E-04	1.01	4.18
1500	1.05E-06	-0.38	3.01	1.58E-05	3.05	1.07E-02	0.99	3.99
1600	6.16E-06	-0.08	1.45	1.66E-05	1.69	1.50E-02	1.15	1.75

It is noticed in **Table 1** that K increases with the increasing temperature. For each isotherm, K also rises as the creep stage develops, with a higher increase from the secondary to the tertiary stage by three orders of magnitude.

The stress exponent n rises considerably with the creep stage progression at 1300 °C. At 1400 °C and 1500 °C n is approximately 3 for the primary and the secondary stages, and equal to 4 in the tertiary stage. At 1600 °C the stress exponent n slightly increases with creep stage progression, showing values between 1.45 and 1.75.
For the primary creep stage at 1300 °C, 1400 °C and 1500 °C the parameters a and n are similar. These values are reduced at 1600 °C to –0.08 and 1.45, respectively. In the secondary creep stage n decreases from 5.31 at 1300 °C to approximately 3.1 at 1400 °C and 1500 °C. At 1600 °C, the stress exponent n drops to 1.69, equivalent to the values in the primary stage. Similar observations are made for the tertiary creep stage, but with higher values of n compared to those of the secondary stage. Indeed, n is equal to 7.48 at 1300 °C, reduced to approximately 4 at 1400 °C and 1500 °C, and then further reduced to 1.75 at 1600 °C. In the tertiary creep stage a is approximately equal to 1 for all isotherms, demonstrating significant acceleration at the last creep stage that eventually led to fracture.

The creep parameters of the Norton-Bailey constitutive equation (n_i, a_i and K_i) resolved with L-M algorithm are presented in **Table 2**. The parameters at 1300 °C and 1600 °C were also determined by fitting two curves and those at 1400 °C and 1500 °C by fitting three.

Table 2: Creep parameters n_i, a_i and K_i [$MPa^{-n}s^{-1}$] for magnesia-chromite bricks at 1300-1600 °C (L-M algorithm).

Stage	I			II		III		
T(°C)	K_1	a_1	n_1	K_2	n_2	K_3	a_3	n_3
1300	1.34E-09	-0.38	3.63	6.19E-09	5.42	4.82E-05	1.68	7.26
1400	2.31E-07	-0.15	2.82	7.60E-07	3.29	4.45E-04	1.08	4.33
1500	3.91E-06	-0.22	3.13	1.91E-05	3.19	2.30E-03	0.74	3.75
1600	8.74E-06	-0.04	1.43	5.67E-06	0.85	6.28E-02	1.36	1.99

Norton-Bailey creep parameters that were inversely-estimated with the L-M algorithm showed similar results comparing to the ones determined with the GRG algorithm. Some differences can

be noticed, especially for the temperature dependent function K within the tertiary creep and for the temperatures where only two curves were fitted, viz. 1300 °C and 1600 °C. The minor dissimilarities can be due to the different method utilized for the selection of the transition points.

b. Magnesia-spinel material

Table 3 summarizes the Norton-Bailey creep parameters (n_i, a_i and K_i) resolved with GRG algorithm. The parameters at temperatures between 1150 °C and 1300 °C were solved by fitting three curves at each of the temperatures.

Table 3: Creep parameters n_i, a_i and K_i [$MPa^{-n}s^{-1}$] for magnesia-spinel bricks at 1150-1300 °C (GRG algorithm).

Stage	I			II		III		
T(°C)	K_1	a_1	n_1	K_2	n_2	K_3	a_3	n_3
1150	5.27E-11	-0.81	5.81	1.28E-08	4.56	2.19E-07	0.49	4.66
1200	7.78E-10	-0.71	3.56	6.11E-08	3.82	1.34E-06	0.47	3.50
1250	1.17E-09	-0.74	3.02	1.68E-07	2.88	4.56E-04	1.39	3.29
1300	8.18E-07	-0.21	5.33	2.12E-06	4.50	4.48E-03	1.41	4.81

The temperature dependent function $K(T)$ increases with the increasing stage and increasing temperature. The fit for this material at 1150 °C and 1200 °C was not as precise as at higher temperatures, see **Fig. 22**. The evaluation was achieved with the GRG method. The heterogeneity of the material makes it difficult to obtain perfectly matching experimental and theoretical curves; specifically within the tertiary stage where damage mechanisms could have also taken part.

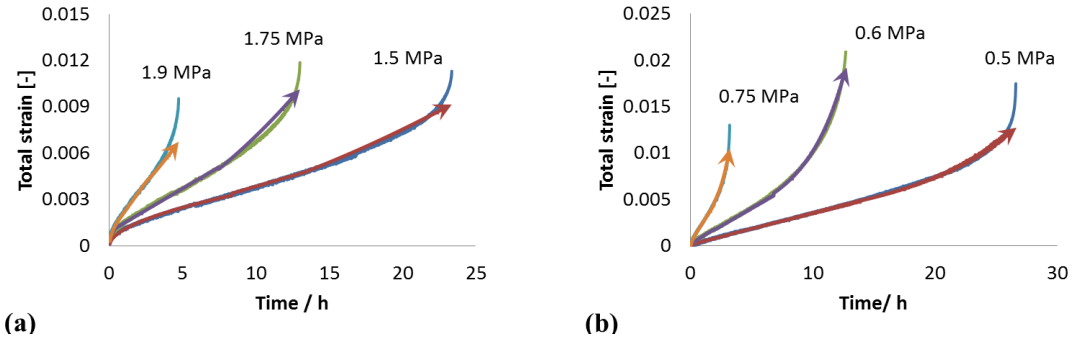

Figure 22: Measured (–) and inverse-estimated (→) total strains over time of magnesia-spinel bricks at (a) 1150 °C and (b) 1300 °C – GRG method.

The stress exponent *n* is considerably high at 1150 °C for the primary stage, 5.81, and then it decreases at 1200 °C and 1250 °C for the same stage to 3.56 and 3.02, respectively. At 1300 °C it rises again to approximately the same value as for 1150 °C. At temperatures of 1200 °C and 1250 °C, the stress exponent is equal to approximately 3 for all stages. For the two other temperatures, 1150 °C and 1300 °C, exponent *n* is higher. At these temperatures it attains values between 4.5 and 5.81 also for all of the three stages.

The strain exponent *a* increases in the primary stage from -0.81 at 1150 °C up to -0.21 at 1300 °C. At 1200 °C and 1250 °C for the primary stage the strain exponents are comparable. In the tertiary creep stage the exponents *a* are not so close to 1 for all isotherms as for the magnesia-chromite material. At lower temperatures *a* is equal to about 0.48, the value increases to 1.39 and 1.41 at 1250 °C and 1300 °C, respectively. The changes in the strain exponent may indicate a change in the creep behaviour at those temperatures. In some distance from crack faces other further cracks, which did not cause total failure, occurred (crack branching). See **Fig. 23**. This was not observed in the magnesia-chromite material. Furthermore, the cracks were propagating between matrix/grains interphase and not in an intragranular way. These may have significantly influenced the resulting parameters in the tertiary stage.

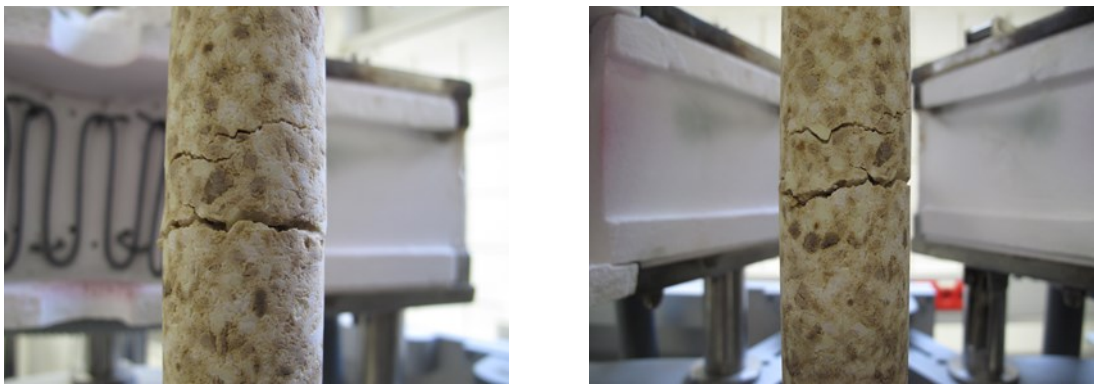

Figure 23: Magnesia-spinel specimen after creep testing at 1300 °C and 0.75 MPa.

Table 4 shows the Norton-Bailey creep parameters (n_i, a_i and K_i). The parameters were obtained with L-M algorithm by fitting three curves at each temperature..

Table 4: Creep parameters n_i, a_i and K_i [$MPa^{-n}s^{-1}$] for magnesia-spinel bricks at 1150-1300 °C (L-M algorithm).

Stage		I			II			III
T(°C)	K_1	a_1	n_1	K_2	n_2	K_3	a_3	n_3
1150	4.60E-11	-0.85	5.29	1.28E-08	4.56	5.03E-08	0.25	5.20
1200	1.23E-09	-0.64	3.72	5.97E-08	3.83	1.55E-07	0.10	3.86
1250	6.88E-09	-0.52	3.20	1.87E-07	3.00	2.40E-04	1.39	3.39
1300	6.38E-07	-0.21	4.88	2.51E-06	4.66	2.30E-03	1.21	5.41

For magnesia-spinel evaluation, Norton-Bailey creep parameters determined with L-M algorithm also showed comparable results with those obtained using the GRG algorithm. Nevertheless the fit achieved for magnesia-spinel at lower temperatures was not as accurate as that obtained from magnesia-chromite curves, especially in the tertiary stage. A better fit was attained at higher temperatures, i.e. 1250 °C and 1300 °C. See **Fig. 24**.

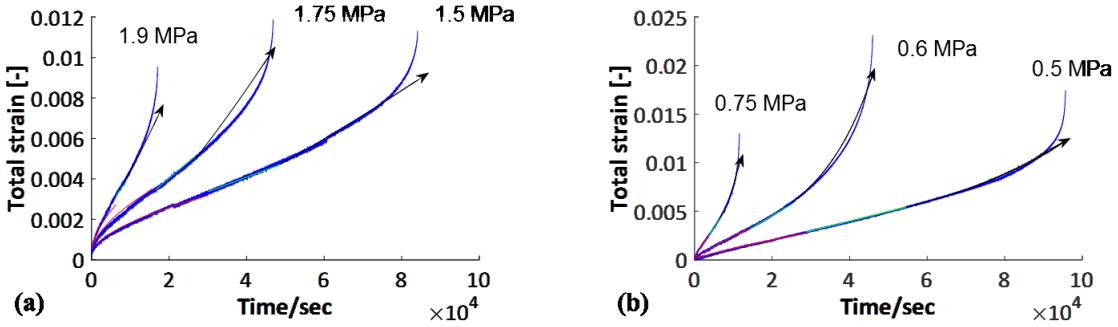

Figure 24: Measured (–) and inverse-estimated (→) total strains over time of magnesia-spinel bricks at (a) 1150 °C and (b) 1300 °C – L-M method.

Both methods for detecting the starting values show similar results despite the difference in the selection of the transition points. The evaluation with GRG algorithm was however more

constraining and more time consuming. In the future L-M will be utilized for the determination of the Norton-Bailey creep parameters. Matlab program could also be further improved with inverse-estimating to the transition points in order to achieve a higher performance.

3.5 Creep behaviour of magnesia-chromite

3.5.1 Ultimate strains and correlations

An additional study was carried on for magnesia-chromite material consisting on finding the correlations between the ultimate strain, stress and temperature collected from the tensile creep experimental results. The ultimate total strains at each of the three stages were considered for three temperatures; 1300 °C, 1400 °C and 1500 °C. **Figs. 25** and **26** illustrate the ultimate total strains with respect to the creep stage at 1400 °C and 1500 °C, respectively, under several applied loads.

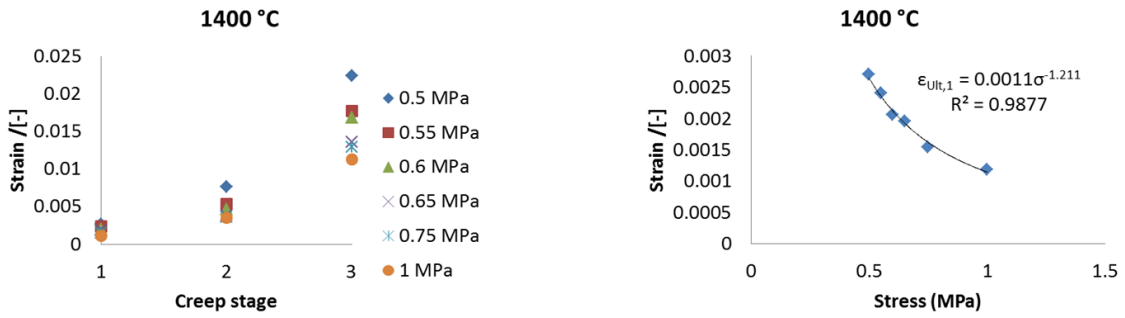

Figure 25: Ultimate primary total strains (a) with respect to creep stage and (b) the applied stress for the magnesia-chromite material at 1400 °C.

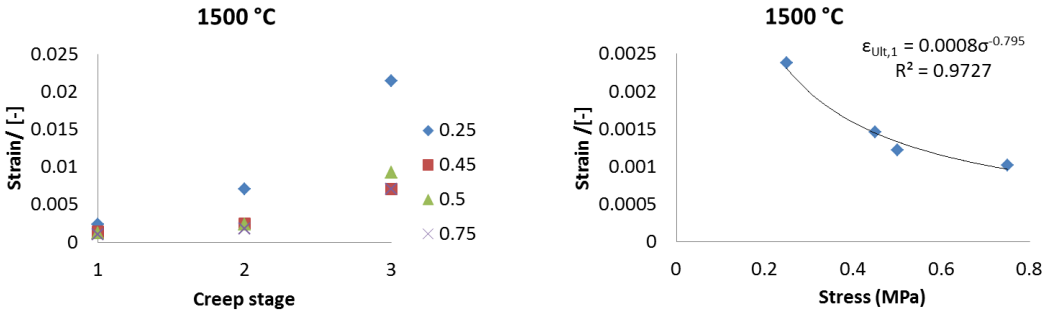

Figure 26: Ultimate primary total strains (a) with respect to creep stage and (b) the applied stress for the magnesia-chromite material at 1500 °C.

The ultimate strain regarding each stage is temperature and stress dependent; it is inversely related to the applied load and the temperature. Furthermore the longer the creep time the higher the ultimate strain. It is also noted that the difference in ultimate strain between two experiments at different load or different temperature increases with the creep stage, especially for a higher level of loads.

A correlation between the ultimate strains, stress and temperature makes it possible to identify the creep stage prevailing under these conditions. An approach can be implemented in a thermomechanical simulation program that will allow applying the corresponding creep parameters of each stage and therefore predicting the material behaviour and performance during service.

The results shown in **Figs. 25b)** and **26b)** suggest a representation of the ultimate strain for the primary stage in the following way:

$$\varepsilon_{Ult,1} = A_1(T)\sigma^{B_1(T)} \tag{37}$$

After verification, **Eq. 37** was then generalized for the three stages (See Appendix B).

$$\varepsilon_{Ult,1} = A_i(T)\sigma^{B_i(T)} \tag{38}$$

$A_i(T)$ and $B_i(T)$ are temperature dependent coefficients regarding to each stage, see **Fig. 27**.

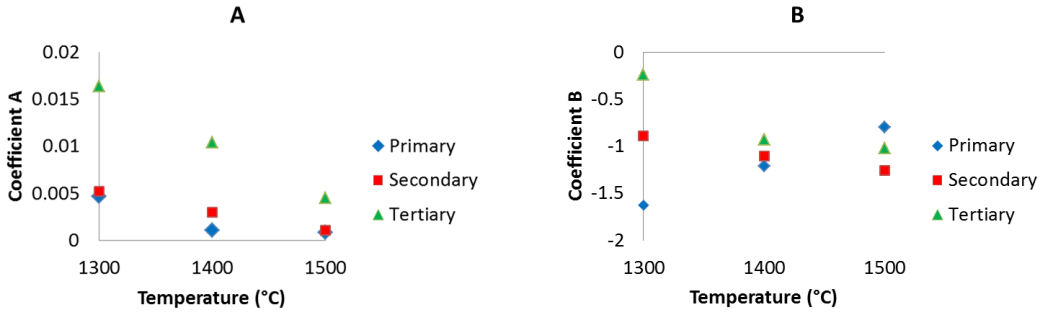

Figure 27: Temperature dependent coefficients $A_i(T)$ and $B_i(T)$ for all three creep stages for the investigated magnesia-chromite material.

The coefficients $A_i(T)$ and $B_i(T)$ will be applied to the FE simulation in the software Abaqus in order to predict the strain-hardening, steady-state and strain-softening behaviour of magnesia-chromite linings during operation.

Figs. 28 and **29** illustrate the ultimate total strains at 1400 °C, 1500 °C and 1600 °C under equivalent applied stresses.

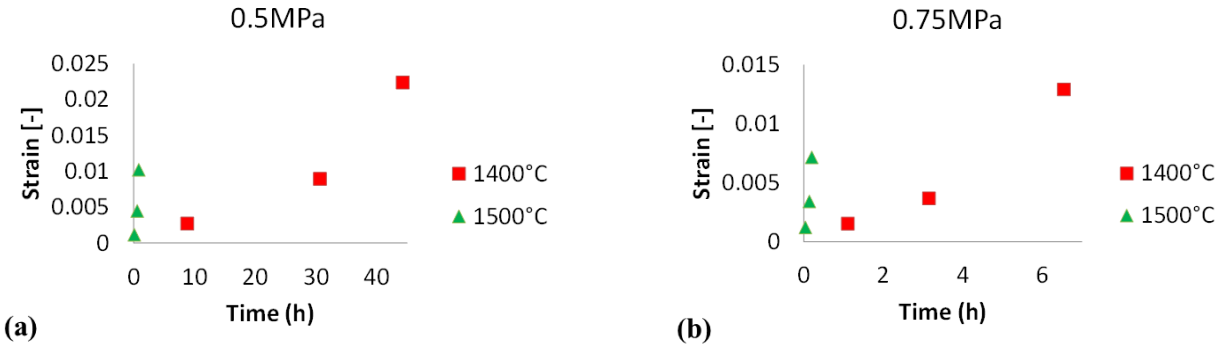

Figure 28: Ultimate total strains with respect to time at (a) 0.5 MPa and (b) 0.75 MPa for the investigated magnesia-chromite material.

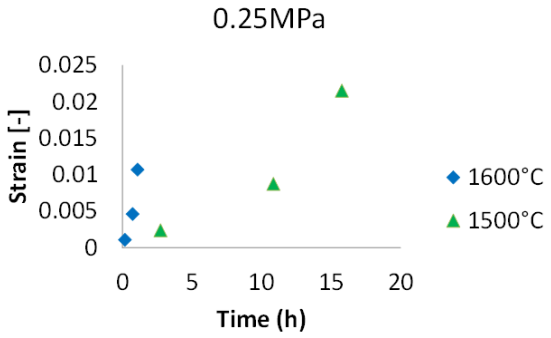

Figure 29: Ultimate total strains with respect to time at 0.25 MPa for the investigated magnesia-chromite material.

For similar applied load magnesia-chromite material underwent more intensive creep at higher temperature. The ultimate total strains corresponding to each stage diminished with the increasing temperature. Furthermore, by raising the temperature, creep time reduced dramatically inducing the reduction of the ultimate strains. The change in ultimate strains was more significant for the tertiary stage.

3.5.2 Arrhenius equation and creep behaviour

In chemical kinetics, the Arrhenius empirical law allows of describing the change in the rate of a chemical reaction depending on the temperature. It shows the dependence of the rate constant K of the reaction on the absolute temperature T. As already mentioned, the temperature dependent creep function can be written as the following:

$$K = A\,exp\left(-\frac{Q}{RT}\right) \tag{39}$$

Here Q is the activation energy, A is the pre-exponential factor and R is the universal gas constant. By introducing the logarithm Arrhenius' equation yields:

$$\ln(K) = \ln(A) - \frac{Q}{R}\frac{1}{T} \tag{40}$$

This means that ln (K) is a linear function of $1/T$. Thus if a reaction has a rate constant that obeys Arrhenius' equation, a plot of ln (K) with respect to T^{-1} gives a straight line. The gradient and intercept are used to determine Q and A. The activation energy is therefore defined to be ($-R$) times the slope of a plot of ln (K) vs. T^{-1}.

$$Q = -R\left[\frac{\partial \ln(K)}{\partial\left(\frac{1}{T}\right)}\right]_p \tag{41}$$

The activation energy of the magnesia-chromite material was determined during the steady-state creep in temperature range between 1300 °C and 1500 °C.

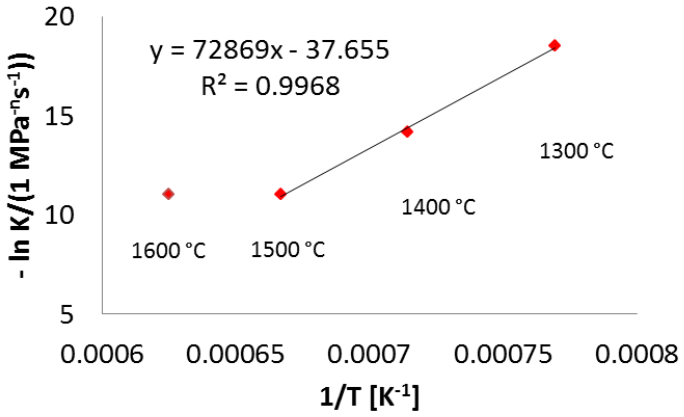

Figure 30: ln (K) with respect to ($1/T$).

Table 5: Activation energy calculated for magnesia-chromite material.

Stage II	Q (kJ/mol)	Q (kcal/mol)	A ($MPa^{-n}s^{-1}$)
1300-1500 °C	606.09	144.86	4.237E-17

Creep mechanisms are usually derived from the stress exponent and the grain size exponent mostly from the secondary stage and the activation energy. In this research creep mechanisms could not be investigated in that manner since the studied materials are heterogeneous and poly-disperse -that is, grain size dependence cannot be determined from the investigated materials alone. However, the graph representing -ln (K) with respect to $1/T$ suggests a change in creep mechanisms between 1500 °C and 1600 °C. In this temperature range and as the material shows a low C/S-ratio it is clear that the variations in the creep parameters are a consequence of formation of high amount of liquid phase.

3.6 Conclusions

Tensile creep was detected for magnesia-chromite and magnesia-spinel refractories at various temperatures and loads. Measurements were performed at 1300-1600 °C under loads between 0.2 MPa and 1.75 MPa for magnesia-chromite materials and at 1100-1400 °C under loads from 0.25 MPa to 1.90 MPa for magnesia-spinel materials. Three creep stages were distinguished at these conditions representing the strain-hardening, the steady state creep and the strain-softening behaviours of the materials. Evaluation was performed using a newly developed approach that comprised the choice of Norton-Bailey creep law for the interpretation of the experimental results, the identification of the creep stages and the calculation of the creep parameters by inverse estimation using the GRG or the L-M methods.

a. Magnesia-chromite material

In **Table 1** individual creep parameters were identified at each applied temperature for magnesia-chromite material. A second table can be provided showing common creep parameters determined for different temperatures. The values for the parameters *a* and *n* are valid at 1300-1500 °C for the primary creep stage. Only two parameter sets are therefore necessary, one at 1300-1500 °C and another at 1600 °C, instead of the four intended for each temperature. At 1400 °C and 1500 °C for the secondary and tertiary creep stages it is also possible to reduce the number of parameter sets. **Table 6** illustrates the common creep parameters for magnesia-chromite material.

Table 6: Common creep parameters n_i, a_i and K_i [MPa^{-n} s^{-1}] for magnesia-chromite bricks at 1300-1600 °C.

Stage	I			II		III		
T(°C)	K_1	a_1	n_1	K_2	n_2	K_3	a_3	n_3
1300	7.25E-09			9.48E-09	5.01	2.37E-06	1.14	7.48
1400	1.75E-07	-0.20	2.95	6.73E-07		2.79E-04		
					3.11		1.00	4.01
1500	3.55E-06			1.58E-05		1.07E-02		
1600	6.16E-06	-0.08	1.45	1.66E-05	1.69	1.05E-02	1.15	1.75

The application of Norton-Bailey creep law is appropriate to express the results for ordinary ceramic refractory materials. **Fig. 31** illustrates the experimental and the inverse estimated total strains at 1400 °C using the parameters of **Table 6**. The Norton-Bailey creep law identified by the inverse procedure presented above shows a satisfactory fit for all three creep stages. In the tertiary creep stage materials are expected to experience cavity coalescence, crack growth and possible necking phenomena before rupture [126]. Because the Norton-Bailey law does not take into consideration the crack growth, estimated curves slightly deviated from the experimental ones for the tertiary creep stage. The graphs corroborate the agreement between the measurements and the calculated total strains using the common creep parameters.

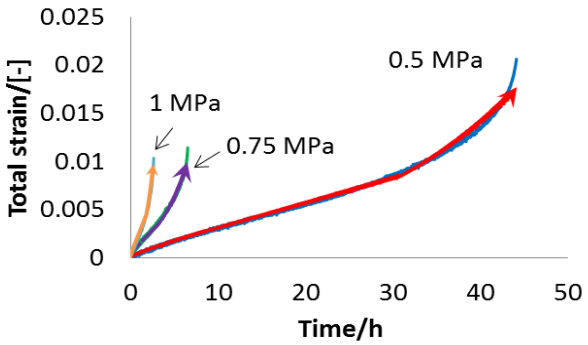

Figure 31: Measured (–) and inverse-estimated (→) total strains over time of burnt magnesia-chromite bricks at 1400 °C.

Creep mechanisms and changes of creep parameters are not yet addressed in this work. Indeed, there is no explanation for the reduction of the stress exponent *n* at the secondary and tertiary creep stages from 1300 °C to higher temperatures. However, the lower values of the strain exponent *a* at 1600 °C and a large difference in the values of the stress exponent *n* compared to those at the lower temperatures suggest a change in creep mechanisms. At this high temperature with a low C/S-ratio it is obvious that the variations in the creep parameters were due to a high amount of liquid phase formation. Valuable further research should also focus on structural influences on creep, especially the amount of fines. Further structural changes during the creep process including crack growth observation in stage 3 may be of high relevance.

b. Magnesia-spinel material

Common creep parameters, applied for several temperatures, were also investigated for magnesia-spinel material. The values of the parameters *a* and *n* are similar at 1200 °C and 1250 °C for the primary and secondary creep stages. Three parameter sets are therefore necessary instead of four, one at 1150 °C, a second one at 1200-1250 °C and a third one at 1300 °C. At

1200 °C and 1250 °C for the tertiary creep stage it was not possible to reduce the number of parameter sets. **Table 7** exhibits the common creep parameters for magnesia-spinel material. **Fig. 32** illustrates the experimental and the inverse estimated total strains at 1400 °C using the parameters of **Table 7**.

Table 7: Common creep parameters n, a and K [MPa^{-n} s^{-1}] for magnesia-spinel bricks at 1150-1300 °C.

Stage		I		II		III		
T(°C)	K_1	a_1	n_1	K_2	n_2	K_3	a_3	n_3
1150	4.60E-11	-0.85	5.29	8.33E-09	5.30	5.03E-08	0.25	5.20
1200	1.23E-09	-0.74	2.94	5.97E-08	3.38	1.55E-07	0.10	3.86
1250	6.88E-09			1.87E-07		2.40E-04	1.39	3.39
1300	6.38E-07	-0.21	4.88	2.51E-06	4.66	2.30E-03	1.21	5.41

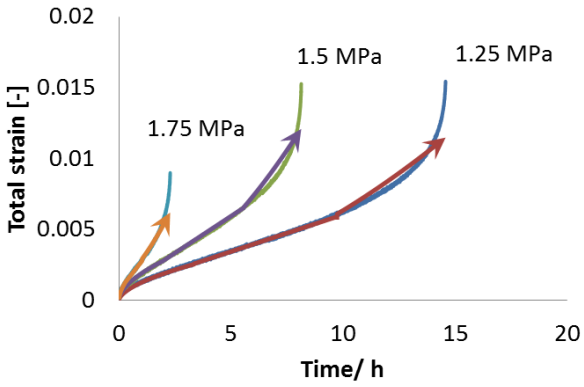

Figure 32: Experimental (–) and inverse-estimated (→) total strains over time of magnesia-spinel bricks at 1200 °C.

Creep mechanisms for magnesia-spinel have also not been subjected to study; the material being as much heterogeneous as magnesia-chromite. However, it was observed by visual inspection at the end of the test that damage accumulation was more intense for magnesia-spinel material. Its Young's modulus in dependence with the temperature shows a hysteresis because the material is known to have a high density of microcracks [127]. The microcracks present in the material close during preheating; at 1200-1250 °C Young's modulus of the material is at its maximum. During

cooling it reaches at 900 °C a second maximum, which is equal to app. the double of the maximum value during heating. The damage observed at the end of testing could also have been caused during cooling.

Norton-Bailey creep parameters were determined according to two procedures that used the GRG or the L-M algorithm. Both methods showed comparable results. In the first evaluation (that uses GRG algorithm) the first derivative of the polynomial fit was considered to determine the transition points. Despite the fact that this procedure allowed of inverse-estimating the transition times $ts,_2$ and $ts,_3$ the evaluation was constraining and time consuming. On the other hand the evaluation that uses L-M was more rapid and efficient. This second method considers the third derivative of the polynomial fit for the detection of the transition points and does not take into consideration their inverse-estimation. A further improvement of L-M programming can be considered with implementing an inverse-estimation of the transition points.

Chapter 4: Application of tensile creep data for a case study

4.1 Introduction

In 1950s, RH (Rurhstahl Heraeus) degassers were developed for secondary steelmaking processes in Germany with the purpose of generating quality steel by decreasing the hydrogen content so that "hair crack" formation is lowered. Since then, their function was enlarged to produce high quality steel which contains low hydrogen, low nitrogen and low total oxygen contents, as well as ultra-low sulphur and carbon contents. Many existing vacuum treatment techniques are employed for degassing purposes. Their process depends on the requirement for the steel grade to be produced. For instance, the Vacuum Tank Degassing (VTD) encourages good conditions in terms of sulphur removal for the reason that during molten steel treatment high slag-metal interaction occurs, whereas lower slag-metal interaction takes place during RH treatment [128]. If desulphurization is required to be conducted on RH plant, an assortment of fluxes, like CaO and Al_2O_3, is blown during RH treatment via a lance on the surface of molten steel. Nowadays, RH vacuum degassing facilities are integrated more frequently compared to VTD ones in the steel production line. The main motives are the high mixing performance, short cycle time for decarburization and degassing which increases the daily number of heats. RH degasser is composed of two vessels (upper and lower) in addition to inlet and outlet snorkels which are considered as insertion and evacuation chambers when immersed into the liquid steel. The assembly of their cylindrical shape is complex and time consuming. Snorkels are made of shaped refractories; viz. magnesia-chromite bricks, monolith refractories (concrete), and are reinforced and maintained by a steel structure, See **Fig. 33**.

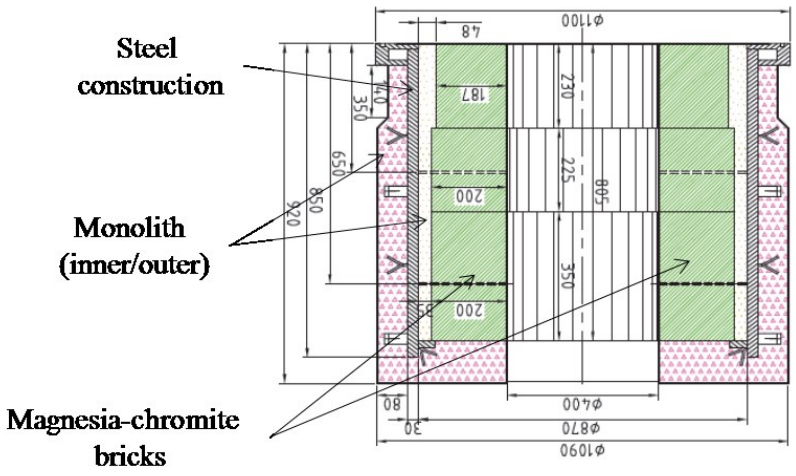

Figure 33: Inlet snorkel including steel construction and refractory linings (Voestalpine construction drawing).

Prior to RH process, the water bound by monoliths is evaporated by drying the interior of the snorkels during e.g. 35 hours at a temperature of 550 °C. This evades any case of failure caused by high vapour pressure. The snorkels are then fixed to the lower vessel and conveyed to the whole degasser entity. The RH degasser is an essential reactor for the metallurgy plants that involves complex reactions between molten steel, gas, slag, inclusions, and refractories [129]. The vessel is preheated from the top by means of a lance burner with the aim of decreasing the thermal shock instigated during submersion into the molten steel. The preheating is carried on for 7 hours, nevertheless at the end of the preheating the temperature of the upper parts varies from 500 °C to 200 °C comparing to the lower parts. The snorkels are then submerged into the liquid steel with a temperature of 1600 °C. After 35 minutes the snorkels emerge from the steel and hold on for a further cycle of immersion. During process the steel construction flange is water cooled at about 50 °C. Snorkel lifetime prediction withstands a great number of heats. The process engenders deterioration of the linings through long thermal cycling and severe thermal shock by cracking formation, spalling and corrosion [130, 131]. This leads to a frequent maintenance of the snorkels with adequate refractory mixes [132, 133]. The study of the behaviour of these types of lining materials that endure intensive thermal stresses may apply various damage and crack models [134, 135, 136 and 137]. For instance, the fictitious crack model according to Hillerborg [138] can be established for the simulation of crack formation by applying the strain softening behaviour of the material. The model assumes a linear stress-strain relation for the unaffected material, while a linear or non-linear stress-crack opening relation describes the crack propagation by considering a fictitious crack with cohesive forces acting between its faces. The failure mode of refractory materials under compression depends on the stress state and may be triggered by either tensile or shear stresses. This mode of failure can be described by the Drucker-Prager yield criterion [139]. It is a pressure-dependent model for determining whether a material has endured plastic yielding or failed. The shear strain energy criterion of von Mises is considered and the criterion is defined in terms of the principal stresses related to the hydrostatic pressure, the material cohesion and the friction angle function. The difference between Drucker-Prager creep model and the classical creep model is that the first one considers the elastic region in addition to the plastic deformation.
Creep with no doubts plays an important role in the material response when subjected to high stresses and elevated temperatures; the irreversible strain response of refractories in operation contributes intensively. Only few researchers investigated creep of linings [140, 141 and 142] mainly with the purpose of improving their design without having reflective depiction of creep impact.

This last chapter discusses creep applied to the RH snorkel during one heat including the preheating, the immersion and the idle time. Three creep models applied to magnesia-chromite bricks were implemented in Abaqus software: symmetric creep model with tensile data (1300-1600°C), symmetric creep model with compressive data (1100-1550°C) and asymmetric creep model including both tensile and compressive data. Magnesia-chromite bricks behaviour is discussed with respect to temperature and stress distributions at each stage of the process

(preheating, immersion, idle time). The Norton-Bailey strain hardening constitutive law was applied for the description of the three creep models.

4.2 Creep model applied to the RH snorkel

Three-dimensional geometry with radial and axial symmetries defines the model as the snorkel is of cylindrical shape. The parts included were the magnesia-chromite bricks, the inner and outer monoliths (concrete) and the steel construction, see **Fig. 34**. Three magnesia-chromite bricks were disposed in the same way as during process. The bricks are lengthwise in contact to the inner monolith and in the axial direction the lower magnesia-chromite brick is in contact with the outer monolith. The steel construction is arranged between the inner and outer monoliths. The process was simulated with three distinct and continuous steps: the preheating, the submerging and the emerging of the snorkel. Material properties, i.e. conductivity, density, Poisson ratio, Young's modulus, etc., were assigned to each of the bricks type and to the steel construction. The preheating lasted for 7 hours and was simulated with increasing the temperature of the hot face. Adequate temperature dependent heat transfer coefficients and temperatures up to 200 °C, 300 °C, 400 °C and 500 °C were applied at each of the magnesia-chromite and concrete outer (**Fig. 34**).

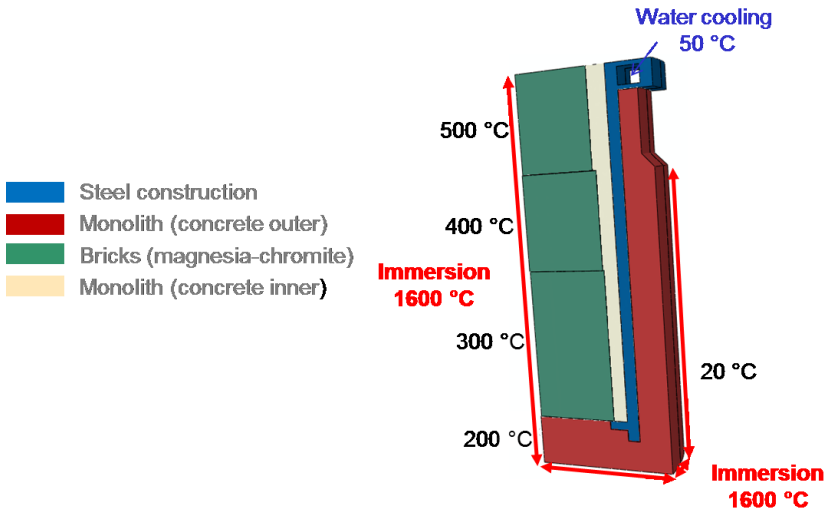

Figure 34: Snorkel illustration in a 3D model.

An initial temperature of 20 °C was applied in the upper outer part of the geometry with a temperature dependent heat transfer coefficient. The process, namely the submerging, lasted 35 min. It was modelled by harshly increasing the temperature of the outer concrete and magnesia-

chromite bricks to 1600 °C and applying a severe heat transfer coefficient. Water cooling of the flange was created with a temperature of 50 °C. Creep was simulated during process by applying Norton-Bailey creep parameters. Only the creep strain hardening approach was considered in this model. As mentioned previously, a symmetrical creep model was first computed with the compressive creep parameters applied between 1100 °C and 1500 °C [143], and then a second symmetrical creep model was computed with the tensile creep parameters applied between 1300 °C and 1600 °C. Finally an asymmetrical creep model applying compressive creep parameters at 1100-1500 °C and tensile creep parameters at 1300-1600 °C was carried out. The performance of the asymmetrical creep model needed a subroutine to be implemented in Abaqus software. The program used was according to Jin [144]. The emerging, or idle time, was simulated for 25 min by deactivating the intensive heating. A temperature history of the central magnesia-chromite brick is shown in **Fig. 35**. Creep was applied to magnesia-chromite lining only, the steel construction and the monoliths were assigned a linearly elastic behaviour.

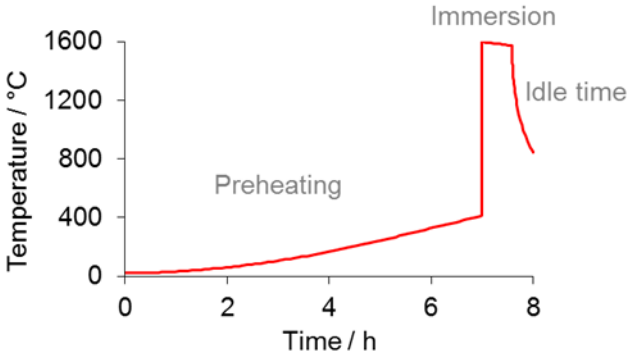

Figure 35: Temperature history of the central magnesia-chromite brick during preheating, immersion and idle time.

4.3 Simulation results

4.3.1 Temperature distribution

Temperature gradient of the snorkel is presented in the following figures (**Figs. 36**, **37**, **38**). The colour scale from red to blue indicates higher and lower temperatures, respectively. At the end of the preheating the upper part of the working lining reached a maximal temperature of 439.2 °C at its hot face approaching the defined target temperature of 500 °C. The central and lower bricks reached maximal surface temperatures of 366 °C and 292.8 °C. The outer concrete showed a relatively low temperature of 183 °C at its surface.

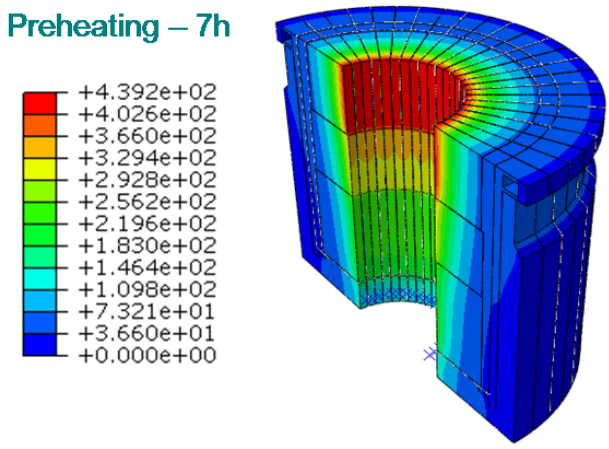

Figure 36: Temperature distribution in the snorkel at the end of the preheating – 7 h.

The submerging was simulated by a quick temperature increase of the working lining at its surface. As expected the maximum temperature of 1600 °C was found at the magnesia-bricks surface, which represents the hot face. Minimum temperature, equal to app. 50 °C was situated at the cold ends. At the end of the submerging the hot face temperature still keeps its maximum value of 1600 °C. Magnesia-chromite bricks endured a severe hot thermal shock. The outer concrete also endured thermal shock. Due to thermal conductivity of the material, temperature propagated through the lining thickness (See **Fig. 37**).

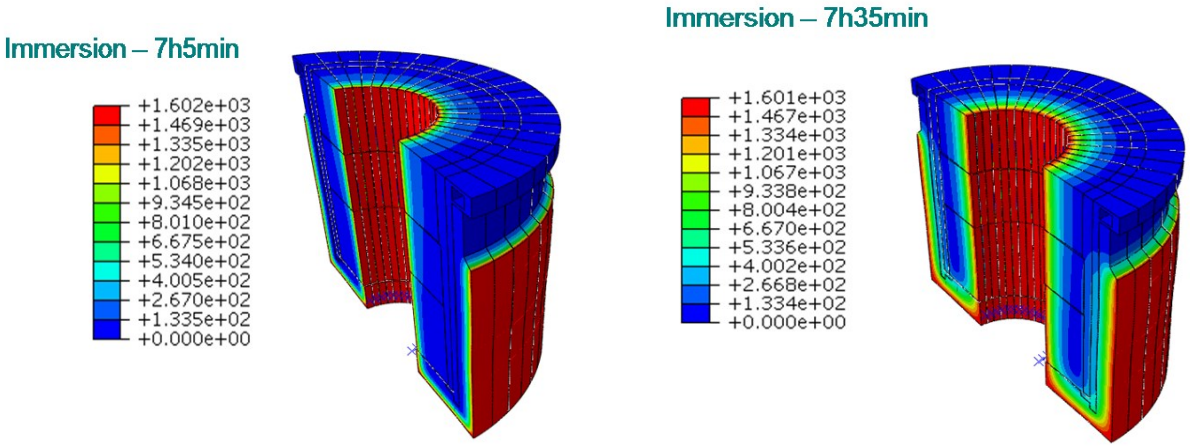

Figure 37: Temperature distribution in the snorkel at (a) the beginning (5 min) and (b) the end (35 min) of the submerging.

After immersion the emerging follows. The temperature of the snorkel at the end of the idle time is illustrated in **Fig. 38**.

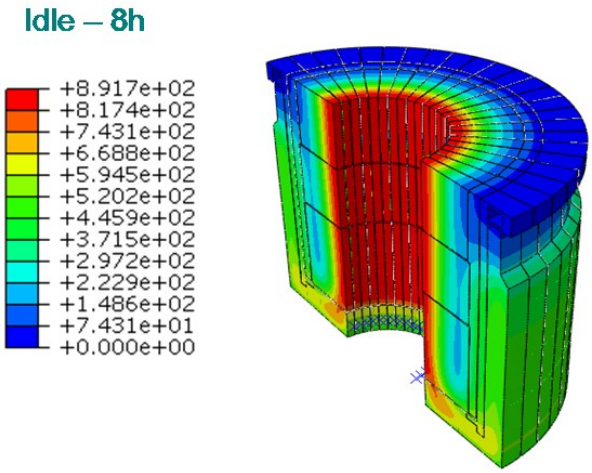

Figure 38: Temperature distribution in the snorkel at the end of the idle time – 8 h.

After 8 hours (end of idle time) the hot face temperature has decreased to approximately 892 °C but the heat still propagated in radial and circumferential directions as a result of heat diffusion from the outer surfaces (magnesia-chromite bricks and outer concrete) to the inside of the snorkel. The propagation of the heat through the working lining thickness continues to rise during the idle time. As a consequence the cold end temperatures grew over the entire length of magnesia-chromite bricks up to 148.6 °C (upper part) and 446 °C (lower part). However, the temperature of the snorkel was relatively low before the next immersion.

4.3.2 Stress distribution

Fig. 39 illustrates the state of the working lining in terms of temperature and stress distribution at the end of the preheating. The colour gradient from red to blue indicates higher and lower stresses, respectively. After 7 hours preheating the maximal temperature was located at the surface of the upper brick. The axial stresses in this area reached a maximal tensile value of 14.5 MPa. At this state the bricks, although having different temperatures, showed low stresses. Creep did not occur at these levels of temperature.

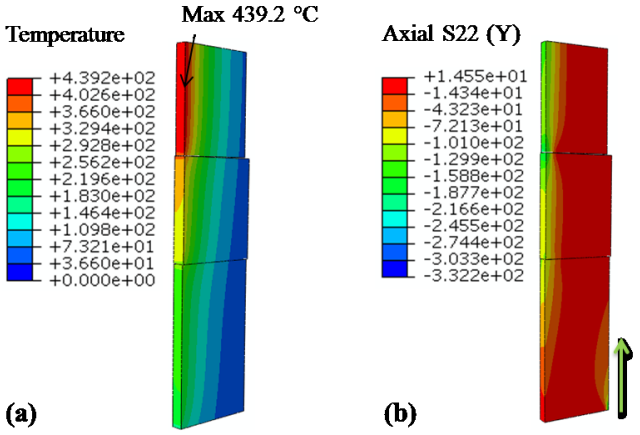

Figure 39: (a) Temperature and (b) stress distribution at the end of the preheating for magnesia-chromite bricks.

The stresses state during process (submerging) and idle time are observed and compared between different creep models. This is shown in the next sections.

4.3.3 Creep models comparison

As mentioned above, three creep models were simulated and applied to magnesia-chromite bricks: The symmetrical compressive model, the symmetrical tensile model and the asymmetrical model that considers different creep behaviour of the material when under tension and compression. **Fig. 40** shows the axial stresses of the three creep models for magnesia-chromite bricks after 2 minutes of submerging.

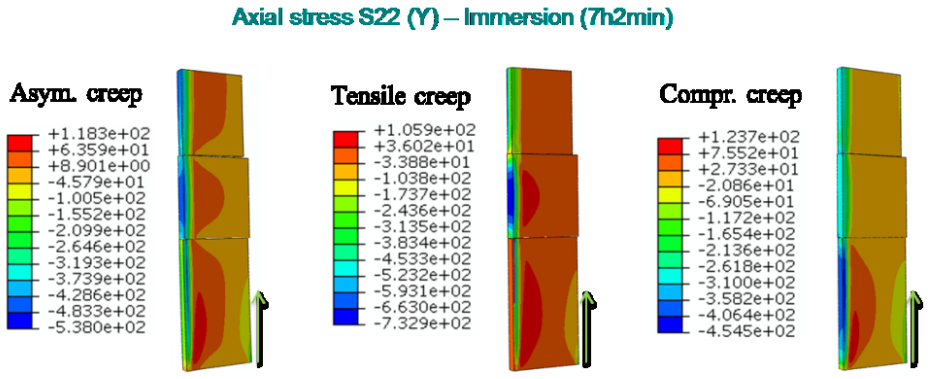

Figure 40: Axial stresses distribution (S22) – comparison between the three creep models after 2 min of submerging.

The stress distribution differed with the applied model. The highest compressive stresses were concentrated at the hot face of the lower brick for the compressive model, whereas they were situated in the central brick for the tensile model. The asymmetrical model presented a more realistic stress distribution with high compressive stresses at the hot face of the three bricks followed by tensile stresses in some distance from the hot face. Tensile stresses further decrease with the increasing distance from the hot face.

Fig. 41 presents the axial stresses and the axial irreversible strains with respect to time during the first minutes of the submerging. The node at the hot face of the lower brick was selected. The chosen node for stresses and strains observations is shown in **Fig. 42**.

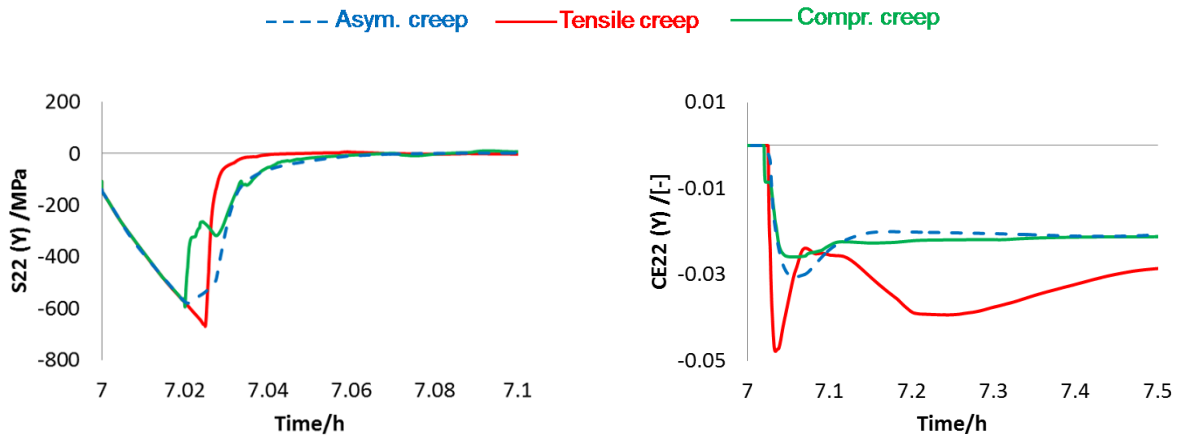

Figure 41: (a) Axial stresses and (b) axial irreversible strains with respect to time during the first minutes of the submerging.

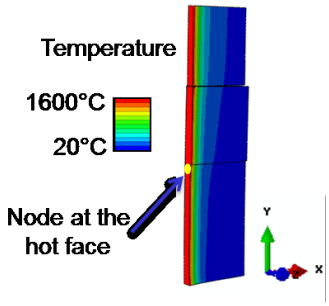

Figure 42: Node selected at the hot face for axial stresses and axial irreversible strains observation in Fig. 41.

Axial stresses decreased severely as the brick endured thermal shock. The hot face was under compression. Lower values (viz. higher absolute values) of S22 (Y) for the tensile creep model were observed; -670.23 MPa for the tensile creep model and -594.85 MPa for the compressive model. The material was assumed to behave linear elastically prior to creep. Compressive creep was applied in a range of 1100-1550 °C and tensile creep in a range of 1300-1600 °C. As soon as creep took place, the axial stresses for both tensile and compressive creep models sharply increase up to a near-zero value. Creep led to a release of the stresses inside the brick. The increase of stresses occurred earlier for the compressive creep model comparing to the tensile one. It happened already at 1100 °C. The presence of intense stresses engendered a high irreversible deformation of the brick. Compressive irreversible creep strains (CE22), already high, decreased until values of -0.025 and -0.023 for the tensile and the compressive creep models, respectively, see **Fig. 41b)**. At 7.1 h for the tensile model, CE22 decreased again to -0.04 before finally stabilizing to -0.026 at 7.5 h, whereas for the compressive model CE22 stabilized earlier to a higher value of -0.020. The asymmetric creep model presented smother curves. The increase of axial stresses and irreversible strains was not as sharp as for the symmetrical ones. The three models show different behaviours, although the asymmetrical creep model approached the compressive symmetrical model. As under thermal shock compressive stresses emerged in the short laps of time following the thermal shock.

The following figure, **Fig. 43a)**, shows the axial stress distribution after 5 minutes of submerging. The hot face was under high thermal shock. Low compressive axial stresses were noticed (area 1). Higher compressive stresses were now at a small distance from the hot face (area 2). In area 3 high tensile stresses were found, as the temperature at this area was lower than at the hot face. High levels of radial compressive stresses were present. The heat was diffusing through the width of the bricks. **Fig 43b)** illustrates the axial stresses along the width of the brick for the three creep models 5 minutes after immersion (see sketch in **Fig.43b)**). Here as well extremely high tensile stresses were observed for the tensile model because creep was applied only for temperatures exceeding 1300 °C. As the heat transferred inside the brick, creep occurred and instigated a release of stresses. Tensile stresses appeared at a distance larger than app. 50 mm. Compressive and asymmetrical models present lower values of compressive stresses near to the hot surface (about 20 mm). For these two models tensile stresses appeared already at a distance of app. 35 mm from the hot face. In the cold end the three models converged together and show app. similar and relatively low compressive stress values.

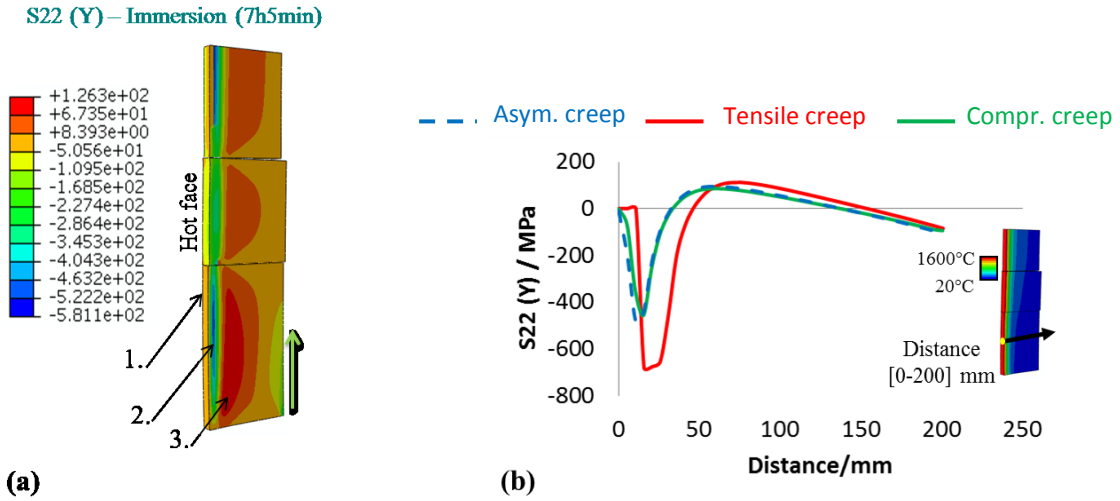

Figure 43: a) Axial stresses distribution (S22) and b) axial stresses with respect to time along the brick – after 5 min of submerging.

The next figure (**Fig. 44**) illustrates the axial stresses at the end of the submerging. No compressive stresses were present at the hot face. The stresses were propagating along the brick, which pointed out a more significant opening of the joints (see **Fig. 44a)**). Maximal compressive stresses were at a distance of app. 30 mm from the hot face for the three creep models.

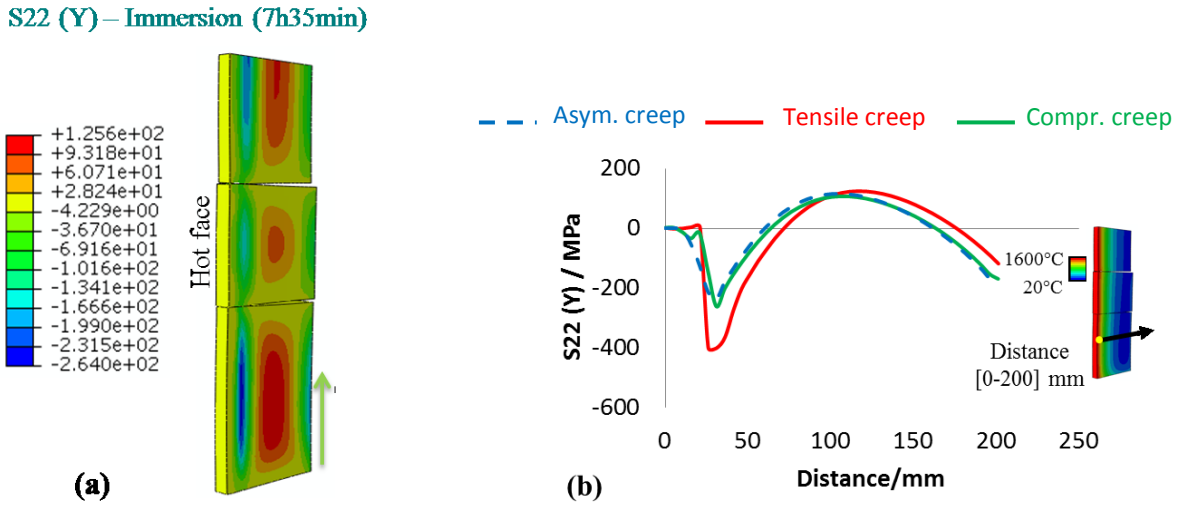

Figure 44: a) Axial stresses distribution (S22) and b) axial stresses with respect to time along the brick – at the end of submerging.

Tensile stresses covered a high area of the brick in its centre. Here also the three models show similar values of stress when approaching the cold end with the compressive model being the closest to the asymmetrical one.

Axial irreversible strains were also observed at the end of submerging. **Fig. 45** illustrates the irreversible strain distributions in the axial direction at the end of the process. In **Fig. 45a)** one can see high compressive strains (up to -0.02) between the bricks at the hot face. The joints were on the other hand opened in the cold end. **Fig 45b)** shows the difference in evolution of the axial creep strains along the brick for the three creep models. At the hot surface the irreversible strains were equal to about -0.008 in the three models. With a further increase of the distance from the hot face the irreversible axial strains diminished up to nearly zero. The tensile creep model overestimated the axial irreversible strains and the compressive creep model underestimated them, whereas the asymmetrical creep model showed smother and more or less the mean progression of the strains along the brick.

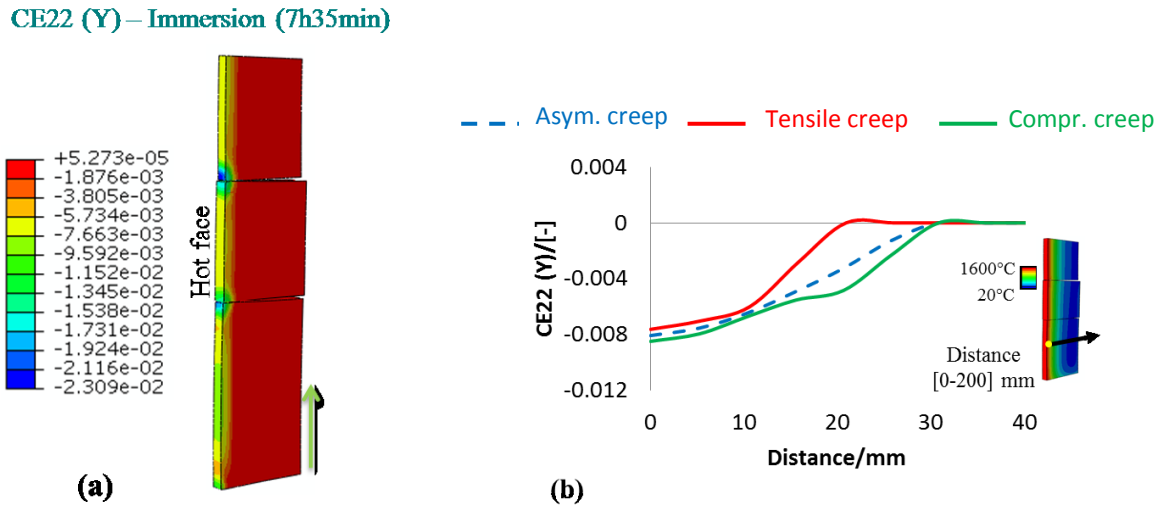

Figure 45: a) Axial irreversible strain distribution (CE22) and b) axial irreversible stain with respect to time along the brick – at the end of submerging.

It was interesting to compare the symmetrical and asymmetrical creep models in terms of stress and strain distributions. Due to the fact that the working lining endured hot thermal shock, the compressive creep model presented more comparable results to the asymmetrical one.

4.3.4 Asymmetrical creep model evaluation

Stresses in the axial (Y), radial (X) and circumferential (Z) directions are plotted over the whole process at a distance of 15 mm in the radial direction from the hot face in **Fig. 46a)**. The chosen node is shown in **Fig. 47**. Intensive decrease of stresses was observed not only in the axial but also in the circumferential direction at the beginning of the immersion causing irreversible deformation of the brick (see **Fig. 46b)**). Important radial irreversible strains (CE11) are noticed although there was nearly no variation of the radial stresses (S11) at that area. The reason is because the applied creep model refers to a constant volume of the material. If the material is compressed in two directions, an expansion in the third direction is assumed to achieve a constant volume. Nevertheless in this simulation damage was not taken into account. The evolution of CE11 with respect to time showed therefore an expansion in the radial direction and not a tensile deformation. The third direction is counterbalancing the two others.

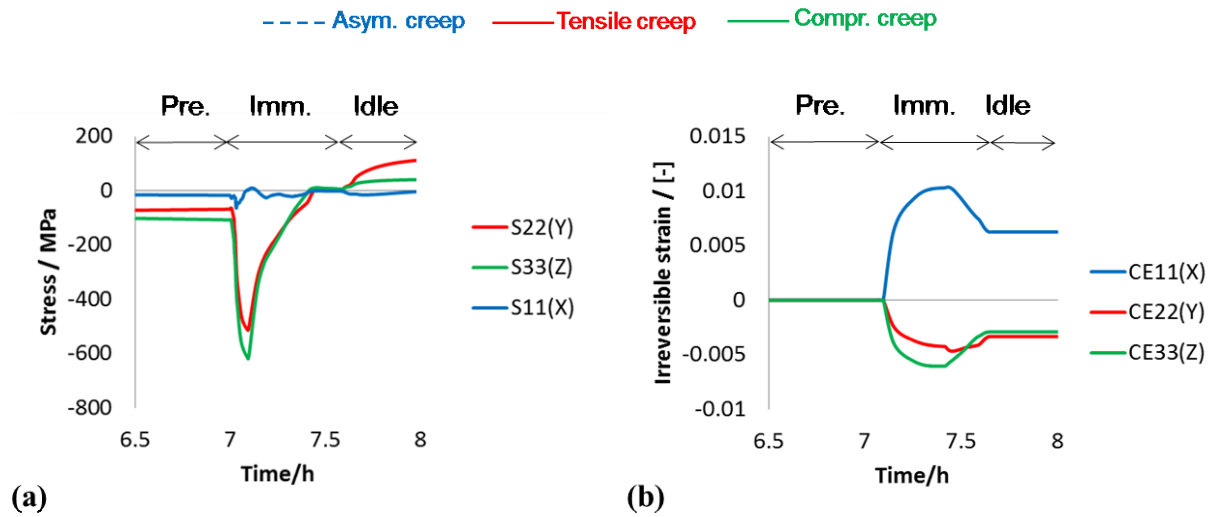

Figure 46: Axial (Y), radial (X) and circumferential (Z) (a) stresses and (b) irreversible strains over time at a distance of 15 mm from the hot face – considering asymmetrical creep.

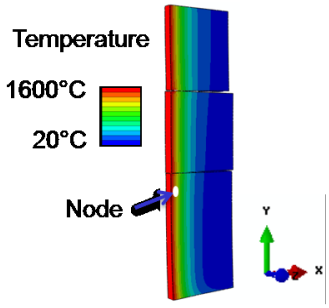

Figure 47: Node selected for stresses and irreversible strains observation at a distance of 15 mm from the hot face (representing 7.5 % of the brick thickness) – considering asymmetrical creep model.

The opening of the vertical joints between the working lining bricks was observed at different moments of the submerging. **Fig. 48a)** represents the contact opening after 1 min, 16 min and 35 min of the submerging with respect to the distance along the brick. The selected distance coordinate is shown in **Fig. 49**.

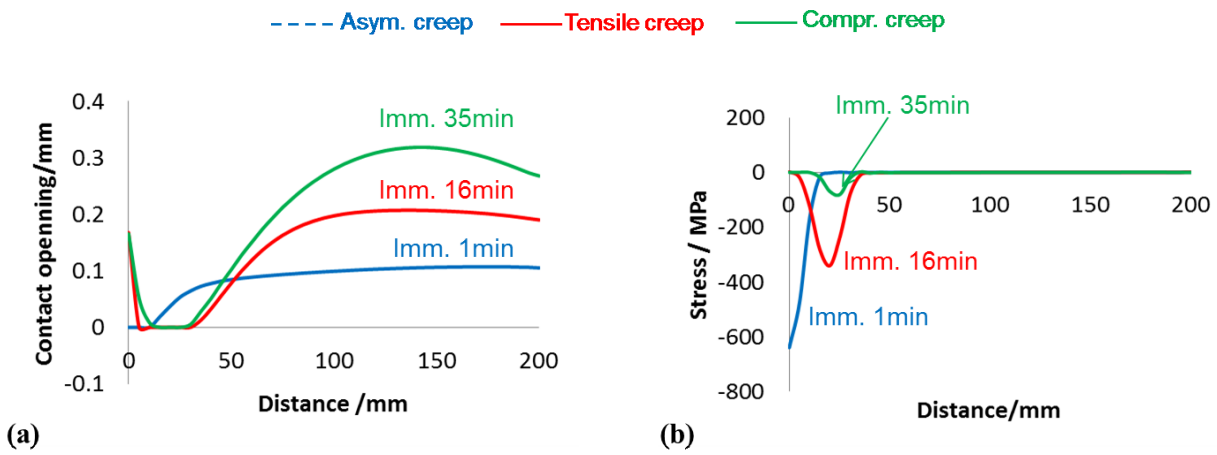

Figure 48: (a) Contact opening and (b) circumferential stresses (S33) along the brick at different moments of the submerging – for the asymmetrical creep model.

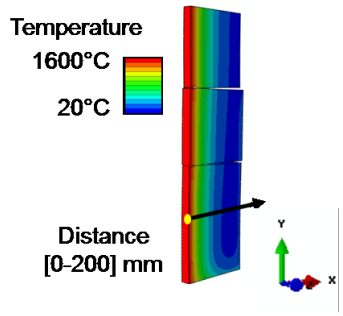

Figure 49: Coordinate selected for depicting the contact opening and circumferential stresses in Fig. 48.

Joint opening occurred immediately after immersion, but not at the hot face. After 1 min immersion, the joint opened at a distance larger than 10 mm from the hot face. The opening continued up to a maximal value of 0.1 mm through the whole width of the brick. Accordingly, the circumferential compressive stresses (S33) at this moment of the process, although extremely high at the hot face, decreased along the lining width and vanished starting at app. 10 mm. Joints are closed at locations of compressive stresses near to the hot face. They may be opened where compressive stresses vanish. After 16 min of immersion the absolute values of compressive circumferential stresses were reduced, but they extended to about 20 mm from the hot face, as the heat diffused through the lining. The opening of the joint reached a value of up to 0.2 mm in the stress free region. At the end of the process the opening of the joint was equal to 0.3 mm as a consequence of a further reduction of the circumferential compressive stresses. For further heats the joint opening will increase. It is clear that the creep participated in the reduction of the compressive stresses. Moreover, at the end of the immersion, the areas close to the hot face presented nearly no stresses.

4.4 Conclusion

Three creep models were applied to the RH snorkel which are the symmetrical tensile, the symmetrical compressive and the asymmetrical one. One heat was simulated including the preheating, the submerging and the emerging of the vessel. Temperature and stress distributions at each stage of the process were shown. A detailed comparison between the creep models revealed that the asymmetrical model presented smother curves of stresses during thermal shock and showed more realistic results for describing the snorkel behaviour. It is more representative than tensile and compressive creep models. Nevertheless, the compressive model results approached the asymmetrical ones. It was clear that the temperature of the snorkel was relatively low before immersion; the preheating temperatures were not high enough to minimalize the thermal shock. The onset of temperature of creep could also have influenced the results. At the

immersion it was noticed that the area close to the hot face had nearly no stresses. For further heats this area will increase. Finally, joint opening occurred immediately at the immersion.

General conclusion

Refractory linings applied in pyro-processes are generally altered after a period of time since they are exposed to high mechanical loads at elevated temperatures. Their major role is to sustain such tough conditions in the long term. The behaviour of refractory materials under tensile loading is in general greatly affected by their creep strain. Therefore, it was important to quantify creep for a better understanding of the material performance and designing failure resistant systems. The present thesis aimed at investigating the creep of two refractory materials at high temperature. The setup permitted to detect three creep stages up to failure of the specimens in a reasonable time. Creep data were generated in a broad range of stress and temperature, which enabled the determination of parameters derived from Norton-Bailey creep constitutive law. The data were analysed according to two parameterization methodologies using the GRG and L-M algorithms. Asymmetric creep was finally applied to the RH snorkel during one heat including the preheating, the immersion and the idle time. The creep reduced considerably the stresses within the working lining. The reduction in stresses is especially influenced by the onset temperature of creep. This triggers a sensitivity study, both for the influence of creep parameters and the onset temperature. In the future, some further modelling efforts should be made to better understand the thermo-mechanical behaviour of whole lining systems applied in industrial vessels and furnaces. Accordingly, failure model associated to the asymmetrical creep model will be investigated and thus implemented in the simulation program.

References

[1]: Terwilliger G.R., Radford KC. High temperature deformation of ceramics: I, Background. J Am Ceram Soc 1974; 53(2): 172–173.

[2] Penny R.K., Marriott D.L. Design for creep. Chapman & Hall, London, 1995.

[3] Boyle J.T., Spence J. Stress analysis for creep. Camelot Press, London, 1983: p. 13–20.

[4] Kennedy A.J. Processes of Creep and Fatigue in Metals. Oliver & Boyd, London, 1962.

[5] Dorn J.E. Some fundamental experiments on high temperature creep. J. Mech. Phys. Solids, 1965: p. 3.

[6] Soderberg C.R. The interpretation of creep tests for machine design. Trans. ASME, 1936: p. 58.

[7] Mc Vetty P.G. Working stresses for high temperature service. Mech. Eng., 1943: p. 56. Mc Vetty P.G. Creep of metals at elevated temperatures – the hyperbolic sine relation between stress and creep rate. Trans. ASME, 1943: p. 65.

[8] Johnson A.E., Henderson, J. and Kahn B. Multiaxial creep strain/complex stress/time relations for metallic alloys with some applications to structures, in ASME/ASTM/I Mech E, Proceedings Conference on creep. Inst. Mech. E, New York/London, 1963.

[9] Norton F.H. the creep of steel at high temperatures. McGraw-Hill, London, 1929.

[10] Bailey R.W. The utilization of creep test data in engineering design. Proc. I. Mech. E., 1935: p. 131–149.

[11] Andrade E.N. da C. The viscous flow in metals and allied phenomena, Proc. R. Soc., 1910: p. 84.

[12] Graham A. and Walles K.F.A. Relations between long and short time properties of a commercial alloy. J. Iron Steel Inst., 1955: p. 179.

[13] Garofalo F. Fundamentals of creep and creep rupture in metals. MacMillan, New York, 1965.

[14] Arrhenius S.A. Ueber die Reaktionsgeschwindigkeit bei der Inversion von Rohrzucker durch Säuren. Z. Phys. Chem., 4, 1889: p. 226–248.

[15] Arrhenius S.A. Ueber die Dissociationswaerme und den Einfluß der Temperatur auf den Dissociationsgrad der Elektrolyte. Z. Phys. Chem. 4, 1889: p. 96–116.

[16] Laidler K. J. Chemical Kinetics, Third Edition, Harper & Row, 1987: p. 42.

[17] Shibli I.A, Holdsworth S.R., and Merckling G. Creep and Fracture in High Temperature Components – Design and Life assessment issues. Proceedings ECCC creep conference, London, 2005.

[18] Altenbach H. and Naumenko K. Modeling of Creep for Structural Analysis. Foundations of engineering mechanics, Springer Berlin Heidelberg, 2007: p. 128–138.

[19] Betten J. Creep mechanics. Springer, Berlin Heidelberg, 2003.

[20] Reveron H., Zaafrani O. and Fantozzi G. Microstructure development, hardness, toughness and creep behaviour of pressureless sintered alumina/SiC micro-nanocomposites obtained by slip-casting. J. Eu. Cer. Soc. 2010: 30, p. 1351–1357.

[21] Ivankovic H., Tkalcec E., Rein R. and Schmidt H. Microstructure and high temperature 4-point bending creep of sol-gel derived mullite ceramics. J. Eu. Cer. Soc. 2005: 26, p. 1637–1646.

[22] Calderón-Morenoa J.M., de Arellano-Lópeza A.R., Domínguez-Rodrígueza A. and Routbortb J.L. Microstructure and creep properties of alumina/zirconia ceramics. J. Eu. Ceram. Soc. 1995: 15, p. 983–988.

[23] Lin H.T., Alexander K.B. and Becher P.F. Grain size effect on creep deformation of alumina-silicon carbide composites. J. Am. Ceram. Soc.1996: 79(6), p. 1530–1536.

[24] Raj R. and Ashly M.F. On grain boundary sliding and diffusional creep. Metall. Trans. 1971: 2, p. 1113–1127.

[25] Snowden W.E., Pask J.A., Creep behavior of a model refractory system MgO-$CaMgSiO_4$. J. Am. Ceram. Soc. 1978: 61(5-6), p. 231–234.

[26] Luecke W.E. and Wiederhorn S.M. J. Am. Ceram. Soc. 1999: 82, p. 2769–2778.

[27] Wei Q., Sankar J. and Narayan J. Microstructural changes due to heat-treatment of annealing and their effect on the creep behaviour of self-reinforced silicon nitride ceramics. Mat. Sci. E. 2001: A299, p. 141–151.

[28] Johnson A.E., Henderson J. and Khan B. Complex-stress creep, relaxation and fracture of metallic alloys. National engineering laboratory, Edinburgh: H.M.S.O, 1962.

[29] Gooch D.J. and How I.M. Techniques for multiaxial creep testing. Elsevier Applied Science Publishers LTd, 1986.

[30] Boyle J.T., Spence J. Stress analysis for creep. Camelot Press, London, 1983: p. 39–55.

[31] Viswanathan R. Damage mechanisms and life assessment of high-temperature components. ASM Internationals, Ohio, 1989.

[32] Yao H.T., Xuan F.Z., Wang Z. and Tu S.T. A review of creep analysis and design under multi-axial stress states. Nuclear Engineering Design. 2007: 237(18), p. 1969–1986.

[33] Harry K. Creep analysis. Wiley, New York, 1980.

[34] Penny R.K., Marriott D.L. Design for creep. Chapman & Hall, London, 1995.

[35] Cannon W.R. and Langdon T.G. Review of creep of ceramics. Part 1: Mechanical characteristics. J. Mat. Sci. 1983: 18, p. 1–50.

[36] Pletka B.J., Heuer A.H. and Mitchell T.E. Work-hardening in sapphire (α-Al_2O_3). Acta Metall. 1977: 25, p. 25–33.

[37] Gooch D.J. and Groves G.W. Non-basal slip in sapphire. Phil. Mag. 1973: 28, p. 623.

[38] Routbort J.L. High-temperature deformation of cubic oxides. J. Physique, Colloque C3. 1981: 42, p. C3-59.

[39] Dryden J.R., Kucerovsky D.S., Wilkinson D.S. and Watt D.F. Creep deformation due to a viscous grain boundary phase. Acta Metall. 1997: 37(7), p. 2007–2015.

[40] Dryden J.R. and Wilkinson D.S. Three dimensional analysis of the creep due to a viscous grain boundary phase. Acta Mater. 1997: 45(3), p. 1259–1273.

[41] Chadwick M.M., Wilkinson D.S. and Dryden J.R. Creep due to a non-Newtonian grain boundary phase. J. Am. Ceram. Soc. 1992: 75(9), p. 2327–2334.

[42] Shanti V.N. and Jakus K. High temperature mechanical behaviour of ceramic composites. Butterworth-Heinemann, Boston, 1995.

[43] Andreev K., Zinngrebe E., Heijboer W.M., Ham P.J.N. v.d., Everstein S.J. Compressive behaviour of ACS torpedo bricks. In Proceedings of UNITECR 2009.

[44] Krause R.F. Compressive strength and creep behaviour of a magnesium chromite refractory. Ceram. Eng. and Sci. Proceedings, 1986: p. 220–228.

[45] Surendranathan A.O. An introduction to ceramics and refractories. CRC Press, Taylor and Francis Group, Boca Raton, 2015.

[46] Wiederhorn S.M. Particulate ceramic composites: their high-temperature creep behaviour. Key E. Mat. 2000: 175-176, p. 267–288.

[47] Bennet J.P. and Smith J.D. Fundamentals of Refractory Technology. Proceedings of the refractory ceramics division, Indiana, 2000.

[48] Ruggles-Wrenn M.B. and Whiting B.A. Cyclic creep and recovery behaviour of Nextel™720/alumina ceramic composite at 1200 °C. J. Eu. Cer. Soc. 2011: 528(3), p. 1848–1856.

[49] Volkmann E., Tushtev K., Koch D., Wilhelmi C., Grathwohl G. and Rezwan K. Influence of fiber orientation and matrix processing on the tensile and creep performance of Nextel 610 reinforced polymer derived ceramic matrix composites. J. Eu. Cer. Soc. 2014: 614, p. 171–179.

[50] Wilkinson D.S. Creep mechanisms in multiphase ceramics. J. Am. Ceram. Soc. 1998: 81(2), p. 275–299.

[51] Ye X., Hyers R.W. Computational methods for the analysis of, non-contact creep deformation, in ZrB2–SiC composites. J. Eu. Cer. Soc. 2010: 30(11), p. 2191–2196.

[52] Davies C.K.L., Oddy D., Reece M.J., Stevens R.N., Williams K., Fantozzi G., Olagnon C. and Torrecillas R. High temperature creep/fatigue of single or multi-phase ceramics with an additional Glass/liquid phase. Int. J. Mat. Prod. Tech. 2011: 2, p. 530–537.

[53] Massard L. Etude du fluage de réfractaires électrofondus du système alumine-zircone-silice. PhD thesis, Ecole Nationale Supérieure des Mines de Paris, 2005.

[54] Lange F.F. Non-elastic deformation of polycrystals with a liquid boundary phase. Deformation of ceramic materials, edited by Bradt R.C and Tressler R.E. Plenium press, New York, 1972: p. 361–381.

[55] Wei Q., Sankar J., Kelkar A.D. and Narayan J. Microstructure evolution accompanying high temperature; uniaxial tensile creep of self-reinforced silicon nitride ceramics. Mat. Sci. E. 1999: A272, p. 380–388.

[56] Cao J.W., Okada A. and Hirosaki N. Tensile creep behavior of a ytterbium silicon oxynitride-silicon nitride ceramic. J. Eur. Ceram. Soc. 2002: 22, p. 769–775.

[57] Ienny P. and Boussuge M. Determination of the creep behaviour of reaction-sintered ceramics using tensile testing. Proceeding of 2nd Eur. Ceram. Soc. Conference: Euro-Ceramics, Augsburg, Ed. Ziegler G. and Hausner H. 1991: 2, p.1221–1225.

[58] Lamouroux F., Vallés J.L. and Steen M. Influence of damage on the creep behaviour of ceramic matrix composites. Comp. Eng. 1995: 5 (10-11), p. 1379–1386

[59] Lamouroux F., Vallés J.L. and Steen M. Dual-stage tertiary creep of a ceramic matrix composite. Material Science and Engineering 1998: 250(2), p. 279–284.

[60] Chermant J.L., Boitier J., Darzens S., Farizy G., Vicens J. and Sangleboeuf J.C. The creep mechanism of ceramic matrix composites at low temperature and stress, by material science approach. J. Eur. Ceram. Soc. 2002: 22, p. 2443–2460.

[61] Casas L., Martinez-Esnaola J.M. Modelling the effect of oxidation on the creep behaviour of fibre-reinforced ceramic matrix composites. Acta Mater. 2003: 51, p. 3745–3757.

[62] Morscher G.N. Tensile creep and rupture of 2D-woven SiC/SiC composites for high temperature applications. J. Am. Ceram. Soc. 210: 30, p. 2209–2221.

[63] Almeidaa R.S.M., Tushteva K., Clauß B., Grathwohla G. and Rezwana K. Tensile and creep performance of a novel mullite fiber at high temperatures. Composites Part A: Applied Science and Manufacturing. 2015: 76, p. 37–43.

[64] Tsai R.L and Raj R. A theoretical estimate of solution-precipitation creep in MgO-fluxed Si_3N_4. Communication of the Am. Ceram. Soc., 1982: p. C-88–C90.

[65] Bradt, R.C., Brookes, C.A. and Routbort J.L. Plastic Deformation of Ceramics. Springer US, New York, 1995.

[66] Meléndez-Martíneza J.J., Jiménez-Melendoa M., Domínguez-Rodrígueza A. and Wötting G. Creep behaviour of two sintered silicon nitride ceramics. J. Eur. Ceram. Soc. 2002: 22(14-15), p. 2495–2499.

[67] Thurn G., Canel J., Bill J., Aldinger F. Compression creep behaviour of precursor-derived Si-C-N Ceramics. J. Eur. Ceram. Soc. 1999: 19(13-14), p. 2317–2323.

[68] Bakunov V.S., Gulaev V.M and Levi V.S. Creep mechanism in a corundum ceramic over a wide range of test conditions. High temperature institute, academy of sciences of the USSR. 1982: p. 356–358.

[69] Wereszczak A.A., Kirkland T.P., Curtis WF. Creep of CaO/SiO2-containing MgO refractories. J. Mater. Sci. 1999: 34, p. 215–227.

[70] Evans R.W., Scharning P.J. and Wilshire B. Creep of CaO/MgO refractories. J. Mater. Sci. 1985: 20, p. 4163–4168.

[71] EN 993-9, Methods of test for dense shaped refractory products. Determination of creep in compression. 1973.

[72] ASTM C832-00, Standard test method of measuring thermal expansion and creep of refractories under load, ASTM International, West Conshohocken, 2015.

[73] Matsumura I., Hayashi Y., Hiyama Y. and Ijiri A. Refractoriness under load and hot creep measurements. Taikabutsu Overseas. 1990: 2(2), p. 36–42.

[74] Chien Y., Lee T., Pan H., Ko Y. Effect of Cr_2O_3 on creep resistance of high alumina bauxite refractories. Ceram. Bull. 1984: 63(7), p. 915–8.

[75] Dixon-Stubbs P.J. and Wilshire B. High temperature creep behaviour of a fired magnesia refractory. Trans. J. British Ceram. Soc. 1981: 80, p. 180–185.

[76] Mong L.E. Elastic behaviour and creep of refractory bricks under tensile and compressive loads. J. Research NBS. 1947: 38, p. 229–240.

[77] Jin S., Harmuth H. and Gruber D. Compressive creep testing of refractories at elevated loads-device, material law and evaluation techniques. J. Eur. Ceram. Soc. 2014: 34(15), p. 4037–4042.

[78] Ferber M.K. Weresczak and A.A. Hemrick J.G. Compressive Creep and Thermo-physical performance of refractory materials. Technical report, US department of energy, 2006.

[79] Cranmer D.C. Workshop on assessment of testing methodology for glass, glass-ceramic, and ceramic matrix composites. Conference report, J. Research NIST 1991: 96(4), p. 493–501.

[80] Ohji T. Handbook of Advanced Ceramics. Testing and evaluation of mechanical properties, Tokyo Institute of Technology. 2nd ed. In: Somiya S, editor 2013: p. 633–656.

[81] Ferber M.K., Jenkins M.G. and Tennery V.J. Comparison of Tension, Compression, and Flexure Creep for Alumina and Silicon Nitride Ceramics. Ceram. Eng. Sci. Proc. 1990: 11(7-8), p. 1028–1045.

[82] DIN EN 1893:2005-07. Hochleistungskeramik - Mechanische Eigenschaften von keramischen Verbundwerkstoffen bei hoher Temperatur in Luft bei Atmosphärendruck - Bestimmung der Eigenschaften unter Zug.

[83] DIN EN 1007-4:2004-08. Hochleistungskeramik - Keramische Verbundwerkstoffe - Verfahren zur Prüfung der Faserverstärkungen - Teil 4: Bestimmung der Zugeigenschaften von Fasern bei Raumtemperatur. DIN EN 1007-6:2008-02 Hochleistungskeramik - Keramische Verbundwerkstoffe - Verfahren zur Prüfung der Faserverstärkungen - Teil 6: Bestimmung der Zugeigenschaften von Fasern bei hoher Temperatur.

[84] Heindl R.A. and Mong L.E. Young's modulus of elasticity, strength and extensibility of refractories in tension. J. Research NBS. 1936: 17, p. 463–482.

[85] Tuckerman L.B. Optical strain gages and extensometers. Proc. Am. Soc. Testing Mats. 1923: 23, p. 602.

[86] Schmitt N., Berthaud Y. and Poirier J. Tensile behaviour of magnesia carbon refractories. J. Eur. Ceram. Soc. 2000: 20(12), p. 2239–2248.

[87] Z.P. Bazant and Pijaudier-Cabot G. Measurement of characteristic length of nonlocal continuum. Journal of Eng. Mechs. 1989: 115(4), p. 755–767.

[88] Mazars J and Bertrand Y. Une technique expérimentale appliquée au béton et pour créer un endommagement diffuse et mettre en évidence son caractère unilatéral. Comptes rendus Acad. Sci. 1989; t.308, série II: p. 579–584.

[89] Nazaret F., Marzagui H. and Cutard T. Influence of the mechanical behaviour specificities of damaged refractory castables on the Young's modulus determination. J. Eur. Ceram. Soc. 2006: 26, p. 1429–1438.

[90] Ghassemi Kakroudi M., Huger M., Chotard T. and Gault C. Tensile behaviour at high temperature of two alumina refractory castables. In Proceedings of UNITECR 2007: p. 528–531.

[91] Huger M., Tessier-Doyen N., Chotard T. et Gault C. Microstructural effects associated to CTE Mismatch for enhancing the thermal shock resistance of refractories: investigation by high temperature ultrasounds. Ceram. Forum. Int. 2007: 84(9), p. E93–E102.

[92] Grasset-Bourdel R., Alzinaa A., Huger M. Chotard T., Emler R., Gruber D. and Harmuth H. Tensile behaviour of magnesia spinel refractories: Comparison of tensile and wedge splitting tests. J. Eur. Ceram. Soc. 2013: 33, p. 913–923.

[93] Kandil F.A. and Dyson B.F. Tensile creep of ceramics: the development of a testing facility. Int. J. High Tech. Ceram. 1988: 4, p. 243–262.

[94] Bisson G. and Regent O. High temperature tensile testing apparatus for industrial ceramics characterization. Key Engineering Materials 1997: 132-136, p. 667–669.

[95] Rendtel A. and Hübner H. Precise tensile creep measurement with refractory ceramics. Cfi/Ber. DKG. 2001: 78(8): p. E45–E47.

[96] Dryden J.R. On the creep in ceramics due to a viscous grain boundary phase. J. Mech. Phys. Solids. 2000: 48, p. 2115–2135.

[97] Hockey B.J. and Wiederhorn S.M. Effect of microstructure on the creep of siliconized silicon carbide. J. Am. Ceram. Soc. 1992: 75, p. 1822–1830.

[98] Chokshy A.H. Diffusion creep in oxide ceramics J. Eur. Ceram. Soc. 2002: 22, p. 2469–2478.

[99] Kottada R.S. and Chokshi A.H. The high temperature tensile and compressive deformation characteristics of magnesia doped alumina. Acta mater. 2000: 48(15), p. 3905–3915.

[100] Wiederhorn S.M., Roberts D.E., Chuang T.J. and Chuck L. Damage-Enhanced Creep in a Siliconized Silicon Carbide: Phenomenology. J. Am. Ceram. Soc. 1998: 71(7), p. 602–608.

[101] Blond E., Schmitt N., Hild F., Blumenfeld P. and Poirier J. Modelling of high temperature asymmetric creep behavior of ceramics. J. Eur. Ceram. Soc. 2005: 25(11), p. 1819–1827.

[102] Chuang T., Wang Z. and Wu D. Analysis of creep in a Si-SiC C-ring by finite element method, J. Eng. Mater. Tech. 1992: 114 (3), p. 311–16.

[103] Lim H.J., Jung J.W., Han D.B. and Kim K.T. A finite element model for asymmetric creep behavior of ceramics. Mater. Sci. and Eng.: A. 1997: 224(1-2), p. 125–130.

[104] Wereszczak A.A., Ferber M.K., Kirkland T.P., Barnes A.S., Frome E.L. and Menon M.N. Asymmetric tensile and compressive creep deformation of hot-isostatically-pressed Y_2O_3-Doped-Si_3N_4. J. Eur. Ceram. Soc. 1998: 19(2), p. 227–237.

[105] Bingham E.C. fluidity and plasticity. Mc Graw-Hill, New York, 1922.

[106] Irgens F. Continuum mechanics, Springer, Bergen, 2008.

[107] Ladevèze P. Sur une théorie de l'endommagement anisotrope. Report LMT-Cachan no. 34, 1983.

[108] Ladevèze P. and Lemaitre J. Damage effective stress in quasi-unilateral condition. 16th IUTAM Congress, Lyngby, Denmark, 1984.

[109] M. Ortiz. A constitutive theory for the inelastic behavior of concrete. Mech. Mater. 1985: 4, p. 67–93

[110] David JR. Tensile Testing. 2nd ed. USA: ASM international technical Book committee. 2004: p. 1–3, 8–12.

[111] Wang Z., Chiang C.K. and chuang T.J. Optimum design of a ceramic tensile creep specimen using a finite element method. J. Research NIST 1997: 102(1), p. 15–28.

[112] Cranner D.C., Richerson D.W. Mechanical testing methodology for ceramic design and reliability. New York, Marcel Dekker Inc. 1998: p. 100–106.

[113] Marquardt D.W. An algorithm for least-squares estimation of non-linear parameters, J. of Soc. for Indust. and Appl. Maths. 1963:11(2), p. 431–441.

[114] https://www.zwick.de/de/aktuelles/testxpo/mitaussteller/messphysik-materials-testing-gmbh.html

[115] Olsen O. and Freeze P.D. Reference Tables for the Platinel II Thermocouple. J. of Research of the National Bureau of Standards. C. Engineering and Instrumentation. 1964: 68C(4), p. 263–281.

[116] ASTM E1012–14. Standard Practice for Verification of Testing Frame and Specimen Alignment Under Tensile and Compressive Axial Force Application, 2014.

[117] Low I.M. Ceramic Matrix Composites – Microstructure, Properties and Applications. Woodhead Publishing, Cambridge, 2006.

[118] Eusner G.R. and Hubble D.H. Technology of spinel-bonded Periclase brick. J. Am. Ceram. Soc. 1960: 43(6), p. 292–296.

[119] Brathe L. and Josefson L. Estimation of Norton-Bailey parameters from creep rupture data. Metal Science.1979: 13(12), p. 660–664.

[120] Roebben G., Bollen B., Brebels A., Van Humbeeck J. and Van der Biest O. Impulse excitation apparatus to measure resonant frequencies: elastic moduli, and internal friction at room and high temperature. Rev. Sci. Instrum. 1997: 68(12), p. 4511–4515.

[121] Munz D. and Fett T. Mechanisches Verhalten keramischer Werkstoffe. Springer Verlag, 1989: p. 176–177.

[122] Lasdon L.S., Waren A.D., Jain A. and Ratner M. Design and Testing of a Generalized Reduced Gradient code for nonlinear programming. ACM Transactions on Mathematical Software (TOMS). 1978: 4(1), p. 34–50.

[123] Marquardt D.W. An algorithm for least-squares estimation of nonlinear parameters. J. Soc. Indust. Appl. Math. 1963: 11(2), p. 431–41.

[124] Lasdon L.S. *et al*. Nonlinear optimization using the Generalized Reduced Gradient method. National Technical Information Service (NTIS). Springfield, 1973.

[125] Levenberg K. A Method for the solution of certain non-linear problems in least squares. Quarterly of Appl. Maths. 1944: 2, p. 164–168.

[126] Wachtman J.B., Cannon W.R. and Matthewson M.J. Mechanical Properties of Ceramics. 2nd ed. John Wiley & Sons, 2009: p. 380–386.

[127] Dahlem E. Characterisation of refractory failure under combined hydrostatic and shear loading at elevated temperatures PhD Thesis. Chair of Ceramics, Montanuniversitaet Leoben, 2011.

[128] Zulhan Z. and Schrade C. Vacuum Treatment of Molten Steel: RH (Rurhstahl Heraeus) versus VTD (Vacuum Tank Degasser). SEAISI Conference and Exhibition, kuala-Lampur, 2014.

[129] Van ende M.A, Kim Y.M, Cho M.K, Choi J., and Junga I.H. Kinetic Model for the Ruhrstahl Heraeus (RH) Degassing Process. The Minerals, Metals & Materials Society and ASM International. 2011: 42B, p. 477–489

[130] Cordonnier T., Hiot B. and Blumenfeld P. How to select magnesia-chromite bricks for RH-degasser applications. The proceeding of 54th international colloquium on refractories, Aachen, Germany. 2011: p.155–158

[131] Gruber D., Auer T., Harmuth H. and Sormann A. FEM based thermo-mechanical investigations of RH-snorkels. Proceedings of Unified International Technical Conference on Refractories, Orlando, 2005.

[132] Jungreithmeier A., Reisinger P., Jandl K., Viertauer A. and Pissenberger E. Vacuum Degassing at voestalphine Stahl. BHM. 2002: 147, p. 138–144.

[133] Lee J., Kim B. and Um C. Development of high-durability hot repair spray and new installation method for the RH snorkel. Proceedings of Unified International Technical Conference on Refractories, Victoria, 2013.

[134] Jin S., Gruber D., Harmuth H., Soudier J., Meunier P. and Lemaistre H. Optimisation of monolithic lining concepts of channel induction furnace. International Journal of Cast Metals Research. 2014: 27(6), p 336–340.

[135] Zabolotsky A.V. Computer simulation of thermal shock in refractory linings of metallurgical installations. Mathematical Models for Eng. Sci. (int. Conf.), Puerto de la Cruz. 2010: p. 73–76.

[136] Andreev K. and Harmuth H. FEM simulation of the thermo-mechanical behaviour and failure of refractories-a case study. J. of Mater. Proc. Tech. 2003: 143-144, p. 72–77.

[137] Jin S. Investigation of compressive refractory creep. PhD Thesis. Chair of Ceramics, Montanuniversitaet Leoben. 2014: p. 39–61.

[138] Hillerborg A. Analysis of one single crack. In: Wittmann F.H., edit. Fracture Mechanics of Concrete. Amsterdam: Elsevier, 1983: p. 223–249.

[139] Drucker D.C., Prager W. Soil mechanics and plastic analysis or limit design. Quart. Appl. Math. 1952:10, p. 157–165.

[140] Chen E. and Buyukozturk O. Methodology for thermomechanical analysis of brittle system. Am. Ceram. Soc. Bulletin. 1985: 64(7), p 982–988.

[141] Chen E. and Buyukozturk O. Methodology for thermomechanical analysis of brittle system. Am. Ceram. Soc. Bulletin. 1985: 64(7), p 988–994.

[142] Nazaret F., Cutard T. and Barrau O. Damage and creep modeling for refractory structures sizing. Conference of Metallurgists (COM). Vancouver, 2010.

[143] Jin S. Investigation of compressive refractory creep. PhD Thesis. Chair of Ceramics, Montanuniversitaet Leoben. 2014: p. 31–38.

[144] Jin S. In-house code: Ascree. Chair of Ceramics, Montanuniversitaet Leoben, 2015.

Appendices

A. mul_process_origin_v3

```
% Mul_process_origin
% Version:                    3.3
% Author:                     Amina SIDI MAMMAR
% Creation Date:              01-Sep-2015
% Last Update Date:           16-Feb-2016

%-------------------------------------------------------------------------%
%-------------------------------------------------------------------------%
%-------------------------------------------------------------------------%
%------PART 1: Parameters Definition and Initialization-------------------%
%-------------------------------------------------------------------------%
%-------------------------------------------------------------------------%
%-------------------------------------------------------------------------%

% Define the optimisation algorithm + related parameters
options =
optimset('LargeScale','off','Display','off','MaxFunEvals',10000,'MaxIter',1000
0,'Tolfun',1e-10,'TolX',1e-8);
options = optimset(options,'Algorithm','levenberg-marquardt');

% Define the folder that contains the measurements
measurement_folder = 'Measurements';

% Define the extension of the measurement files
measurement_extension = 'data';

% Define constant parameters file name
constant_param_file_name = 'constant_parameters.mat';

% Define Norton-Bailay parameters file name for each stage (a, n and k)
nb_fn_stage1 = 'nb_stage1.mat';
nb_fn_stage2 = 'nb_stage2.mat';
nb_fn_stage3 = 'nb_stage3.mat';

% Define the colors of the theoretical and experimental figures for each stage
color_theo_stage1 = 'b';
color_theo_stage2 = 'b';
color_theo_stage3 = 'b';
color_exp_stage1 = 'r';
color_exp_stage2 = 'g';
```

```
color_exp_stage3 = 'k';

%-------------------------------------------------------------------------%
%-------------------------------------------------------------------------%
%-------------------------------------------------------------------------%
%------PART 2: Data Measurements and Related Parameters Extraction--------%
%-------------------------------------------------------------------------%
%-------------------------------------------------------------------------%
%-------------------------------------------------------------------------%

% Get the constant parameters, including the mapping between the
%temperatures and E
const_param = load(constant_param_file_name);

% Get the Norton-Bailey parameters for each stage
nb_stage1 = load(nb_fn_stage1);
nb_stage2 = load(nb_fn_stage2);
nb_stage3 = load(nb_fn_stage3);

% Get the measures and transition times for each file in the measurement
%folder
measures = extract_measurements(measurement_folder, measurement_extension,
const_param);

% Resize all the arrays before mul_norton_bailey (to 75000)
is_resized = true;

%-------------------------------------------------------------------------%
%-------------------------------------------------------------------------%
%-------------------------------------------------------------------------%
%------PART 3: Calculate a, n and k for each stage------------------------%
%-------------------------------------------------------------------------%
%-------------------------------------------------------------------------%
%-------------------------------------------------------------------------%

% Split the measures for each stage
[measures_stage1, measures_stage2, measures_stage3] =split_measures(measures);

% Use the optimization of mul_norton_bailey for each stage, and get the
%corresponding values of a, n and k

[a1, n1, k1] = mul_norton_bailey(measures_stage1, nb_stage1, options,
is_resized);
[a2, n2, k2] = mul_norton_bailey(measures_stage2, nb_stage2, options,
is_resized);
[a3, n3, k3] = mul_norton_bailey(measures_stage3, nb_stage3, options,
is_resized);
```

```
%-------------------------------------------------------------------------%
%-------------------------------------------------------------------------%
%-------------------------------------------------------------------------%
%------PART 4: Get the results and Plot the Experimental------------------%
%--------------------and the Theoretical Functions------------------------%
%-------------------------------------------------------------------------%
%-------------------------------------------------------------------------%
%-------------------------------------------------------------------------%

measures_stage1 = update_theo_strain(measures_stage1, a1, n1, k1);
measures_stage2 = update_theo_strain(measures_stage2, a2, n2, k2);
measures_stage3 = update_theo_strain(measures_stage3, a3, n3, k3);

hold on;
measures_plot(measures_stage1, color_theo_stage1, color_exp_stage1);
measures_plot(measures_stage2, color_theo_stage2, color_exp_stage2);
measures_plot(measures_stage3, color_theo_stage3, color_exp_stage3);
hold off;
```

B. Ultimate strains and correlations

$$\varepsilon_{Ult,1} = A_1(T)\sigma^{B_1(T)}$$

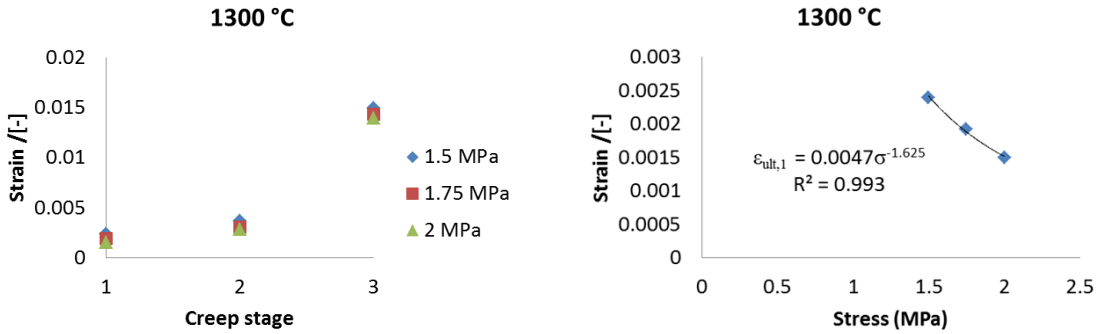

Figure 50: Ultimate primary total strains (a) with respect to creep stage and (b) the applied stress for the magnesia-chromite material at 1300 °C.

$$\varepsilon_{Ult,2} = A_2(T)\sigma^{B_2(T)}$$

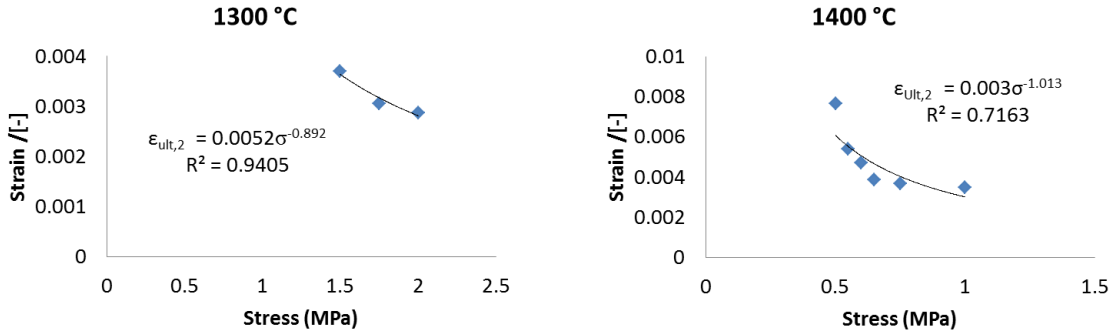

Figure 51: Ultimate secondary total strains with respect to the applied stress for the magnesia-chromite material at (a) 1300 °C and (b) 1400 °C.

$$\varepsilon_{Ult,2} = A_2(T)\sigma^{B_2(T)}$$

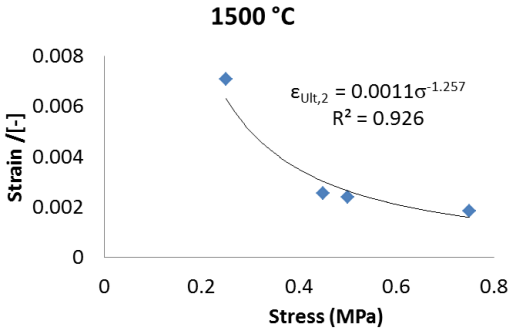

Figure 52: Ultimate secondary total strains with respect to the applied stress for the magnesia-chromite material at 1500 °C.

$$\varepsilon_{Ult,3} = A_3(T)\sigma^{B_3(T)}$$

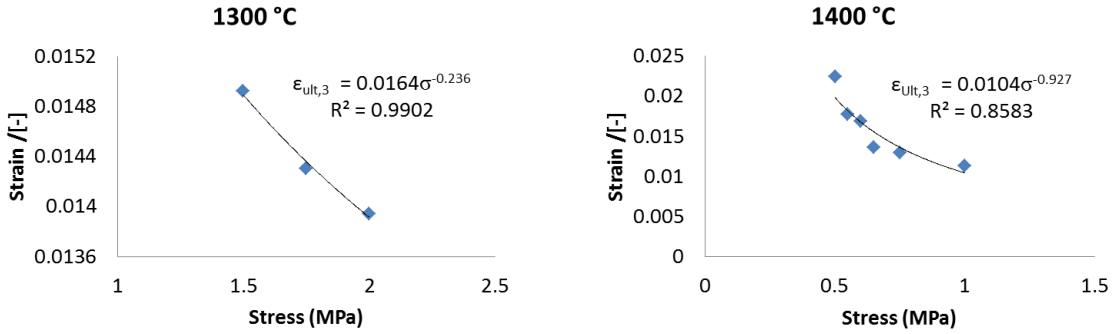

Figure 53: Ultimate tertiary total strains with respect to the applied stress for the magnesia-chromite material at (a) 1300 °C and (b) 1400 °C.

$$\varepsilon_{Ult,3} = A_3(T)\sigma^{B_3(T)}$$

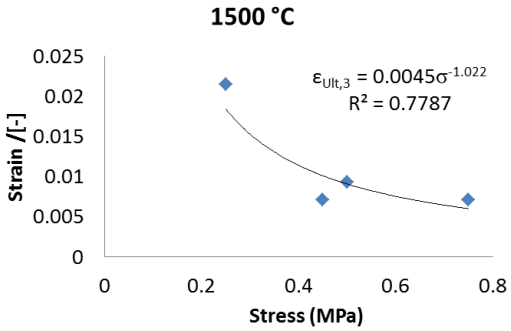

Figure 54: Ultimate tertiary total strains with respect to the applied stress for the magnesia-chromite material at 1500 °C.